DESIGN OF HYBRID 2D AND 3D NANOSTRUCTURED ARRAYS FOR ELECTRONIC AND SENSING APPLICATIONS

A Dissertation
Presented to
The Academic Faculty

by

Hyunhyub Ko

In Partial Fulfillment
of the Requirements for the Degree
Doctor of Philosophy in the
School of Materials Science and Engineering

Georgia Institute of Technology
April 2008

DESIGN OF HYBRID 2D AND 3D NANOSTRUCTURED ARRAYS FOR ELECTRONIC AND SENSING APPLICATIONS

Approved by:

Dr. Vladimir V. Tsukruk, Advisor
School of Materials Science and Engineering
Georgia Institute of Technology

Dr. Satish Kumar
School of Polymer, Textile and Fiber Engineering
Georgia Institute of Technology

Dr. Christopher Summers
School of Materials Science and Engineering
Georgia Institute of Technology

Dr. Meisha Shofner
School of Polymer, Textile and Fiber Engineering
Georgia Institute of Technology

Dr. Valeria Milam
School of Materials Science and Engineering
Georgia Institute of Technology

Date Approved: March 7, 2008

To my loving family

Acknowledgements

This work would not have been possible without the help and support of great number of people. I would first like to thank my advisor, Dr. Vladimir V. Tsukruk, for his continuous encouraging and guiding me to this point. I learned the way to organize and present results from him. I also thank my committee members, Dr. Christopher J. Summers, Dr. Satish Kumar, Dr. Valeria Milam, Dr. Meisha Shofner for their advice and comments on my work.

There have been a number of people whose assistance has been a great help to my research. Especially, I would like to thank our current and old SEMA members, Ray, Sehoon, Srikanth, Michael, Eugenia, Dima, Sergiy, Marina, Melbs, Yen-Hsi, Yuri, and Chaoyang for their technical supports and valuable discussions. I am grateful for the financial support from the NASA through NDE Center Contract NAG 102098, AFOSR Grant No. F496200210205, and the support from Agiltron and Army Research Office (ARO).

My special thanks go to my family. Especially, I am really indebted to my parents for their endless love and support. Most importantly, I cannot thank my wife Yumean enough for her support and encouragement. Thank you for your patience and trust. Finally, my son and daughter, Hogan and Hannah, I feel sorry not to spend enough time with you. I promise to be a good friend with you.

Table of Contents

List of Tables

List of Figures

Summary

This dissertation presents the design of organic/inorganic hybrid 2D and 3D nanostructured arrays via controlled assembly of nanoscale building blocks. Two representative nanoscale building blocks such as carbon nanotubes (one-dimension) and metal nanoparticles (zero-dimension) are the core materials for the study of solution-based assembly of nanostructured arrays. The electrical, mechanical, and optical properties of the assembled nanostructure arrays have been investigated for future device applications. We successfully demonstrated the prospective use of assembled nanostructure arrays for electronic and sensing applications by designing flexible carbon nanotube nanomembranes as mechanical sensors, highly-oriented carbon nanotubes arrays for thin-film transistors, and gold nanoparticle arrays for SERS chemical sensors.

In first section, we fabricated highly ordered carbon nanotube (CNT) arrays by tilted drop-casting or dip-coating of CNT solution on silicon substrates functionalized with micropatterned self-assembled monolayers. We further exploited the electronic performance of thin-film transistors based on highly-oriented, densely packed CNT micropatterns and showed that the carrier mobility is largely improved compared to randomly oriented CNTs. The prospective use of Raman-active CNTs for potential mechanical sensors has been investigated by studying the mechano-optical properties of flexible carbon nanotube nanomembranes, which contain freely-suspended carbon nanotube array encapsulated into ultrathin (<50 nm) layer-by-layer (LbL) polymer multilayers.

In second section, we fabricated 3D nano-canal arrays of porous alumina membranes decorated with gold nanoparticles for prospective SERS sensors. We showed extraordinary SERS enhancement and suggested that the high performance is associated with the combined effects of Raman-active hot spots of nanoparticle aggregates and the optical waveguide properties of nano-canals. We demonstrated the ability of this SERS substrate for trace level sensing of nitroaromatic explosives by detecting down to 100 zeptogram (~330 molecules) of DNT.

Chapter 1. Introduction

1.1. Motivation

Nanostructured materials represented by zero-dimensional structures such as quantum dots and metal nanoparticles and one-dimensional nanorods, nanotubes and nanowires have been studied intensely due to their unique mechanical, electrical, and optical properties arising from their nanometer size (1~100 nm at least one-dimension). Significant advancements have been made in developing synthetic techniques of nanomaterials with good control over the shape, and interesting properties of these nanomaterials have been discovered. The next challenge is the fundamental understanding of the collective properties of nanoscale building blocks when they are assembled into nanostructure arrays and the utilization of these nanostructures for a wide range of future device applications (Figure 1.1). For the realization of these device applications, the development of efficient assembly strategies of nanoscale building blocks into hierarchical nanostructure arrays is needed, which could be achieved by controlling the shape, location, and orientation of large amounts of nanoscale building blocks.

While solution-based assembly approaches, so-called bottom-up assembly, provide simple, low-cost and large-area fabrication of nanostructure arrays, the top-down patterning via lithographic method offers arbitrary, complex device geometry and registration. A rational strategy of assembling of nanoscale building blocks into higher-order functional devices will be the assembly of building blocks on top of pre-defined chemical or physical templates fabricated by top-down methods. In this templated

assembly approaches, the chemical or physical patterns have been used to guide the organization of nanoscale building blocks into complex device structures.

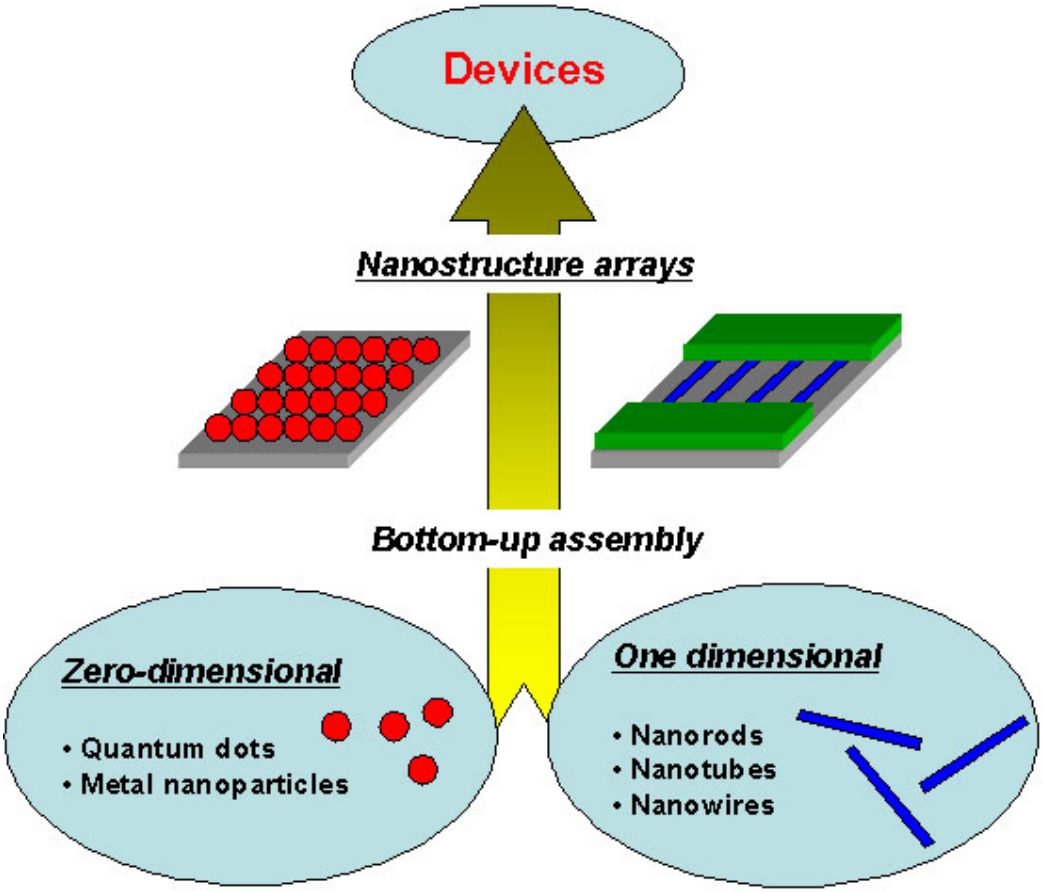

Figure 1.1. Bottom-up assembly of nanoscale building blocks into nanostructure arrays for device applications

The goal of this work is the design of hybrid 2D and 3D nanostructured arrays for proof-of-concept device applications via controlled bottom-up assembly of nanoscale building blocks onto various substrates. This work explores several solution-based strategies to organize nanoscale building blocks into 2D and 3D nanostructured arrays onto various substrates containing chemical or physical templates. Two representative nanoscale building blocks, that is, carbon nanotubes (one-dimension) and gold

nanoparticles (zero-dimension) will be used for the solution-based assembly of nanostructured arrays. The evaluation of unique physical properties of the assembled nanostructures for future device applications is essential focus of this study. For the sake of proof-of-concept device applications, nanostructure arrays will include 1) highly-oriented carbon nanotubes arrays for thin-film transistors, 2) flexible carbon nanotube nanomembranes for mechanical sensors, and 3) gold nanoparticle arrays for surface-enhanced Raman scattering (SERS)-based chemical sensors.

This thesis is organized in the following format. A brief literature background of carbon nanotubes and gold nanoparticles is introduced in Chapter 1. Chapter 2 describes the materials and characterization methods used in this thesis. In Chapter 3, we introduce several solution-based methods to organize carbon nanotubes into well-ordered and patterned arrays on the silicon substrates by using chemical templates prepared by microcontact printing. We also investigate the assembled CNT arrays by using Raman spectroscopy and prove the change in Raman shift depending on the nanostructure of CNT arrays. As an extension of well-ordered CNT arrays, in Chapter 4, we report the formation of long-range ordered and densely-packed array of CNTs via liquid crystalline processing by simple tilted-drop casting of CNT solution on functionalized micropatterned geometries and further demonstrate that the electrical performance of thin-film transistors based on these densely-packed uniformly oriented CNT array is dramatically improved compared to random CNTs.

To study the CNT arrays inside the polymer membranes, in Chapter 5, we describe the fabrication of freely suspended polymer nanomembranes with embedded carbon nanotubes and the investigation of the deformational behavior of ultrathin (<100 nm) nanomembranes subjected to elastic deflections by conducting *in-situ* monitoring of resonance Raman scattering directly in the course of full deformational cycle. In Chapter 6, we demonstrate that the patterned array of carbon nanotubes can be successfully incorporated into the freely suspended LbL membranes by using the micropatterned LbL surface as a template for subsequent nanotube assembly. The capability of polymer sacrificial templates for the encapsulation of organized arrays inside the LbL membranes have been extended in Chapter 7, in which we introduce a novel patterning technique, termed capillary transfer lithography, for the creation of well-defined 3D polymer microstructures onto polyelectrolyte LbL multilayers and demonstrate successful encapsulation of organized arrays from both carbon nanotubes and gold nanoparticles within polyelectrolyte multilayers.

In Chapter 8, we describe the design of metal nanostructured arrays for SERS substrates. We introduce a design of nanocanal arrays of porous aluminum membranes decorated with gold nanoparticles immobilized into polyelectrolyte surface layers inside these nanocanals and demonstrate efficient SERS substrates showing giant enhancements factor compared to convential 2D SERS substrates. We further extend this approach in Chapter 9 for the deposition of hot spots of nanoparticle aggregates for highly-efficient SERS substrates capable of detecting trace level explosives.

1.2. Carbon nanotube Basics

1.2.1. Structure and Fundamentals

CNTs consist of one or several curled graphene sheet (hexagonal lattice of carbon) with hemisphere caps that can be SWNTs (Figure 1.2b-e) or MWNTs (Figure 1.2f), respectively.[1] A SWNT can be considered as graphene sheet rolled up into hollow cylinder (Figure 1.2a). The ends of the CNTs consist of fullerene-like caps or

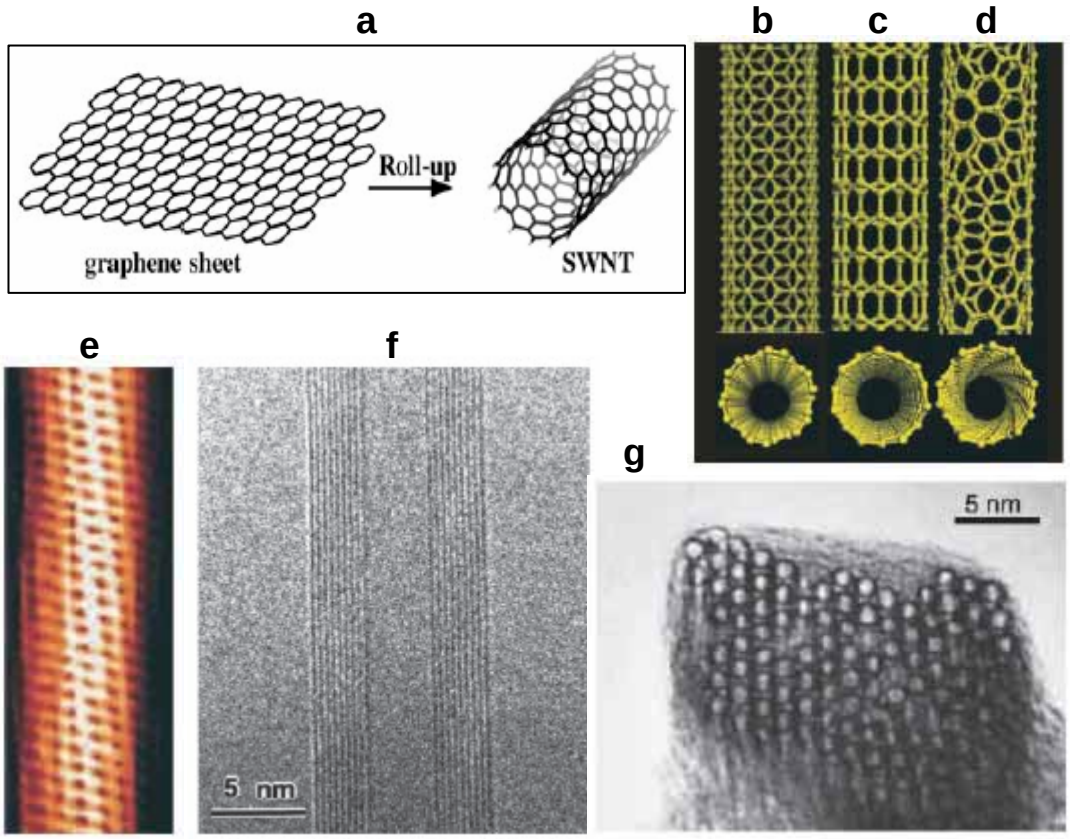

Figure 1.2. (a) Schematic of SWNT that can be formed by rolling up the grapheme sheet into hollow cylinder. Schematic of (b) armchair, (c) zigzag, and (d) chiral SWNTs. (e) Scanning tunneling microscope image of chiral SWNT. (f) Transmission electron microscope (TEM) image of a MWNT. (g) TEM image showing lateral packing of SWNTs in a bundle. (From ref. 4)

hemispheres. As shown in Figure 1.3, their individual structures of nanotube can be characterized by chiral vector $C_h = na_1 + ma_2 = (n, m)$ which determine their diameter and chirality, where n and m are integers and a_1 and a_2 are unit vectors of the hexagonal lattice.[2] The diameter of carbon nanotube d_t can be determined by using the relationship $d_t = \sqrt{3}a_{c-c}(n^2 + nm + m^2)^{1/2}/\pi = C_h/\pi$, where C_h is the length of chiral vector C_h and a_{c-c} is the C–C bond length (1.42 Å).

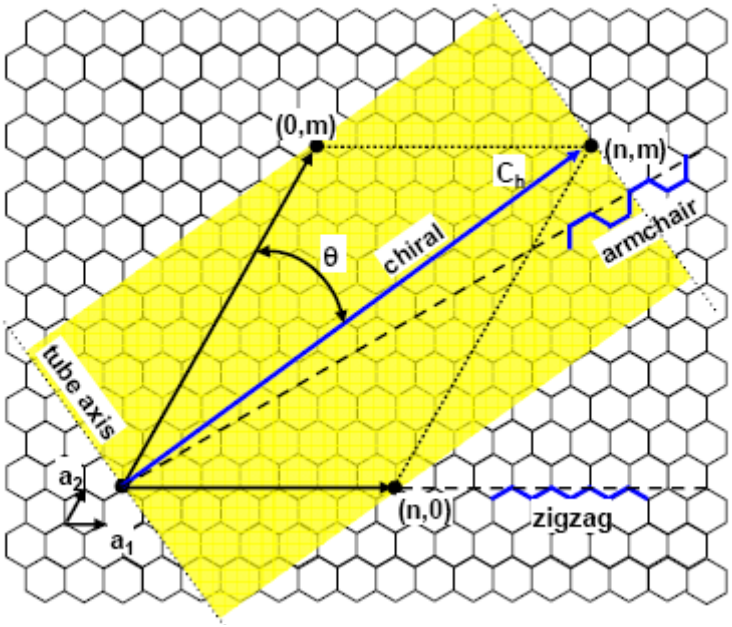

Figure 1.3. Schematic diagrams of chiral vector on graphene sheet (hexagonal lattice of carbon). The chiral vector $C_h = na_1 + ma_2$ is defined by two integers (n, m) that relate C_h to the two unit vectors a_1 and a_2. The direction of nanotube axis is perpendicular to the chiral vector. The achiral cases, zigzag (n or m = 0) and armchair ($n = m$) are indicated with dashed lines.

When we roll up the shaded area of graphene sheet along the chiral vector C_h in Figure 1.3, we get a SWNT specified by the integers (n, m). Different pairs of integers (n, m) define three different types of SWNTs; armchair ($n = m$, Figure 1.2b), zigzag ($n = 0$ or $m = 0$, Figure 1.2c), and chiral ($n \neq m$, Figure 1.21d) nanotubes. The chiral angle θ is

defined by the angle between the chiral vector C_h and the "zigzag" direction. The zigzag and armchair nanotubes, respectively, correspond to chiral angles of $\theta = 0$ and 30°, and chiral nanotubes correspond to $0 < \theta < 30°$. Differences in the nanotube diameter and chiral angle (chirality) give rise to differences in the properties of the various carbon nanotubes.

The as-prepared SWNTs are in the form of many micrometers long bundles or ropes consisting of individual nanotubes in a close-packed triangular lattice (Figure 1.2g). The diameter of individual nanotubes is in the range of 1–2 nm and the number within a rope varies from tens to several hundreds. As a result of substantial van der Waals attractions between tubes,[3] long SWNTs aggregate easily and are difficult to be suspended in solvents. Therefore, two of vital steps in the realization of promising applications of carbon nanotubes are to gain reliable control over their surface chemistry and to achieve monodispersity in nanotube length, diameter, and chirality.

1.2.2. Selected Properties

Carbon nanotubes have a broad range of electronic, thermal, and structural properties that change depending on different kinds of nanotubes (defined by its diameter, length, and chirality). One of the most intriguing properties of carbon nanotubes is that the electronic structure of carbon nanotube can be either metallic or semiconducting depending on its chirality and diameter. Also, carbon nanotubes have attracted the attention worldwide because of their excellent mechanical properties. Several important properties of carbon nanotubes are stated below.

1.2.2.1. Electrical Properties

Carbon nanotubes, specified by chiral vector $C_h = na_1 + ma_2 = (n, m)$, can be metallic or semiconducting depending on their chirality. All armchair ($n = m$) tubes are metals; tubes with $n - m = 3k$, where k is a nonzero integer, are semiconductors with very tiny band gap, but practically considered as metals; and all others ($n - m \neq 3k$) are semiconductors with large band gap. Therefore, when tubes are formed with random values integers (n, m), we would expect that two-thirds of nanotubes would be semi-conducting, while the other third would be metallic. However, these metallic and semiconducting nanotubes are typically grown together as bundles. For the utilization of carbon nanotubes in various applications, it is necessary to separate these two kinds of carbon nanotubes. Recently, several promising attempts have been reported to separate metallic and semiconducting carbon nanotubes by using electric fields or chemical functinalization.[4,5]

The unique electrical properties of carbon nanotubes arise from the nearly one-dimensional electronic structure caused by the confinement of electrons around the circumference of the nanotubes. Metallic nanotubes conduct electrons ballistically (without scattering) over long nanotube lengths, enabling them to carry high current densities with essentially no heating.[6] MWNTs show similar electronic properties to those of metallic SWNTs if the outer graphene layer is metallic.[7] As mentioned above, one-third of the graphene layers of MWNT would be conducting.

1.2.2.2. Mechanical Properties

The extremely high Young's modulus, stiffness and resilience of carbon nanotubes have led to their use in the development of high strength, lightweight material applications. Carbon nanotubes can be expected to have extremely high modulus similar to that of in-plane graphite, which is the largest of any known bulk material.[8] Young's modulus of SWNTs bundle is ~1 TPa; the tensile strength is ~30 GPa.; the strain values at breaking is up to 5 %.[9] In view of their applications in lightweight structural materials, it is impressive that the density-normalized strength and modulus of SWNTs are, respectively, ~56 and ~19 times that of steel wire. While the Young's modulus of MWNT was reported as 1.3 TPa,[10] the actual strength in practical situations would be further affected by the sliding of individual graphene cylinders with respect to each other.

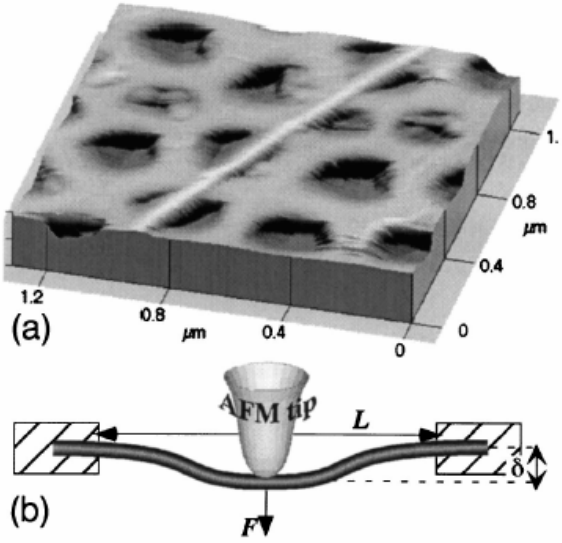

Figure 1.4. (a) AFM 3-D image of a SWNT bundle that adheres to a membrane, with a portion free-standing over a hole. (b) Schematic representation of the measurement technique. The AFM tip is used to apply a load F and the displacement δ is measured. (From ref. 11)

However, the precise determination of their mechanical properties remains a challenge due to the technical difficulties involved in the manipulation of testing tools with nano-scale. As can be seen in Figure 1.4, one way of testing the Young's modulus of nanotubes is to use the AFM tip to bend carbon nanotubes (anchored on substrate or free-standing across a hole) while simultaneously recording the force exerted by the tube as a function of the displacement from its equilibrium position.[11]

A variety of experimental evidence confirms that carbon nanotubes can sustain significant elastic deformations.[12,13] Carbon nanotubes can be bent into small circles or into sharp loops without breaking. Carbon nanotubes have the ability to significantly change their shape, accommodating to external forces without irreversible atomic rearrangements. They develop buckles in compression and bending, and still can reversibly restore their original shape. Under severe bending, buckling is the usual way for the nanotubes to reduce strain. This kind of elastic buckling makes the carbon nanotubes exceedingly tough materials.

1.2.2.3. Optical Properties

The carbon nanotubes show strong dependence of optical absorption on the nanotube geometry (diameter and chirality) and polarization direction.[14] Recently, it was reported that individual semiconducting SWNTs show band gap fluorescence, which could prove useful in biomedical and nanoelectronics applications.[15] However, bundles of nanotubes broadened the adsorption spectra due to the interaction with metallic nanotubes. Carbon nanotubes were experimentally proved to be a third order nonlinear

optical (NLO) material with enough third order NLO susceptiblities for photonic applications.[16]

The strong coupling between electrons and phonons in 1-D carbon nanotube system gives rise to highly unusual resonance Raman spectra. Therefore, the main experimental technique for studying phonons in carbon nanotubes has been Raman spectroscopy.[17,18] Carbon nanotubes show many unique and unusual features of Raman spectra such as radial breathing mode, tangential stretch mode, and disorder-induced D-band. These main features of Raman spectra has been successfully used to determine the chiral vector (n,m) and, therefore, diameter distributions and metallic/semiconducting characters of carbon nanotubes.

Raman spectroscopy has played an important role in the characterization of carbon nanotubes, both in terms of the diameter distribution in SWNT bundles and whether a SWNT is metallic or semiconducting. When the incident or scattered photons in the Raman process are in resonance with an electronic transition between the valence and conduction bands at special energy states, E_{ij}, the Raman signal becomes very large as a result of the strong coupling between the electrons and photons of the nanotube under these resonance conditions. Therefore, the resonance process is highly selective of particular SWNTs, since each SWNT, characterized by two integers (n, m), has a unique set of such electronic transitions energies, E_{ij}.

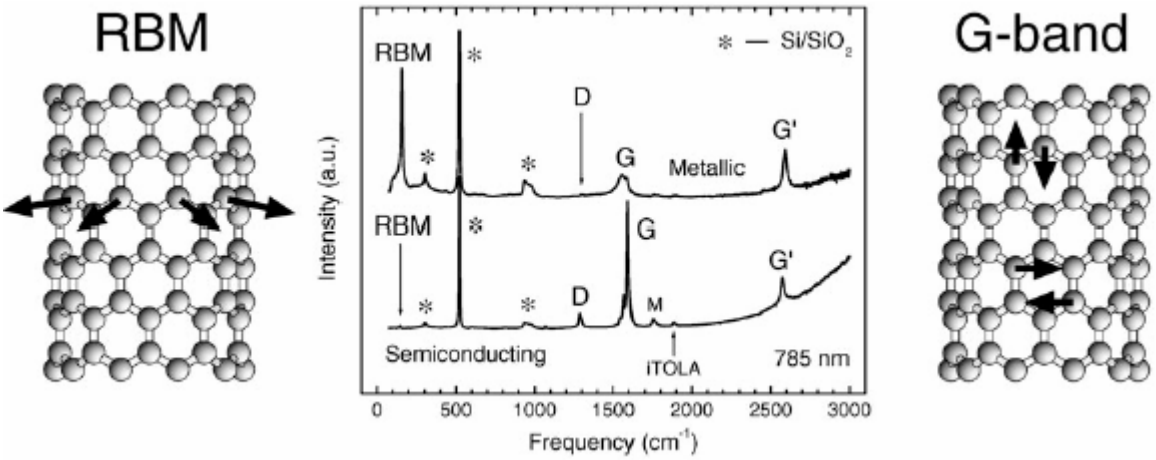

Figure 1.5. Raman spectra from a metallic and semiconducting SWNT using 785 nm laser excitation, showing the RBM, D band, G band, and G′ band features. Left and right images show atomic displacements associated with the RBM and G band vibrations. The spectra marked with an asterisk (*) are from the silicon substrate. (From ref. 103)

As was shown in Figure 1.5, the four most important features in Raman spectra of carbon nanotubes are the radial breathing mode (RBM) in the 150–200 cm^{-1} range, the disorder-induced D band in the 1250–1450 cm^{-1} range, the tangential G band in the 1500–1600 cm^{-1} range, and the G′ band in the 2500–2900 cm^{-1} range.[19] The frequency of RBM is strongly related to the nanotube diameter, in which all the carbon atoms vibrating in the radial direction. The G band feature is used to elucidate the differences between the metallic and semiconducting nanotubes where neighboring carbon atoms are vibrating in the opposite directions along the nanotube surface as in 2-D graphite. The D band is typically attributed to the presence of amorphous carbon in bulk nanotube samples or an inherent feature of SWNTs and may be related to symmetry lowering effects such as defects, bending of the nanotubes, and finite-size effects. The ratio of relative intensities of *D* band to *G* band is the measure of the degree of structural order. The G′ band is the second-order harmonic spectra of D band and exhibits a large

dispersion either when the laser energy is changed or when compressive and tensile strains are applied.

1.2.3. Purification and Solubilization

1.2.3.1. Purification

The as-prepared carbon nanotubes contain large amounts of impurities (typically 30 % or more), such as metal catalyst particles, amorphous carbon, and fullerenes, which need to be removed for the purpose of many potential applications of carbon nanotubes. These impurities are closely entangled with long ropes of carbon nanotubes, via physically or occasionally even via chemical bonds. The metal catalyst impurities are usually covered by amorphous carbon and attached to the ends of nanotube ropes.

A number of purification methods have been reported to date such as oxidation in gas or acid, filtration, chromatography, centrifugation and mixture of these methods. A major advantage of filtration and centrifugation methods is that the structures of carbon nanotubes are undamaged.[20,21,22] Also, the chromatography method produces highly pure and undamaged carbon nanotubes.[23] However, since the carbon nanotubes are insoluble in any solvent, it is difficult to directly apply the physical purification methods such as filtration and centrifugation. It is possible to disperse carbon nanotubes in aqueous surfactant solution with the aid of sonication. During the sonication, carbon nanotubes are encapsulated by the surfactant micelles and can be suspended in water. Subsequent centrifugation removes a large fraction of high-density undispersed amorphous carbon

and metal particles. After that, it needs several successive filtrations to remove small-size impurities.

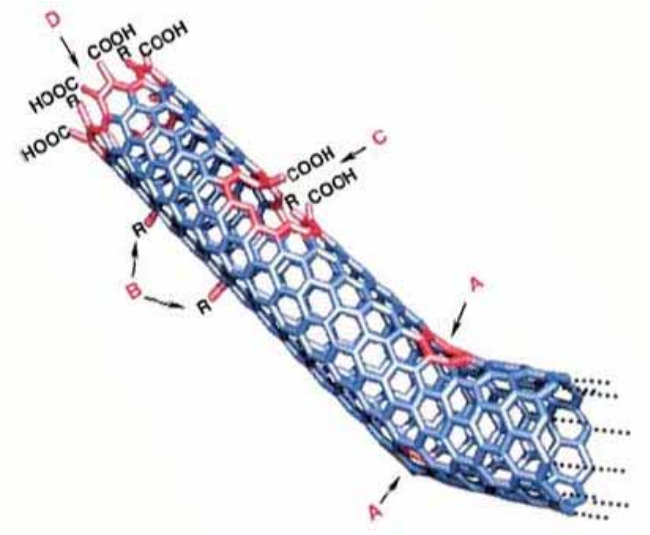

Figure 1.6. Typical defects in a SWNT: a) pentagon or heptagon defects in the sidewall leads to a bend in the nanotube, b) sp^3-hybridized defects (R = H or OH), c) the sidewall damaged by oxidative conditions, which is terminated with carboxylic groups (-COOH), d) open end of SWNT terminated with –COOH groups by oxidative conditions. Besides carboxylic groups, other terminal groups such as carbonyl (–C=O) and hydroxyl (–OH) groups are possible. (From ref. 69)

Many researchers use the oxidative treatments of carbon nanotubes in acids to oxidize and decompose impurities such as amorphous carbon and metal particles.[24,25,26,27] For example, refluxing the nanotubes in dilute nitric acid (3M) was found efficient for removing amorphous carbon and metal catalysts. Oxidation methods of purification use the unexpected resistance of nanotube structures towards oxidation. During the oxidative treatments, the impurities are more prone to oxidative attack compared with the surfaces of nanotubes. Also, with the oxidation of impurties, the oxidation of nanotubes preferentially takes place at the the ends of naotubes, where the pentagon defects are located, and some defects on the sidewall. Figure 1.6 shows the typical defects in a

SWNT which are intrinsic or induced by oxidation.[28] However, there is a large loss of carbon nanotube material during oxidation, which means that some nanotubes are destroyed. Durjardin et al. have proposed that the outer SWNTs of a bundle are decomposed into amorphous carbon, which protects the inner SWNTs from further oxidation.

1.2.3.2. Solubilization

The chemical modification and solubilization of carbon nanotubes represent a vital research field in the development of carbon nanotube-based materials and systems. The soluble carbon nanotubes offer excellent opportunities not only in the study of fundamental properties of carbon nanotubes but also in the utilization of carbon nanotubes in various applications. However, SWNTs typically exist as ropes or bundles with several micrometers long and 10–25 nm in diameter; the strong van der Waals interactions and poor wettability of SWNTs make it hard to break the SWNT bundles;[29] the SWNT bundles are entangled together in the form of a highly dense, complex network structure. These factors, coupled with the fact that graphitic cylinders do not have any surface functional groups, make them very difficult to disperse in organic solvents.

As previously mentioned, the chemical oxidation of carbon nanotubes has been used as a purification method to decompose impurities. In addition, the oxidation of carbon nanotubes with concentrated HNO_3 and H_2SO_4 mixed with HNO_3 or H_2O_2 have been widely used to generate oxygen-containing functional groups on the ends and walls

of carbon nanotubes, thus improving their solubility.[24,25] As a result of the chemical oxidation, the ends and sidewalls of the carbon nanotubes are covered with oxygenated groups such as carboxylic (–COOH), carbonyl (–C=O), and hydroxyl (–OH) groups.[30,31] During the oxidation process, the oxidizing agents can wet and intercalate into the SWNT bundles, which make the SWNT bundles to break and more soluble in organic solvents. This way, relatively stable aqueous suspension of nanotubes can be prepared with or without[32] the help of surfactants.

However, the chemical oxidation treatments introduce defects on the nanotube surfaces that may affect the various intrinsic properties of carbon nanotubes. For example, the intercalation of the nanotube lattice by oxidizing agents such as nitric acid molecules can lead to changes in the Raman spectra of SWNTs by doping.[33] The doping of SWNTs by nitric acid also causes the changes in interband electronic transitions in the far- and near-IR spectra.[34] Furthermore, the defects could cause a significant destruction of carbon nantoubes in the process of oxidation and produce carbonaceous impurities.[35] On the other hand, the introduced defect sites on the nanotube sidewall can be used to shorten the micrometers long carbon nanotubes.

The acid-oxidized SWNTs can be dispersed only in several amide-type organic solvents and water with the help of sonication. Tuning the solubilization of carbon nanotubes in various organic solvents will require the attachment of relatively large functional groups to the nanotubes. A variety of oligomeric and polymeric compounds have been used in the functionalization of carbon nanotubes for their solubility in

different organic solvents and water. Because of its simplicity and efficiency, surfactants such as sodium dodecylsulfate (SDS) or benzylalkonium chloride are frequently used for the dispersion of carbon nanotubes.

1.2.4. Assembly of Carbon Nanotubes

Since the discovery of multi-walled carbon nanotubes (MWNTs) in 1991 and single-walled carbon nanotubes (SWNTs) in 1993,[36,37,38] carbon nanotubes (CNTs) have been studied intensely due to their unique structural, mechanical, electrical, and optical properties. Besides their extremely small nanometer size with quasi one-dimensional geometrical dimensions, CNTs exhibit remarkable electrical conductivity, chemical and thermal stability, unusual high tensile strength and elasticity.[39] Numerous potential applications of CNT-based devices have been proposed including field-effect transistor,[40] field emitter,[41] probe tips,[42,43] chemical sensors,[44,45] and electromechanical sensor.[46] However, in order to utilize CNTs in nanodevices, it is necessary to develop efficient strategies for their assembling into hierarchical nanostructures, which could be achieved by controlling the shape, location, and orientation of a large amount of nanotube arrays.

Self-organization of CNTs into highly ordered arrays has been approached by direct-growth assembly or post-growth assembly methods. Significant progress in growing vertically aligned nanotube assemblies on patterned substrates has been made recently with pre-catalyst patterning and chemical vapor deposition (CVD).[47,48,49] Direct-growth assembly by CVD has the advantage of achieving highly ordered and densely packed nanostructures. However, the requirements of high temperature (typically >800

°C) and reactive environment have prevented its application from devices with limited thermal and/or chemical stability such as polymer-involved systems. Post-growth assembly of CNTs in a vertical direction has been demonstrated by the deposition of CNTs from suspension onto chemically modified surfaces.[50] On the other hand, several in-plane orientation methods have been reported, such as catalytic growth,[51,52] alignment in electric and magnetic fields,[53,54,55] and self-assembling on chemically modified surfaces.[56,57,58,59,60] Among all these approaches, bottom-up assembly based on solution processes has recently received great attention because of the associated mild conditions and the ability to produce well-defined nanostructures.

The applications of CNTs into various nanoelectronic devices require not only uniform orientation of CNTs but also organization of the CNT assembly into complex structures or device architectures. Therefore, CNT assembly on patterned substrate will be a critical step into the realization of CNT-based nanodevices. Microcontact printing is an efficient method for patterning self-assembled monolayers with different chemical functionalities on a variety of substrates. With the precise control over the chemical functionalities, patterned substrates can be used for selective attachment of CNT assembly. Also, micropatterning has been successfully used as microfluidic channels to guide the assembly of nanowires into parallel arrays or cross-bar junctions.[61] However, CNT assembly on patterned substrate is still in an early stage of development.

Soft lithography, which uses PDMS elastomer as a stamp or a mold, has been an efficient technique to prepare chemical or physical micropatterned templates on various

solid surfaces including silicon, glass, and metal substrates. For example, microcontact printing was used for the patterning of self-assembled monolayers (SAMs) of thiols on metal surfaces and siloxanes on hydroxyl-terminated substrates. For physical templates, nanoscale patterns of 2D polymer has been prepared by microcontact printing and used as a scaffold for the deposition of gold nanoparticles.[62] Moreover, well-defined 3D polymer microstructures have been fabricated by using various molding methods including imprint lithography,[63,64] microtransfer molding,[65] micromolding in capillaries,[66,67] solvent-assisted micromolding,[68] and capillary force lithography.[69] In these processes, an elastomeric master is usually pressed into a compliant polymer film which has been softened by heat or solvent, enabling the polymer to fill the recessed areas of the master by capillary forces. In most cases, additional dry etching process is needed to remove a residual film of the polymer remainings in the compressed areas.

There are a number of issues that remain to be addressed before these techniques can be used in the organization of CNT assembly. First of all, the precise chemical functionalities of patterned substrates by microcontact printing still need to be better controlled and systematically studied. Second, the exact control over the integration density of CNT assembly and the development of appropriate organization techniques need to be accomplished. For example, highly packed CNT assembly which will be needed in dense array of sensor is difficult to achieve for typical dip-coating techniques. Third, the control over the microfluidic behavior on the patterned substrate needs to be achieved. Even though the behavior of CNT solution on patterned substrate will have

enormous effects on the alignments of CNT assembly, there is little knowledge about the microfluidic behavior on patterned substrates.

1.2.5. The Prospective Applications of CNTs

Since the electronic properties of carbon nanotubes are strong function of mechanical deformation or chemical doping, such changes can be easily detected by electron current signals and these properties make CNTs strong candidates for sensor arrays sensitive to their chemical and mechanical environments. Recent experimental and theoretical works have proved that the semiconducting SWNTs show a significant conductance change in response to physisorption of certain gas molecules,[70,71,72,73] demonstrating their ability to act as extremely sensitive chemical sensors. Dai and coworkers were the first to use nanotube field-effect transistor as sensitive chemical sensors at ambient temperature. They found the conductivity of the SWNT changed rapidly upon exposure to nitrogen dioxide (NO_2) and ammonia (NH_3). The principles for carbon nanotube chemical sensors to detect gases or molecules are based on the changes in electronic properties induced by charge transfer with the molecules due to physical adsorptions. The electron-donor or electron-acceptor gas molecules adsorbed on the surface of nanotubes can either donate or remove electrons from carbon nanotubes, resulting in changes of their electrical conductivity. Exposure of the p-type transistor to electron-donating NH_3 results in hole depletion in the nanotube and consequently reduced electrical conductivity. However, exposure to electron-withdrawing NO_2 causes accumulation of hole carriers in the nanotube and enhanced electrical conductivity.

Carbon nanotube gas sensors offer several potential advantages over traditional sensor materials with respect to sensitivity, operation at room temperature, and small sizes for device miniaturization and massive sensor arrays. For conventional sensors, semiconducting metal oxides have been used for NO_2 and NH_3 detection, but they operate at high temperatures (200° to 600°) to attain high sensitivity[74] and organic materials-based sensors have undesirably high electrical resistivity.[75] Also, the adsorption of gas molecules arises only on the limited surface region of the macroscopic sensors, making them undesirable for highly sensitive gas sensors. However, for carbon nanotube sensors, the adsorption of gas molecules to the surface of a nanotube can lead to depletion or accumulation of carriers in the "bulk" of the one-dimensional nanostructure and increase sensitivity to the point of molecular-scale detection even at room temperature. In addition, the extremely high surface-to-volume ratio of a nanotube is ideal for efficient gas molecules adsorption. Also, the small size of nanotube building blocks and recent advances in assembly suggest that dense arrays of sensors could be prepared.

Recently, it was reported that the mechanical deformation of CNTs strongly affects their electronic properties.[76,77] It has been demonstrated that the mechanical strain can open a band gap in a metallic CNT and modify the band gap in a semiconducting CNT. Theoretically, the full range of electronic bandgap changes of carbon nanotubes have been computed as functions of axial compression, tensile stretch, torsion, and bending strain.[78] These examples of strong dependence of CNT band structure on the mechanical deformation demonstrate a possibility of developing carbon nanotubes as mechanical sensors. For example, a 30 μm thick film of randomly oriented carbon

nanotubes have been demonstrated as macroscale strain sensors, in which the measured voltage changes are proportional to the applied strain.[79] Changes of optical properties along with mechanical deformation of carbon nanotubes also make them useful as strain sensors. For example, Raman spectra are known to give shifted peaks when CNTs undergo stress or strain.[80,81] This phenomenon has been used to detect phase transitions and to measure stress fields in polymers with embedded nanotubes.[82,83,84]

1.2.5.1. Flexible carbon nanotube nanomembranes

The development of assembly processes for hierarchical organization of carbon nanotubes encapsulated into flexible polymer nanomembranes are very important prerequisites for their potential applications in a variety of sensor devices. One of potential sensing applications of carbon nanotubes is the strain sensor arrays, in which the mechanical deformation of carbon nanotubes affects their electrical or optical properties. Recently, it was reported that the mechanical deformation of CNTs strongly affects their electronic properties.[85,86] A thin film of randomly oriented carbon nanotubes have been demonstrated as macroscale strain sensors, in which the measured voltage changes are proportional to the applied strain.[87] On the other hand, changes of optical properties along with mechanical deformation of carbon nanotubes also make them useful as strain sensors. For example, Raman spectra are known to give shifted peaks when CNTs undergo stress or strain.[88,89] This phenomenon has been used to detect phase transitions and to measure stress fields in polymers with embedded nanotubes.[90,91]

Layer-by-layer (LbL) assembly is a technique based on electrostatic self-assembly of oppositely charged species to form ultrathin polymer films. This technique is applicable mainly to water-soluble charged materials, including polyelectrolytes, biopolymers, colloidal particles and other inorganic materials. This assembly technique can be used to create highly tuned, functional thin films with precise control of film composition and structure. Furthermore, it has been demonstrated that multilayer thin films can exist in a variety of novel and unique geometries and forms using patterning techniques, which make these systems even more applicable to the creation of hierarchical nanoassemblies.[92] Polyelectrolyte multilayers formed using this technique may contain a number of different functional groups, including electro-optic, electroluminescent, conducting, and dielectric layers. These functionalities allow interpreting optical, electrochemical, and conductive signals in response to different chemical or physical stimuli, making them excellent components for sensors and responsive membranes.

A major advantage of LBL assembly for fabricating membranes is the creation of robust, ultrathin multilayer films with high flexibility. These properties make them excellent candidates as nanoscale pressure sensor devices, which may not be realized with present microscale silicon membrane techniques.[93] For example, ultrathin deformable nanocomposite membranes composed of polyelectrolytes embedded with gold nanoparticles have shown extremely sensitive deflections to small pressure changes.[94] With its excellent mechanical strength and flexibility, carbon nanotubes represent most promising candidates for membrane sensor applications. In addition,

intrinsic semiconducting or metallic properties of carbon nanotubes will make it possible to detect electrical signals from external forces, leading to highly sensitive sensor devices compatible with integrated circuit techniques. Furthermore, bandgap engineering of carbon nanotubes with strain[76,77] suggests a possibility of fabricating CNT membranes with tunable metallic to semiconducting properties depending on the extent of deformation. LBL assembly of CNT/polyelectrolyte membranes can be an efficient method of fabricating extremely robust and flexible electronics, which composition and structure is finely tunable to the nanoscale.

In relation to chemical sensing applications, multilayer thin films can be used to protect active sensing parts, thus preventing interference from molecules which otherwise might make differentiation from the target molecule difficult. For example, significantly depressed permeabilities have been reported for O_2 and N_2 for poly(allyl amine)/poly(styrene sulfonate) (PAH/PSS) polyelectrolyte multilayers, whereas H_2 permeates readily through these films.[95] These semi-permeable properties of multilayer films can be applied to the carbon nanotube sensor devices capable of detecting molecules such as NO_2, NH_3, and O_2. By simply coating with proper polyelectrolyte multilayers for the target molecules, carbon nanotube sensor devices with high selectivity even in the mixture of different molecules could be created.

1.2.5.2. Carbon nanotube thin-film transistors

Carbon nanotubes (CNTs) have been studied intensely for a variety of applications due to their excellent structural, mechanical, electrical, and optical properties.

Besides their extremely small nanometer size with quasi one-dimensional geometrical dimensions, CNTs exhibit remarkable electrical conductivity, chemical and thermal stability, unusual high tensile strength and elasticity.[96] Numerous potential applications of CNT-based devices have been proposed including field-effect transistor,[97] field emitter,[98] and sensor devices.[99,100] Semiconducting CNTs have been known to exhibit p-type transistor characteristics with several orders of magnitude change in conductance under various gate voltages.[101] In particular, carbon nanotubes in thin-film transistor geometry will be desirable for realistic device applications because of limited current-carrying capacity of individual SWNTs and difficulties in controlling the electronic properties and spatial positions of each nanotube in FETs. Carbon nanotube thin-film transistors (CNT-TFTs) exhibit carrier mobilities (> 10 cm^2/Vs) more than an order of magnitude larger than the mobilities of organic semiconductors (typically < 1 cm^2/Vs).[102] In addition, both n- and p-type CNT transistors of comparable mobility can be produced[103] and molecular absorbates can be used to continuously tune the transistor threshold voltage.[104]

The two most important performance parameters of TFTs in device applications are carrier mobility and on/off ratio. The carrier mobility describes how easily charge carriers can move within the active layer and is, therefore, directly related to the switching speed of the device. The on/off ratio, defined as the ratio of the current in the 'on' and 'off' states, is indicative of the switching performance of TFTs. A low off current is desired to eliminate leakage while in the inactive state. The mobility of CNT-TFTs may be improved by increasing of the tube density or controlling the alignment of

CNTs. However, the efficient methods of controlling surface density and alignment of carbon nanotubes are not yet achieved. Another significant issue is achieving a low off-state current, which is hampered by the mixture state of metallic and semiconducting nanotubes. The on/off ratio may be enhanced dramatically by decreasing metallic tube contents with electrical breakdown procedures.[103] Also, several methods for separating semiconducting and metallic nanotubes have been suggested using chemical reactions.[105,106]

1.3. Gold nanoparticles

1.3.1. Optical Properties

The various colors on the glass windows found in the cathedrals are attributed to the presence of gold nanoparticles inside the glass. In addition, the color of the glass can be tuned by changing the shapes or sizes of the gold nanoparticles. These brilliant colors of gold nanoparticles are due to the surface plasmons, which are caused by the collective oscillations of free electrons on the surface of nanoparticles interacting with electromagnetic field of the incoming light, as schematically shown in Figure 1.7.[107,108]

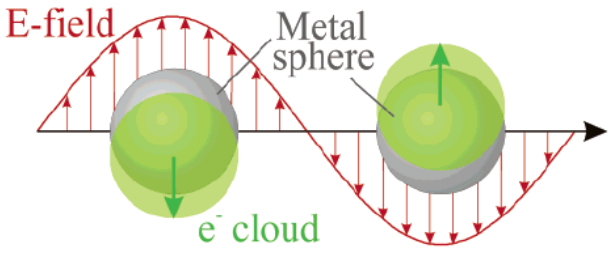

Figure 1.7. Schematic of plasmon oscillation for a sphere, showing the displacement of the conduction electron charge cloud relative to the nuclei. (From ref. 107)

Gold nanoparticles are known to have very unique size dependent optical properties due to the surface plasmon resonance. The frequency of surface plasmon resonance depends not only on the size, shape, and dielectric constant of the individual gold itself but also on the dielectric constant of surrounding medium and interparticle interations of plasmon coupling.[107,109] For example, Figure 1.8 shows the variations of surface plasmon resonances depending on the size, aspect ratio, and interparticle gaps. As the size of gold nanoparticle increases from 9 nm to 99 nm, the surface plasmon resonances red shift by 47 nm from 525 nm (Figure 1.8a). The change in aspect ratio of nanoparticles has more pronounced effects on the surface plasmon resonances, in which the change of aspect ratio from 1.94 to 3.08 results in red shift by 92 nm (Figure 1.8b). The interparticle gaps also affect to the surface plasmon resonance shift. When the two nanoparticles get closer to each other, the surface plasmon resonance red shifts and broadens as can be seen in Figure 1.8c.

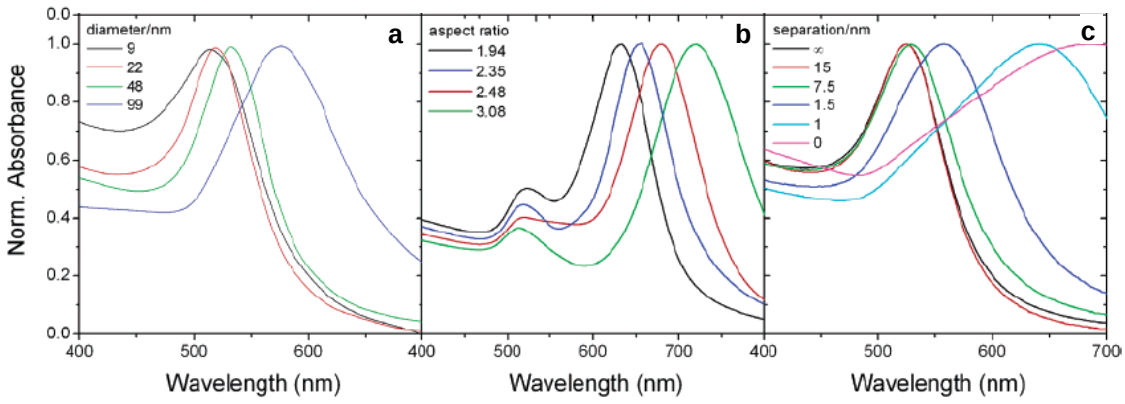

Figure 1.8. Experimental optical absorption spectra for (a) Au spheres, (b) Au nanorods, and (c) multilayer films of glass-coated Au spheres with varying interparticle distance. (From ref. 109)

In particular, the unique localized surface plasmons of gold nanoparitcles in the visible regime have directed many efforts to the study of surface-enhanced Raman scattering (SERS) for chemical sensing applications.[110] The main mechanism of SERS effects is considered to be due to the electromagnetic enhancement, which occurs when the incident light is in resonance with the surface plasmons of metal nanostructures. Therefore, tuning the surface plasmons from well-controlled metal nanoparticle arrays is crucial to the SERS-based chemical sensors. The other minor mechanism of SERS effects is the chemical enhancement, which is caused by the charge transfer complex between the adsorbed analyte and the metal. This charge transfer complex increases the probability of Raman transition by resonant excitation.

1.3.2. Assembly of Gold Nanoparticles

There have been intense researches of bottom-up assembly of metal nanoparticles into one- (1D), two- (2D) and three-dimensional (3D) nanostructure arrays by using methods such as simple drop-casting on appropriate surfaces or Langmuir-Blodgett techniques. Metal nanoparticles are usually capped or stabilized with ligand such as citrate or thiol molecules. The solution-based assembly of nanoparticles could create a variety of nanostructure arrays depending on the various parameters such as the types of capping ligands, ionic strength, interactions between the solvent and substrate, and deposition conditions. While many fundamental principles of assembling nanoparticles onto several planar surfaces have been understood, there remain many challenges for the device applications such as patterning of nanostructure arrays onto various substrates

including polymer surfaces, controlled inter-nanoparticle separations, and functionalization with different kinds of receptor molecules for sensing applications.

The intense research works of SERS promises highly sensitive sensors, but the outstanding challenge for the practical use of SERS-based sensor is the lack of robust and facile fabrication strategies for SERS substrates with huge Raman enhancement. Even though traditional SERS substrates such as electrochemically roughened metallic surfaces, colloidal metal nanoparticles, and metal island films can provide modest SERS enhancement,[111,112] the highly-ordered SERS substrates with reproducible, stable, and highly Raman-active geometries are needed for routine measurement of trace-level analytes by SERS-based sensors. With the help of modern nanotechnology to control nanoscale features and materials, much progress has been made on the reproducible production of highly ordered metallic nanostructures. Especially, the SERS on highly ordered metallic nanostructures is gaining more attention due to the extremely large SERS enhancement assisted by long-range optical effects.

Most of the previous studies of SERS-based chemical sensors involved the SERS substrates with randomly aggregated metal nanoparticles or roughened metal surfaces, which showed inconsistent data due to poor control of aggregates or surface structures. Recently, in order to fabricate reliable and highly SERS active substrates, several approaches of fabricating regular arrays of metal nanostructures have been demonstrated by using lithography techniques.[113] However, the precise control of the sub-10 nm gaps between the metal nanoparticles remains a big challenge. It has been known that the

small gaps (below 10 nm) between two metal nanoparticles or sharp metallic nanostructures generates "hot spots" (Figure 1.9), which are the result of very localized plasmon modes created by the strong electromagnetic coupling between two metal nanoparticles and these hot spots can enhance the Raman signal of a molecule up to 12 orders of magnitude.[114,115] In order to detect trace amount of chemicals, we need to maximize the Raman enhancement by optimizing the nanoparticle arrays. The precise control and tuning of the inter-particle gaps of the metal nanoparticle arrays will result in different conditions of collective plasmon coupling, which can in turn affect the SERS with a broad range of excitation from UV-Vis to NIR region.

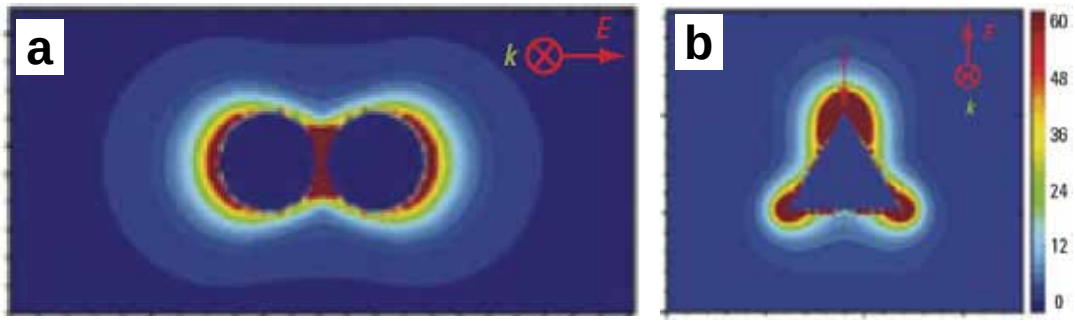

Figure 1.9. Theoretical simulations of the electromagnetic field enhancement around silver nanoparticles of (a) a triangular nanoparticle (700 nm), (b) a dimer of spherical nanoparticles (520 nm). (From ref. 115)

1.3.3. Applications of Surface-Enhanced Raman Spectroscopy

Since the demonstration of single molecule detection by SERS, there has been a tremendous interests in utilizing SERS in various sensing applications such as explosives,[116,117] chemical and biological warfare agents,[118] internal mechanical stresses [119,120,121] and toxic environmental pollutants.[122] The SERS-based sensors has been demonstrated to detect trace molecules due to their huge Raman enhancement up to 10^{14},

which is caused by electromagnetic enhancement of 10^{12} combined with chemical enhancement of 10^{2}.[123] In addition to this high sensitivity, the high speed testing, finger-print spectral signatures of analytes, no need for sample preparation, and the availability of portable systems for field analysis make SERS as strong candidate for sensing applications.

In all cases for SERS-active structures, the overall enhancement of optical response is based on few selected Raman bands. This has made SERS detection extremely ambiguous even for the analysis of simple mixtures. In order to exploit the SERS effect for trace detection in complicated mixture, much effort has been devoted toward the development of selective polymer coatings over metal nanostructurtes. The results indicate the polymer coatings not only increase sensitivity and selectivity of target molecules but also enhance chemical and mechanical stability of metal nanostructures. For example, the uptake and release of the target analytes through the molecularly imprinted polymer layers have been monitored by SERS.[124] Thiol-functionalized crown ether was anchored to silver electrode to selectively adsorb metal cations and detect SERS signal.[125] Cellulose acetate and Nafion (Perfluorosulfonate) coatings on roughened silver electrodes were employed not only to protect silver electrodes from protein adsorption but also to improve dopamine detection.[126] For SERS applications, the use of ultrathin polymer coating will be advantageous over the response time and also the sensitivity because most of the adsorbed analytes inside the polymer layer are within SERS active range. It has been known that the local electromagnetic fields exponentially decay with increasing distance from the metal surface.

The LbL assembly is advantageous in the creation of polymer coating layers for SERS sensors because LbL assembly can create ultrathin polymer layers with precisely controllable thickness (1~2 nm for each layer), film composition, and chemical functionalities.[127,128] The easy control of thickness (1~2 nm for each layer) and chemical functionalities of LbL films will be beneficial for increased selectivity and sensitivity in SERS-based sensors because the distance between adsorbed molecules and metal nanostructures can be controlled within several nanometer ranges by using ultrathin polymer coating layer. Even with its great potential for selective layers in sensing applications, there have been only a few examples of using LbL thin films as recognition layers to adsorb target analytes. For example, PEI was used for adsorption of methyl mercaptan (CH_3SH)[129] and PAH/PAA used for ammonia.[130]

1.4. References

[1] Dresselhaus, M. S.; Dresselhaus, G.; Eklund, P. C. *Science of fullerenes and carbon nanotubes*; Academic Press: San Diego, 1996.

[2] Dresselhaus, M. S.; Avouris, Ph. *Top. Appl. Phys.* **2001**, *80*, 1.

[3] Girifalco, L. A.; Hodak, M.; Lee, R. S. *Phys. Rev. B* **2000**, *62*, 13104.

[4] Krupke, R.; Hennrich, F.; Lohneysen, H. V.; Kappes, M. M. *Science* **2003**, *301*, 344.

[5] Chattopadhyay, D. Galeska, I.; Papadimitrakopoulos, F. *J. Am. Chem. Soc.* **2003**, *125*, 3370.

[6] Liang, W.; Bockrath, M.; Bozovic, D.; Hafner, J. H.; Tinkham, M.; Park, H. *Nature* **2001**, *411*, 665.

[7] Frank, S.; Poncharal, P.; Wang, Z. L.; de Heer, W. A. *Science* **1998**, *280*, 1744.

[8] Kelly, B. T. *Physics of Graphite*; Applied Science: London, 1981.

[9] Yu, M.-F.; Files, B. S.; Arepalli, S.; Ruoff, R. S. *Phys. Rev. Lett.* **2000**, *84*, 5552.

[10] Wong, E. W.; Sheehan, P. E.; Lieber, C. M. *Science* **1997**, *277***,** 1971.

[11] Salvetat, J. P.; Briggs, G. A. D.; Bonard, J. M.; Bacsa, R. R.; Kulik, A. J.; Stöckli, T.; Burnham, N. A.; Forro, L. *Phys. Rev. Lett.* **1999**, *82*, 944.

[12] Falvo, M. R.; Clary, G. J.; Taylor II, R. M.; Chi, V.; Brooks Jr, F. P.; Washburn, S.; Superfine R. *Nature* **1997**, *389*, 582.

[13] Hertel, T.; Martel, R.; Avouris, P. *J. Phys. Chem. B* **1998**, *102*, 910.

[14] Lin, M. F. *Phys. Rev. B* **2000**, *62*, 13153.

[15] O'Connell, M. J.; Bachilo, S. M.; Huffman, C. B.; Moore, V. C.; Strano, M. S.; Haroz, E. H.; Rialon, K. L.; Boul, P. J.; Noon, W. H.; Kittrell, C.; Ma, J. P.; Hauge, R. H.; Weisman, R. B.; Smalley, R. E. *Science* **2002**, *297*, 593.

[16] Liu, X.; Si, J.; Chang, B.; Xu, G.; Yang, Q.; Pan, Z.; Xie, S.; Ye, P.; Fan, J.; Wan, M. *Appl. Phys. Lett.* **1999**, *74*, 164.

[17] Saito, R.; Kataura, H. *Top. Appl. Phys.* **2001**, *80*, 213.

[18] Dresselhaus, M. S.; Eklund, P. C. *Adv. Phys.* **2000**, *49*, 705.

[19] Souza Filho, A. G.; Jorio, A.; Samsonidze, Ge. G.; Dresselhaus, G.; Saito, R.; Dresselhaus, M. S. *Nanotechnology* **2003**, *14*, 1130.

[20] Bonard, J.-M.; Stora, T.; Salvetat, J.-P.; Maier, F.; Stöckli, T.; Duschl, C.; Forro, L.; de Heer, W.A.; Chatelain, A. *Adv. Mater.* **1997**, *9*, 827.

[21] Bandow, S.; Rao, A. M.; Williams, K. A.; Thess, A.; Smalley, R. E.; Eklund, P. C. *J. Phys. Chem. B* **1997**, *101*, 8839.

[22] Bandow, S.; Asaka, S.; Ando, Y. *Appl. Phys. A* **1998**, *67*, 23.

[23] Duesberg, G. S.; Muster, J.; Krstic, V.; Burghard, M.; Roth, S. *Appl. Phys. A* **1998**, *67*, 117.

[24] Liu, J.; Rinzler, A. G.; Dai, H.; Hafner, J. H.; Bradley, R. K.; Boul, P. J.; Lu, A.; Iverson, T.; Shelimov, K.; Huffman, C. B.; Rodriguez-Macias, F.; Shon, Y.-S.; Lee, T. R.; Colbert, D. T.; Smalley, R. E. *Science* **1998**, *280*, 1253.

[25] Dujardim, E.; Ebbesen, T. W.; Krishnan, A.; Treacy, M. M. J. *Adv. Mater.* **1998**, *10*, 611.

[26] Rinzler, A. G.; Liu, J.; Dai, H.; Nikolaev, P.; Huffman, C. B.; Rodriguez-Macias, F. J.; Boul, P. J.; Lu, A. H.; Heymann, D.; Colbert, D. T.; Lee, R. S.; Fischer, J. E.; Rao, A. M.; Smalley, R. E. *Appl. Phys. A* **1998**, *67*, 29.

[27] Dillon, A. C.; Gennett, T.; Jones, K. M.; Alleman, J. L.; Parilla, P. A.; Heben, M. J. *Adv. Mater.* **1999**, *11*, 1354.

[28] Hirsch, A. *Angew. Chem. Int. Ed.* **2002**, *41*, 1853.

[29] Dujardin, E.; Ebbesen, T. W.; Krishnan, A.; Treacy, M. M. J. *Adv. Mater.* **1998**, *10*, 1472.

[30] Zhang, J.; Zou, H.; Qing, Q.; Yang, Y.; Li, Q.; Liu, Z.; Guo, X.; Du, Z. *J. Phys. Chem. B* **2003**, *107*, 3712.

[31] Kuznetsova, A.; Popova, I.; Yates, J. T.; Bronikowski, M. J.; Huffman, C. B.; Liu, J.; Smalley, R. E.; Hwu, H. H.; Chen, J. G. *J. Am. Chem. Soc.* **2001**, *123*, 10699.

[32] Zhao, W.; Song. C.; Pehrsson, P. E. *J. Am. Chem. Soc.* **2002**, *124*, 12418.

[33] Kukovecz, A.; Kramberger, Ch.; Holzinger, M.; Kuzmany, H.; Schalko, J.; Mannsberger, M.; Hirsch, A. *J. Phys. Chem. B* **2002**, *106*, 6374.

[34] Itkis, M. E.; Niyogi, S.; Meng, M. E.; Hamon, M. A.; Hu, H.; Haddon, R. C. *Nano Lett.* **2002**, *2*, 155.

[35] Hu, H.; Zhao, B.; Itkis, M. E.; Haddon, R. C. *J. Phys. Chem. B* **2003**, *107*, 13838.

[36] Iijima, S. *Nature* **1991**, *354*, 56.

[37] Iijima, S.; Ichihashi, T. *Nature* **1993**, *363*, 603.

[38] Bethune, D. S.; Kiang, C. H.; de Vries, M. S.; Gorman, G.; Savoy, R.; Vazquez, J.; Beyers, R. *Nature* **1993**, *363*, 605.

[39] Baughman, R. H.; Zakhidov, A. A.; de Heer, W. A. *Science* **2002**, *297*, 787.

[40] Tans, S. J.; Verschueren, A. R. M.; Dekker, C. *Nature* **1998**, *393*, 49.

[41] Rinzler, A.; Hafner, J. H.; Nikolaev, P.; Lou, L.; Kim, S. G.; Tomanek, D.; Nordlander, P. Colbert, D. T.; Smalley, R. E. *Science* **1995**, *269*, 1550.

[42] Dai, H.; Hafner, J. H.; Rinzler, A. G.; Colbert, D. T.; Smalley, R. E. *Nature* **1996**, *384*, 147.

[43] Wong, S. S.; Joselevich, E.; Woolley, A. T.; Cheung, C. L.; Lieber, C. M.; *Nature* **1998**, *394*, 52.

[44] Kong, J.; Franklin, M. R.; Zhou, C.; Chapline, M. G.; Peng, S.; Cho, K.; Dai, H. *Science* **2000**, *287*, 622.

[45] Collins, P. G.; Bradley, K.; Ishigami, M.; Zettl, A. *Science* **2000**, *287*, 1801.

[46] Tombler, T. W.; Zhou, C.; Alexseyev, L.; Kong, J.; Dai, H.; Liu, L.; Jayanthi, C. S.; Tang, M.; Wu, S. Y. *Nature* **2000**, *405*, 769.

[47] Vajtai, R.; Wei, B. Q.; Zhang, Z. J.; Jung, Y.; Ramanath, G.; Ajayan, P. M. *Smart Mater. Struct.* **2002**, *11***,** 691.

[48] Huang, S.; Mau, A. W. H.; Turney, T. W.; White, P. A.; Dai, L. *J. Phys. Chem. B* **2000**, *104*, 2193.

[49] Li, J.; Papadopoulos, C.; Xu, J. M.; Moskovits, M. *Appl. Phys. Lett.* **1999**, *75*, 367.

[50] Cai, L.; Bahr, J. L.; Yao, Y.; Tour, J. M. *Chem. Mater.* **2002**, *14*, 4235.

[51] Kong, J.; Zhou, C.; Morpurgo, A.; Soh, H. T.; Quate, C. F.; Marcus, C.; Dai, H. *Appl. Phys. A: Mater. Sci. Process* **1999**, *69*, 305.

[52] Huang, S.; Cai, X.; Liu, J. *J. Am. Chem. Soc.* **2003**, *125*, 5636.

[53] Krupke, R.; Hennrich, F.; Weber, H. B.; Beckmann, D.; Hampe, O.; Malik, S.; Kappes, M. M.; Lohneysen, H. V. *Appl. Phys. A* **2003**, *76*, 397.

[54] Ural, A.; Li, Y.; Dai H. *Appl. Phys. Lett.* **2002**, *81*, 3464.

[55] Fischer, J. E.; Zhou, W.; Vavro, J.; Llaguno, M. C.; Guthy, C.; Haggenmueller, R.; Casavant, M. J.; Walters, D. E.; Smalley, R. E. *J. Appl. Phys.* **2003**, *93*, 2157.

[56] Liu J.; Casavant, M. J.; Cox, M.; Walters, D. A.; Boul, P.; Lu, W.; Rimberg, A. J.; Smith, K. A.; Colbert D. T.; Smalley, R. E. *Chem. Phys. Lett.* **1999**, *303*, 125.

[57] Shimoda, H.; Oh, S. J.; Geng, H. Z.; Walker, R. J.; Zhang, X. B.; McNeil, L. E.; Zhou, O. *Adv. Mater.* **2002**, *14*, 899.

[58] Oh, S. J.; Cheng, Y.; Zhang, J.; Shimoda, H.; Zhou, O. *Appl. Phys. Lett.* **2003**, *82*, 2521.

[59] Burghard, M.; Duesberg, G.; Philipp, G.; Muster, J.; Roth, S. *Adv. Mater.* **1998**, *10*, 584.

[60] Gerdes, S.; Ondarcuhu, T.; Cholet, S.; Joachim, C. *Europhys. Lett.* **1999**, *48*, 292.

[61] Messer, B.; Song, J. H.; Yang, P. *J. Am. Chem. Soc.* **2000**, *122*, 10232.

[62] Li, H. W.; Muir, B. V. O.; Fichet, G.; Huck, W. T. S. *Langmuir* **2003**, *19*, 1963.

[63] Chou, S. Y.; Krauss, P. R.; Renstrom, P. J. *Appl. Phys. Lett.* **1995**, *67*, 3114.

[64] Chou, S. Y.; Krauss, P. R.; Renstrom, P. J. *Science* **1996**, *272*, 85.

[65] Zhao, X. M.; Xia, Y. N.; Whitesides, G. M. *Adv. Mater.* **1996**, *8*, 837.

[66] Kim, E.; Xia, Y. N.; Whitesides, G. M. *Nature* **1995**, *376*, 581.

[67] Beh, W. S.; Kim, I. T.; Qin, D.; Xia, Y. N.; Whitesides, G. M. *Adv. Mater.* **1999**, *11*, 1038.

[68] Kim, E.; Xia, Y. N.; Zhao, X. M.; Whitesides, G. M. *Adv. Mater.* **1997**, *9*, 651.

[69] Suh, K. Y.; Kim, Y. S.; Lee, H. H. *Adv. Mater.* **2001**, *13*, 1386.

[70] Qi, P.; Vermesh, O.; Grecu, M.; Javey, A.; Wang, Q.; Dai, H.; Peng, S.; Cho, K. J.; *Nano Lett.* **2003**, *3*, 347.

[71] Valentini, L.; Armentano, I.; Kenny, J. M.; Cantalini, C.; Lozzi, L.; Santucci, S. *Applied Physics Letters* **2003**, *82*, 961

[72] Kong, J.; Franklin, N. R.; Zhou, C. W.; Chapline, M. G.; Peng, S.; Cho, K. J.; Dai, H. J. *Science* **2000**, *287*, 622.

[73] Peng, S.; Cho, K. J. *Nanotechnology* **2000**, *11*, 57.

[74] Shimizu, Y.; Egashira, M. *MRS Bull.* **1999**, *24*, 18.

[75] Capone, S.; Mongelli, S.; Rella, R.; Siciliano, P.; Valli, L. *Langmuir* **1999**, *15*, 1748.

[76] Minot, E. D.; Yaish, Y.; Sazonova, V.; Park, J.-Y.; Brink, M.; McEuen, P. L. *Phys. Rev. Lett.* **2003**, *90*, 156401.

[77] Maiti, A. *Nat. Mater*. **2003**, *2*, 440.

[78] Yang, L.; Han, J. *Phys. Rev. Lett*. **2000**, *85*, 154.

[79] Li, Z.; Dharap, P.; Nagarajaiah, S.; Barrera, E. V.; Kim, J. D. *Adv. Mater*. **2004**, *16*, 640.

[80] Wood, J. R.; Frogley, M. D.; Meurs, E. R.; Prins, A. D.; Peijs, T.; Dunstan, D. J.; Wagner, H. D. *Journal of Physical Chemistry B* **1999**, *103*, 10388.

[81] Wood, J. R.; Wagner, H. D. *Applied Physics Letters* **2000**, *76*, 2883.

[82] Wood, J. R.; Zhao, Q.; Frogley, M. D.; Meurs, E. R.; Prins, A. D.; Peijs, T.; Dunstan, D. J.; Wagner, H. D. *Physical Review B* **2000**, *62*, 7571.

[83] Zhao, Q.; Wood, J. R.; Wagner, H. D. *Applied Physics Letters* **2001**, *78*, 1748.

[84] Zhao, Q.; Wood, J. R.; Wagner, H. D. *Journal of Polymer Science Part B-Polymer Physics* **2001**, *39*, 1492.

[85] Minot, E. D.; Yaish, Y.; Sazonova, V.; Park, J.-Y.; Brink, M.; McEuen, P. L. *Phys. Rev. Lett.* **2003**, *90*, 156401.

[86] Maiti, A. *Nat. Mater*. **2003**, *2*, 440.

[87] Li, Z.; Dharap, P.; Nagarajaiah, S.; Barrera, E. V.; Kim, J. D. *Adv. Mater*. **2004**, *16*, 640.

[88] Wood, J. R.; Frogley, M. D.; Meurs, E. R.; Prins, A. D.; Peijs, T.; Dunstan, D. J.; Wagner, H. D. *J. Phys. Chem. B* **1999**, *103*, 10388.

[89] Wood, J. R.; Wagner, H. D. *Appl. Phys. Lett.* **2000**, *76*, 2883.

[90] Wood, J. R.; Zhao, Q.; Frogley, M. D.; Meurs, E. R.; Prins, A. D.; Peijs, T.; Dunstan, D. J.; Wagner, H. D. *Phys. Rev. B* **2000**, *62*, 7571.

[91] Zhao, Q.; Wood, J. R.; Wagner, H. D. *Appl. Phys. Lett.* **2001**, *78*, 1748.

[92] Hammond, P. T. *Adv. Mater*. **2004**, *16*, 1271.

[93] Elwenspoek, M.; Wiegerink, R. Mechanical Microsensors; Springer, New York, **2001**.

[94] Jiang, C.; Markutsya, S.; Pikus, Y.; Tsukruk, V. V. *Nat. Mater*. **2004**, *3*, 721.

[95] Levasalmi, J. M.; McCarthy, T. J. *Macromolecules* **1997**, *30*, 1752.

[96] Baughman, R. H.; Zakhidov, A. A.; de Heer, W. A. *Science* **2002**, *297*, 787.

[97] Tans, S. J.; Verschueren, A. R. M.; Dekker, C. *Nature* **1998**, *393*, 49.

[98] Rinzler, A.; Hafner, J. H.; Nikolaev, P.; Lou, L.; Kim, S. G.; Tomanek, D.; Nordlander, P. Colbert, D. T.; Smalley, R. E. *Science* **1995**, *269*, 1550.

[99] Dai, H.; Hafner, J. H.; Rinzler, A. G.; Colbert, D. T.; Smalley, R. E. *Nature* **1996**, *384*, 147.

[100] Wong, S. S.; Joselevich, E.; Woolley, A. T.; Cheung, C. L.; Lieber, C. M.; *Nature* **1998**, *394*, 52.

[101] Avouris, P. *Acc. Chem. Res*. **2002**, *35*, 1026.

[102] Snow, E. S.; Novak, J. P.; Campbell, P. M.; Park, D. *Appl. Phys. Lett.* **2003**, *82*, 2145.

[103] Zhou, Y.; Gaur, A.; Hur, S.-H.; Kocabas, C.; Meitl, M. A.; Shim, M.; Rogers, J. A.; *Nano Lett.* **2004**, *4*, 1643.

[104] Star, A.; Han, T. R.; Gabriel, J. C. P.; Bradley, K.; Gruner, G. *Nano Lett.* **2003**, *3*, 1421.

[105] Chattopadhyay, D.; Galeska, I.; Papadimitrakopoulos, F. *J. Am. Chem. Soc.* **2003**, *125*, 3370.

[106] Strano, M. S.; Dyke, C. A.; Usrey, M. L.; Barone, P. W.; Allen, M. J.; Shan, H. W.; Kittrell, C.; Hauge, R. H.; Tour, J. M.; Smalley, R. E. *Science*, **2003**, *301*, 1519.

[107] Kelly, K. L.; Coronado, E.; Zhao, L. L.; Schatz, G. C. *J. Phys. Chem. B* **2003**, *107*, 668.

[108] Burda, C.; Chen, X.; Narayanan, R.; El-Sayed. M. A. *Chem. Rev.* **2005**, *105*, 1025.

[109] Liz-Marzan, L. M. *Langmuir*, **2006**, 22,32.

[110] Baker, G. A.; Moore, D. S. *Anal. Bioanal. Chem.* **2005**, *382*, 1751.

[111] Vo-Dinh, T. *Trends Anal. Chem.* **1998**, *17*, 557.

[112] Baker, G. A.; Moore, D. S. *Anal. Bioanal. Chem.* **2005**, *382*, 1751.

[113] Hulteen, J. C.; Treichel, D. A.; Smith, M. T.; Duval, M. L.; Jensen, T. R.; Van Duyne, R. D. *J. Phys. Chem. B* **1999**, *103*, 3854.

[114] Imura, K.; Okamoto, H.; Hossain, M. K.; Kitajima, M. *Nano Lett.* **2006**, *6*, 2173

[115] Hao, E.; Schatz, G. C. *J. Chem. Phys.* **2004**, *120*, 357.

[116] Sylvia, J. M.; Janni, J. A. ; Klein, J. D. ; Spencer, K. M. *Anal. Chem.* **2000**, *72*, 5834.

[117] Tao, A.; Kim, F.; Hess, C.; Goldberger, J.; He, R.; Sun, Y.; Xia, Y.; Yang, P. *Nano. Lett.* **2003**, *3*, 1229.

[118] Haynes, C. L.; Yonzon, C. R.; Zhang, X. Y.; Van Duyne, R. P. *J. Raman Spectrosc.* **2005**, *36*, 471.

[119] Jiang, C.; Lio, W. Y.; Tsukruk, V. V. *Phys. Rev. Lett.,* **2005,** *95*, 115503.

[120] Jiang, C.; Ko, H.; Tsukruk, V. V. *Adv. Mater.* **2005,** *17*, 2127.

[121] Ko, H.; Pikus, Y.; Jiang, C.; Jauss, A.; Hollricher, O.; Tsukruk, V. V. *Appl. Phys. Lett.,* **2004**, *85,* 2598.

[122] Olson, L. G.; Uibel, R. H.; Harris, J. M. *Appl. Spectrosc.* **2004**, *58*, 1394.

[123] Kneipp, K.; Kneipp, H.; Itzkan, I.; Dasari, R. R.; Feld, M. S. Chem. Rev. **1999**, *99*, 2957.

[124] Kostrewa, S.; Emgenbroich, M.; Klockow, D.; Wulff, G. *Macromol. Chem. Phys.* **2003**, *204*, 481

[125] Heyns, J. B.; Sears, L. M.; Corcoran, R. C.; Carron, K. T. *Anal. Chem.* **1994**, *66*, 1572

[126] Mcglashen, M. L.; Davis, K. L.; Morris, M. D. *Anal. Chem.* **1990**, *62*, 846

[127] Hammond, P. T. *Adv Mater* **2004,** *16*, 1271.

[128] Jiang, C. Y.; Tsukruk, V. V. *Adv Mater* **2006,** *18*, 829.

[129] KiKuchi, M.; Shiratori, S. *Sens. Actuators B* **2005**, *108*, 564

[130] Kim, J. H.; Kim, S. H.; Shiratori, S. *Sens. Actuators B* **2004**, *102*, 241.

Chapter 2. Experimental Section: Materials and Methods

2.1. Materials

2.1.1. Carbon Nanotubes

The carbon nanotubes (CNTs), produced by the arc discharge method, was purchased from MER Corporation (Arizona, U.S.A.). The raw material was in the state of black powder and composed of about 12 wt % single-walled carbon nanotubes (SWNTs) (1.2 – 1.4 nm in diameter, 10 – 50 μm in length, bundles of up to 20 nanotubes), along with other impurities including metal catalyst particles, amorphous carbon, and fullerenes. To remove impurities and oxidize the CNT, mutlti-step purification have been conducted.

The multi-step purification procedure applied here involves oxidation in nitric acid, centrifugation, and filtration. Sodium dodecyl sulfate (SDS) surfactant (Aldrich) was used to make stable colloidal suspension of SWNTs. First, 50 mg of raw material was refluxed in 50 ml of 3 M HNO_3 solution for 48 h at 100 ^{o}C. After the refluxed material was centrifuged for 30 min at 3300 rpm, the red-brownian supernatant acid was decanted off. The trapped acid in the sediment was removed by repeatedly (3–4 times) re-suspending the sediment in water (sonication for 2 min), centrifuging, and decanting the supernatant. Next, the sediment was dispersed in 20 ml of 1 wt% aqueous SDS solution by sonication for 1 h. Immediately after sonication, the resulting dispersion was centrifuged at 3300 rpm for 3 h and the sediment of un-dispersed large aggregates was removed. Finally, the suspension was filtered with polycarbonate membranes (0.4 μm pore size, Millipore) for the removal of remaining small impurities. After filtration, the

residue on the filter was scraped and dispersed in 10 ml of 1 wt% SDS surfactant by sonication for 1 h. Subsequently, large aggregates of SWNTs in this suspension were removed by centrifugation at 3300 rpm for 1 h. The resulting black supernatant was kept in a clean vial for future experiments.

For the assembly of CNTs on the polyelectrolyte multilayers, oxidized CNTs without surfactant was prepared. Single-walled carbon nanotubes (SWNT), produced by arc discharge method, were purchased from Carbolex (Lexington, KY). Carbon nanotubes were purified by oxidation in dilute nitric acid (3 M, 45 h), filtration (0.4 μm pore size), and taking supernatant after high-speed centrifugation (18000 rpm, 1 h). Metastable dispersion of oxidized SWNTs in aqueous solution (without surfactant) was prepared by sonication (Bath sonicator, 1 h) in Nanopure water (18 MΩ cm). Due to the carboxylic acid groups on the walls and ends after oxidation, carbon nanotubes are negatively charged under normal pH conditions.

2.1.2. Gold Nanoparticles

For the patterned assembly of gold nanoparticles on the LbL multilayers, gold nanoparticles (13 nm in diameter) were synthesized using $HAuCl_4$ solution as described elsewhere.[1,2] The gold nanoparticles have modest negative charges under normal pH conditions and can be used for electrostatic surface deposition without further modification. For gold nanoparticle assembly on the porous alumina membranes, gold nanoparticles (32 nm in diameter) capped with cetyltrimethylammonium bromide (CTAB) were prepared by seed growth method following the literature procedure.[3]

2.1.3. Polyelectrolyte Multilayers

Poly(allylamine hydrochloride) (PAH) and poly(sodium 4-styrenesulfonate) (PSS) were purchased from Aldrich. The nanomembranes were fabricated with spin-assisted layer-by-layer (LbL) from polyelectrolyte bilayers and a central nanomaterial-containing layer. For LbL deposition, PAH (0.2wt.%) and PSS (0.2wt.%) solutions were prepared with Nanopure water (18 MΩ cm). The general formula is $(PAH\text{-}PSS)_n$PAH/CNT/$(PAH\text{-}PSS)_n$PAH or (nCNTn) for CNT central layer, where n is the number of polymer bilayers.

2.1.4. Silicon Substrate

The (100) silicon wafers (Semiconductor Processing) were cut in rectangular pieces of approximately 1×2 cm. They were cleaned in Nanopure water in an ultrasonic bath for 10 min, immersed in a piranha solution (3:1 concentrated sulfuric acid:30 % hydrogen peroxide, health hazard) for 1 h to re-grow the oxide layer, and then rinsed several times with water (18 MΩ cm, Nanopure). After rinsing, the substrates were dried under a stream of nitrogen and stored in sealed containers.

2.2. Methods

2.2.1. Atomic Force Microscopy (AFM)

AFM scanning was performed in the tapping mode with a Dimension 3000 (Digital Instruments, Inc.) microscope under ambient conditions according to the usual experimental procedure adopted in our laboratory.[4] Topographical and phase AFM

images were acquired at scan rates in the range of 0.5–1.0 Hz and a set-point amplitude ratio of about 0.8–0.9, which corresponds to the light tapping regime. Silicon cantilevers with spring constant of about 50 N/m and tip radii of 10–20 nm were used as verified by resonance frequency and a gold nanoparticle reference sample, respectively.[5]

2.2.2. Raman Spectroscopy

Confocal Raman microscope CRM 200 (WITec, Germany) was taken on the patterned assembly of carbon nanotubes. The 532 nm line of a Nd:YAG laser was used as the exitation. The image was acquired line by line with Avalanche photodiode detector (APD) in single photon counting mode by fast imaging. The optical resolution of confocal optical microscope is 350 nm in lateral and 900 nm in axial. In this work, we also used combined atomic force/near field/confocal scanning microscope which is based on the design of Aurora-3 NSOM (Topometrix/Veeco). The system allows simultaneous acquisition of high-resolution topography and Raman images for transparent sample. Topography was measured in Aurora's standard shear-force AFM mode and the Raman imaging was achieved by confocal scanning mode. A Nd:YAG laser with 532 nm was used as exitation. A CCD camera (Princeton Instruments/ Roper Scientific) was used to collect the spectra at every point of the sample. After data acquisition, images can be calculated from the spectra for any desired Raman energy.

The Raman spectra of DNT on SERS substrates were recorded with a Holoprobe Raman microscope (Hololab series 5000 spectrometer, Kaiser Optical Systems, Inc) with back-scattered configuration using a 10× objective lens. The excitation laser is diode

laser with 785 nm wavelength and the power is 20 mW to the sample. The collection time is 20 sec with no accumulation and three points were averaged for each sample.

2.2.3. Semiconductor Parameter Analyzer

The semiconducting properties of carbon nanotube transistors were measured by using HP 4155 semiconductor parameter analyzer. The device test was performed for 5–7 devices for each channel length and presented as average values. The channel lengths of 2.5, 5, 10, 20, 40 μm were used for CNT transistors. The current-voltage (I–V) characteristics were measured at ambient laboratory conditions.

2.2.4. Scanning Electron Microscopy (SEM)

A field-emission scanning electron microscopy (FESEM, LEO 1530) was used to investigate the assembled structures of gold nanoparticles decorating porous alumina membranes. For this test, the samples were mounted on silicon substrate by using conductive carbon tape and gold sputtered lightly. The operating voltage is 5-10 KeV.

2.2.4. UV-Vis-NIR Spectroscopy

UV-Vis-NIR optical absorption spectra of the colloidal gold were measured with AvaSpec-2048 Fiber Optic Spectrometer (Avantes). For nanocanal arrays decorated with gold nanoparticles, was used to measure the transmission and absorption spectra. Transmission and absorption spectra of the nano-canal arrays decorated with gold

nanoparticles were measured using an optical microscope (Leica DM4000M) equipped with a Craig QDI 202 point-shot spectrophotometer.

2.3. References

[1] Grabar, K. C.; Freeman, R. G.; Hommer, M. B.; Natan, M. J. *Anal Chem*. **1995**, *67*, 735.

[2] Jiang, C.; Markutsya, S.; Tsukruk, V. V. *Langmuir* **2004**, *20*, 882.

[3] Kwon, K.; Lee, K. Y.; Lee, Y. W.; Kim, M.; Heo, J.; Ahn, S. J.; Han, S. W. *J. Phys. Chem. C* **2007**, 111, 1161.

[4] Tsukruk, V. V.; Reneker, D. H. *Polymer* **1995**, 36, 1791.

[5] Hazel, J. L.; Tsukruk, V. V. *Thin Solid Films* **1999**, 339, 249.

Chapter 3. Patterned Carbon Nanotube Arrays

3.1. Introduction

As attractive building blocks for molecular electronics, carbon nanotubes (CNTs) have been studied intensely due to their unique structural, mechanical, electrical and optical properties.[1] Numerous potential applications of CNT-based nanodevices have been proposed including field-effect transistor,[2] field emitter,[3] probe tips,[4,5] chemical sensors,[6,7] and electromechanical sensor.[8] In order to utilize CNTs in nanodevices, it is necessary to develop efficient strategies for their assembling into hierarchical nanostructures, which could be achieved by controlling the shape, location, and orientation of large nanotube arrays.

Self-organization of CNTs into highly ordered arrays has been approached by direct-growth assembly or post-growth assembly methods. Significant progress in growing vertically aligned nanotube assemblies on patterned substrates has been made recently with pre-catalyst patterning and chemical vapor deposition (CVD).[9,10,11,12,13] Direct-growth assembly by CVD has the advantage of achieving highly ordered and densely packed nanostructures. However, functionalized CNTs can be damaged by the high-temperature CVD process or cannot be synthesized by current CVD methods. Post-growth assembly of CNTs in a vertical direction has been demonstrated by the deposition of CNTs from suspension onto chemically modified surfaces.[14] On the other hand, several in-plane orientation methods have been reported, such as catalytic growth,[15,16] alignment in electric and magnetic fields,[17,18,19] and self-assembling on chemically

modified surfaces. [20,21,22,23,24] Among all these approaches, self-assembly based on wet chemistry has received great attention recently because of the associated mild conditions and the ability to produce well-defined nanostructures.

The CNT assemblies anchored to chemically modified surfaces are likely to be under different mechanical stresses caused by a combination of capillary and surface forces resulting in their stretching, twisting, and bending.[25,26,27] Recently, it was reported that the mechanical deformation of CNTs strongly affects their electronic properties.[28,29] It has been demonstrated that the mechanical strain can open a band gap in a metallic CNT and modify the band gap in a semiconducting CNT. Confocal Raman imaging and spectroscopy have shown that CNT structure may change along the tube axis possibly due to external stress or local defects in the tube structure.[30,31,32] However, very little is revealed on the related optical properties of stressed nanotubes and *direct acquisition* for individual CNTs and their bundles under stress conditions was not demonstrated.

The relation between the Raman spectra and the basic structure of carbon nanotubes are intensely investigated and the nature of all major adsorption bands is well understood.[33] For CNT composites, it was reported that compressive strain can induce frequency shift of Raman G-modes of SWNTs/epoxy composites subjected to bending.[34] However, these studies relied on the measurements of bulk CNT materials and their composites in which the transfer of mechanical stresses and actual shape of the stressed CNTs remain unknown to great extent. Raman studies of bulk CNT materials demonstrated frequency upshift with increasing compressive strain under hydrostatic pressure.[35,36]

In this study, we demonstrate that wet-chemistry approaches (a combination of surface patterning and dip-coating) can be used to produce a massive amount of nanotube arrays assembled on the patterned silicon wafer surfaces. This approach provided not only uniform orientation but also well-defined spacing in nanotube positioning on a micron scale controlled by the dimensions of the hydrophilic and hydrophobic patterned surface areas. We propose that the dewetting of the liquid film is responsible for the uniform nanotube alignment. In addition, we use a direct collection of Raman spectra from CNT arrays with precise localization of the probed area as monitored with atomic force microscopy (AFM), and confocal Raman microscopy.

3.2. Sample preparation

3.2.1. Microcontact Printing

Microcontact printing (μCP) was used for the patterning of self-assembled monolayers (SAMs) on a silicon oxide surface. A poly(dimethylsiloxane) (PDMS, Dow Chemical) stamp was cured at 60 ^{o}C for 1 hr in vacuum and released from a patterned mold of the highly-polished micromachined silicon grid (10 μm pitch, Micromash). For surface patterning, an octadecyltrichlorosilane (OTS, Figure 3.1.b) (Aldrich) toluene solution was used as ink. Aminopropyltriethoxysilane (APTS, Figure 3.1.c) (Aldrich) SAM containing amine-terminated groups with the high ability to attract carboxylic groups was used to form hydrophilic stripes on the silicon oxide surface.

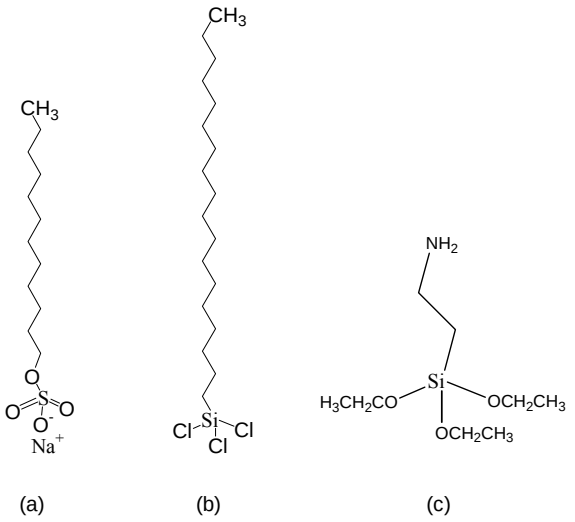

Figure 3.1. Chemical structures of molecules used in this study: (a) Sodium dodecyl sulfate (SDS) surfactant for stable suspension of CNTs, (b) hydrophobic monolayer of methyl-terminated octadecyltrichlorosilane (OTS), (c) hydrophilic monolayer of amine-terminated aminopropyltriethoxysilane (APTS).

The procedure for μCP is shown schematically in Figure 3.2. For the preparation of OTS patterned SAM, the PDMS stamp was immersed into the 0.5 vol.% OTS solution in toluene to ink its surface inside the nitrogen-purged glove box (< 5 % RH), removed outside the glove box in OTS solution, dried with a stream of nitrogen for 30 s, and then brought in contact with the cleaned silicon substrate for 30 s in ambient conditions. After each printing, the PDMS stamp was sonicated in toluene and ethanol for 2 min each and dried with a stream of nitrogen for 1 min to remove contaminations. The patterned samples were rinsed with chloroform and dried with a stream of nitrogen. To amine-terminate, the bare silicon surface areas were backfilled with APTS by immersion in a 1.0 vol.% APTS solution in toluene for 10 min after 1 h hydrolysis of APTS solution inside the nitrogen-purged glove box. Samples were then rinsed with chloroform and dried with nitrogen. All procedures were conducted under cleanroom class 100 conditions to prevent contaminations with external impurities.

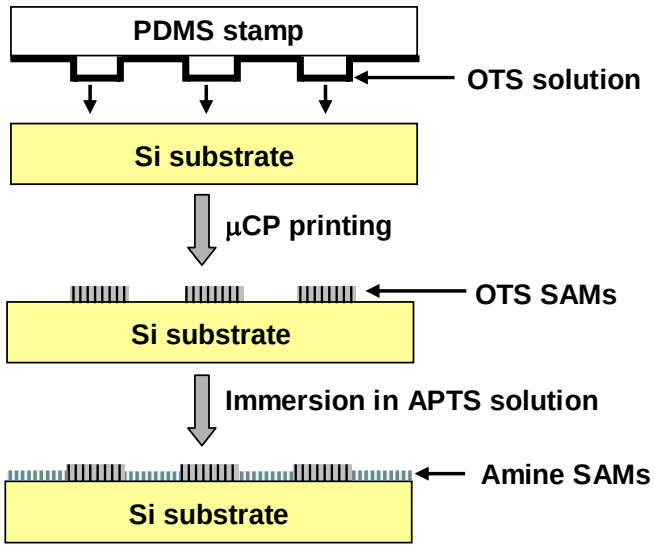

Figure 3.2. Surface patterning by microcontact printing technique showing printing of methyl-terminated OTS SAM followed by backfilling with amine-terminated SAM.

3.2.2. Assembly of Carbon Nanotubes

Figure 3.3 shows schematically the process of CNT deposition by dip-coating and casting from solution. For dip-coating process (Figure 3.3a), patterned substrates were immersed horizontally in carbon nanotube solution for about 24 hours, rinsed briefly (~ 30 s) in water, dry-immobilized in ambient laboratory conditions and rinsed several times in water. To exclude any other factors affecting the alignment, we did not use nitrogen gas when drying the samples. The substrates were withdrawn from a rinsing bath and dried vertically. Withdrawing rate was 10–20 mm/s for all the case. CNTs are immobilized on the substrates in the drying step, so the alignment direction is determined in the drying step. After nanotubes deposition, the substrates were stored in a desiccator under dry air conditions before AFM studies.

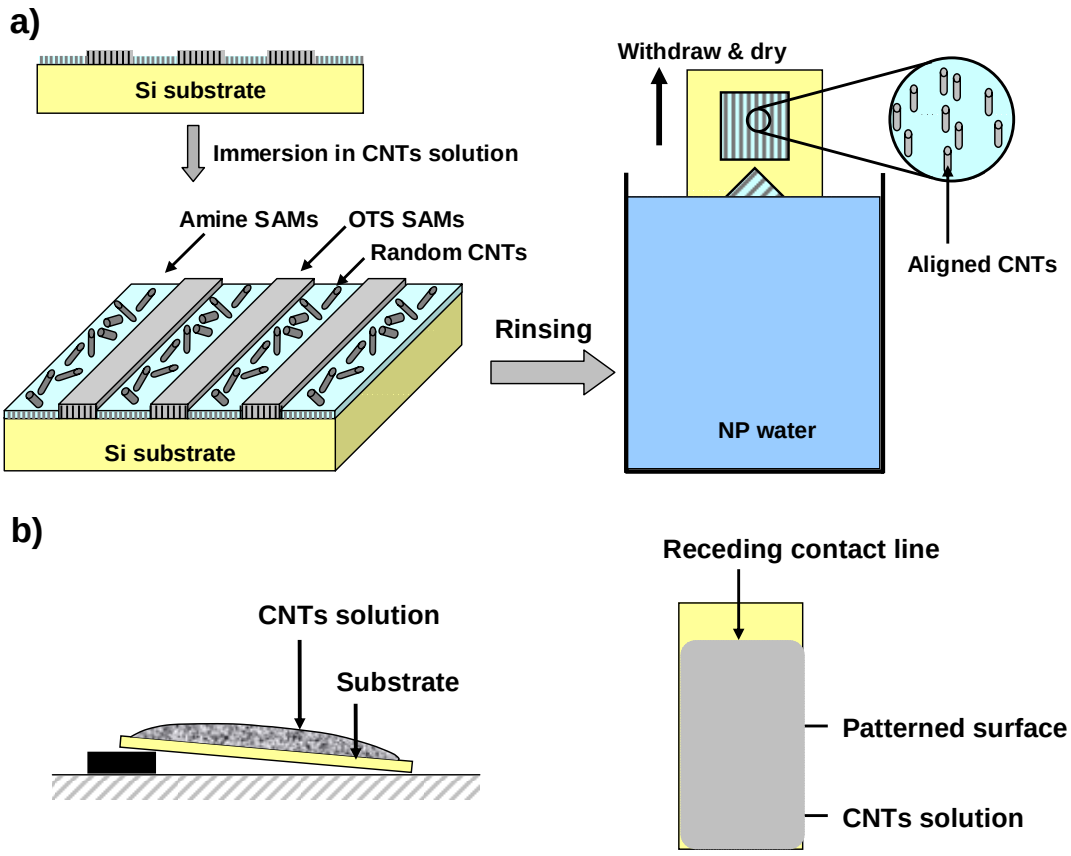

Figure 3.3. Schematic illustration of the nanotube adsorption from solution on amine-terminated SAM stripes. (a) Dip-coating process: Patterned substrates are immersed horizontally in CNT solution. CNTs randomly attach on amine-terminated stripes during immersion. The substrates are withdrawn vertically from the rinsing reservoir after brief rinsing and dried vertically at cleanroom class 100 conditions. Ordered array of carbon nanotubes form during drying step. (b) Drop-casting of CNT solution on patterned substrates. As the solvent evaporates, the CNTs are adsorbed along with receding contact line, forming densely packed array of CNTs.

For the drop-casting of CNT solution (Figure 3.3b), several drops of CNT solution were spread on a patterned substrate and allowed to dry at cleanroom class 100 conditions. The substrate was tilted slightly (~5^{o}) for the unidirectional fluidic flow. After the solvent was completely evaporated, the substrate was rinsed thoroughly with deionized water and dried in cleanroom.

3.3. Results and Discussion

3.3.1. Patterned SAMs by Microcontact Printing

For the selective deposition of purified nanotubes, we prepared chemically heterogeneous surfaces with well-defined periodicity via the microcontact printing technique as was discussed above (Figure 3.4). The micropatterned surface is composed of alternating hydrophilic and hydrophobic stripes: hydrophilic amine-terminated ($–NH_2$) SAMs with the ability for strong grafting of carboxyl-functionalized carbon nanotubes, and hydrophobic methyl-terminated ($–CH_3$) SAMs with weak adsorbing ability for various chemical groups.[37] As can be seen in Figure 3.4, the hydrophilic amine-terminated surface areas are represented by darker stripes of 7 μm width on AFM topographical images. White stripes of about 3 μm across represent thicker hydrophobic methyl-terminated areas (with about 1.2 nm difference in thickness as measured by AFM and expected for these SAMs[38]).

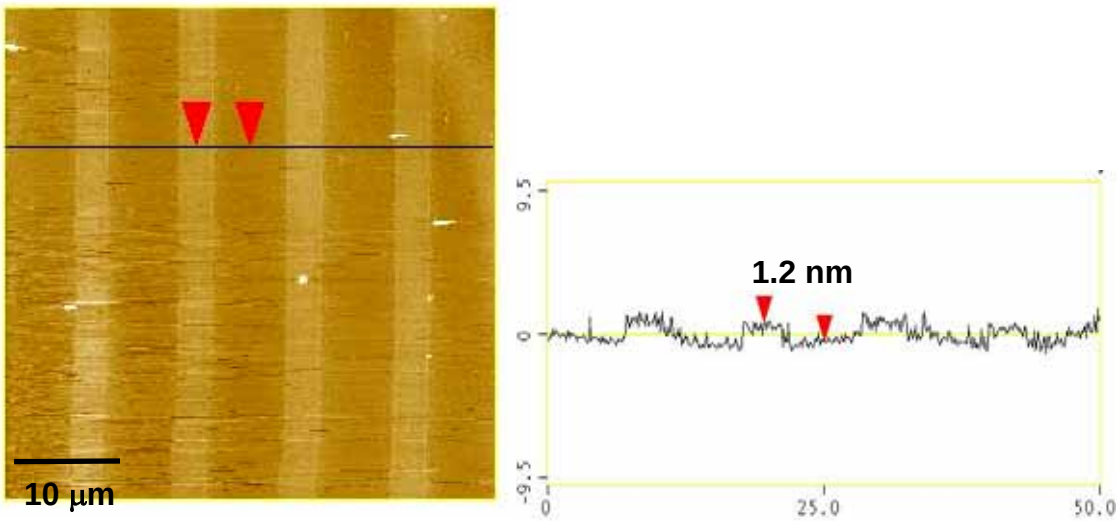

Figure 3.4. Patterned substrate with alternating hydrophilic amine-terminated stripes (dark) and hydrophobic methyl-terminated stripes (bright). The differences in thickness between these SAMs are usually 1.2 nm.

3.3.2. CNT Arrays by dip-coating

Dip-coating of CNT solution on patterned substrates (10 μm parallel lines) resulted in a monolayer of less dense carbon nanotubes firmly attached to the amine-terminated SAM surface (Figure 3.5). This tethering is facilitated by electrostatic attraction, occasional chemical bonding, and strong van der Waals interactions.[39] The majority of carbon nanotubes deposited on the patterned substrates with vertical or parallel to the drying direction, formed ordered nanotube arrays on stripes of amine-terminated SAMs with high selectivity. In fact, very few nanotubes can be found on hydrophobic stripes. The deposition of carbon nanotubes on un-patterned amine-terminated surface results in randomly oriented nanotubes without any indication of orientational ordering. These results demonstrate a critical importance of the surface patterning for the formation of regularly oriented arrays of carbon nanotubes.

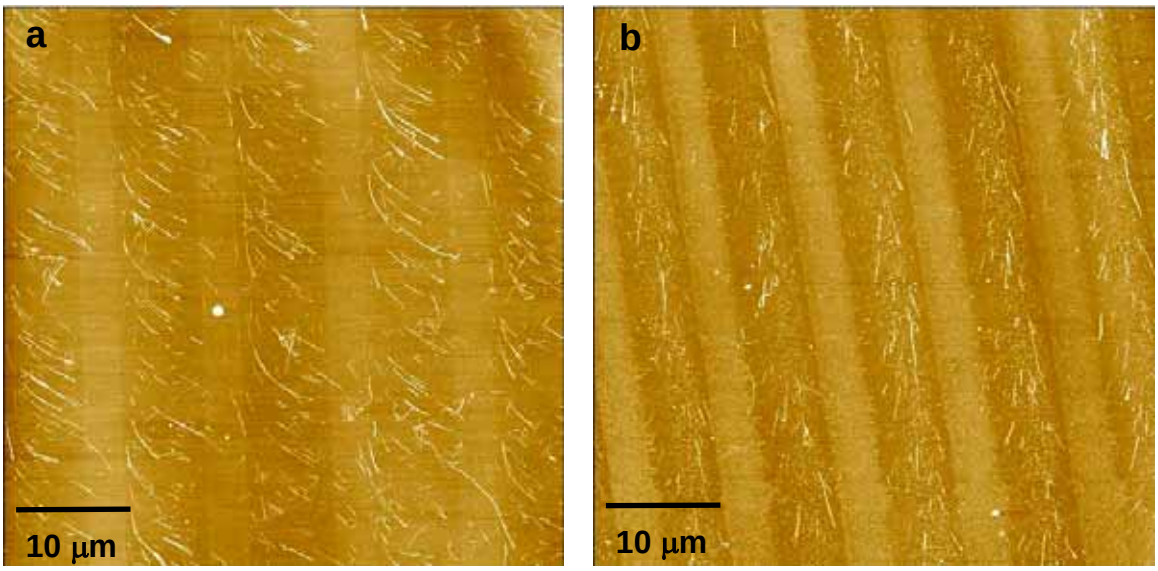

Figure 3.5. AFM topographical images of ordered arrays of carbon nanotubes obtained by dip-coating on the patterned substrates with patterned silicon substrates.

We propose that the dewetting of stripped liquid film confined to the hydrophilic stripes is responsible for the alignment of CNTs in the drying process. When the substrate is withdrawn vertically from a rinsing bath, an ultrathin liquid film is formed on the withdrawn substrate.[40] As known, during drying process of the liquid film on the tilted/vertical substrate under the unidirectional gravitational force, the downwardly dewetting liquid film exerts a hydrodynamic drag force and the receding contact line of this dewetting film exerts a surface tension force.

During initial immersion of the substrate in nanotube solution, freely floating nanotubes are randomly attached to the amine-terminated surface mainly by their functionalized nanotube ends. Also, nanotube sidewalls can be tethered to the amine-terminated surface via electrostatic interactions facilitated by SDS surfactant linkers. It can be expected that tethered nanotubes are mobile in the solution as the surfactant molecules are removed in the course of careful rinsing, which may cause nanotube orientation by external forces. After a brief rinsing, when the substrate is withdrawn from the rinsing reservoir, the meniscus moves upward with the substrate forming a thin liquid film. This liquid film dewets instantaneously on OTS-covered stripes because of their hydrophobicity, thus forming a stripped flow pattern concentrated along the hydrophilic stripes. As the liquid film is drying, the dewetting liquid film exerts a hydrodynamic drag force on the anchored nanotubes. Also, the receding contact line exerts a downward local force on the immersed part of each anchored nanotube, while the emerged nanotubes remain immobilized to the substrates.

3.3.3. CNT Arrays by Drop-Casting

As described in experimental section, directed casting was performed on patterned substrates with tilt. Directed casting from solution followed by gentle rinsing resulted in the formation of densely packed arrays of carbon nanotubes (Figure 3.6). The average thickness of these woven nanotube stripes stays within 10–20 nm that indicates multilayered character of the adsorbed material composed of several (3–8) layers of nanotube bundles. As shown in Figure 3.6, very few carbon nanotubes can be found on the hydrophobic surface areas even without rinsing, which demonstrate the high selectivity of the adsorbing process. CNT patterns are very regularly spaced (see sharp, pointlike rows of Fourier transform in Figure 3.6a), repeatedly reproduced along the stripes, and consistently observed for all stripes over millimeter size surface areas under given casting conditions.

The local orientation of carbon nanotube assemblies within these arrays is very uniform with nematic-like ordering of densely packed straight nanotubes expanding over microscopic areas, as can be seen with AFM phase image and 2D Fourier transform image in Figure 3.6d. It is likely that the local nematic ordering with uniform orientational ordering and no positional ordering is caused by higher lateral capillary forces along the length of a nanotube as compared to its width.[41] Before, similar mechanism of nanotubes nucleation was described in detail by Zhou et al.[42]

The mechanism responsible for nanotube arrays prepared by casting of CNT solution is obviously different from that for arrays prepared by dip-coating. For dip-

coating process, nanotubes are adsorbed during immersion, and then aligned during drying process. However, for casting process, nanotubes adsorption and alignment arise at the same time, resulting in highly packed nanotube arrays. In the process of casting on tilted surface, the liquid film of CNT solution spontaneously sweeps down at the patterned area (less wettable), making the solution locally very concentrated and confined to the hydrophilic stripes. Successive drying of this liquid film causes nanotubes deposition by nucleation along the contact line.

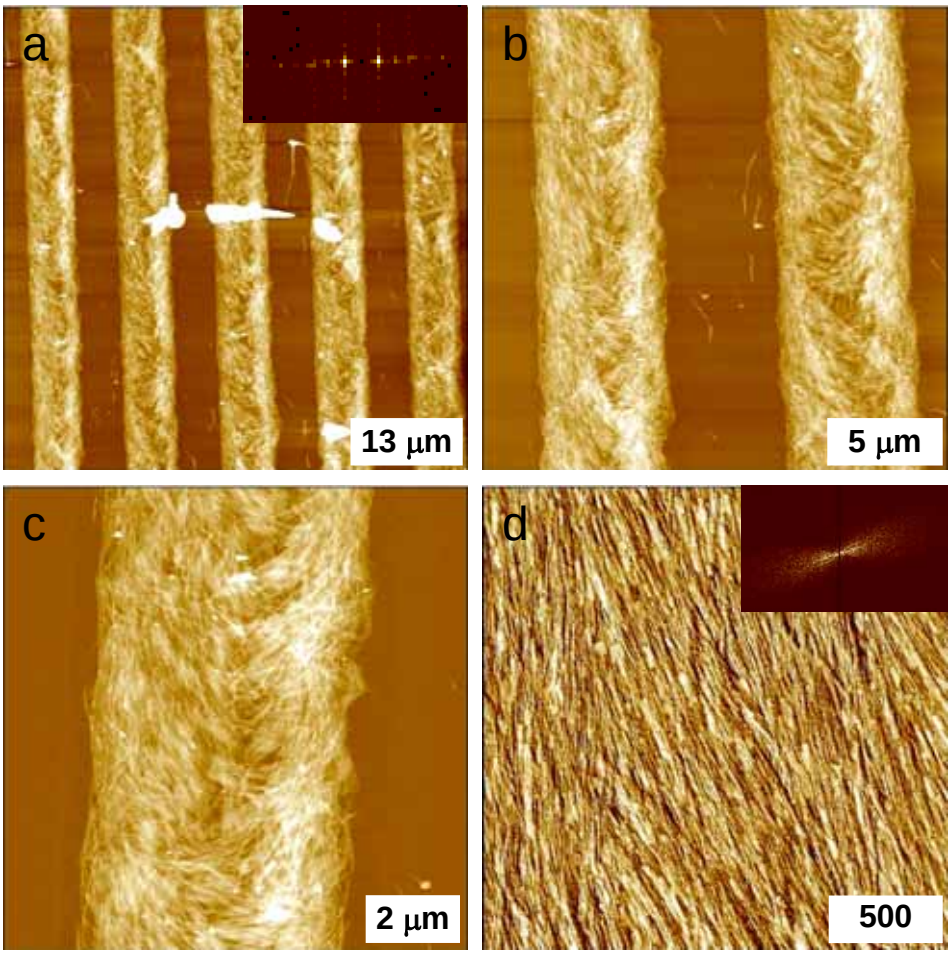

Figure 3.6. AFM topographical images with different scan sizes of highly-packed CNT arrays on amine-terminated stripes obtained by casting of CNT solution on patterned substrates. d) AFM phase image of nematic-like ordering of carbon nanotubes. The inset in (a) and d) shows 2-D Fourier-transform.

Here, we suggest that the formation of highly textured dense nanotube arrays is facilitated by vertical hydrodynamic forces causing initial orientation of carbon nanotubes along the hydrophilic stripes. Further formation of the orientation texture is controlled by the receding contact line, which aligns all carbon nanotubes perpendicular to the meniscus according to detailed studies on combing process for rod-like molecules such as DNA.[43] It is likely that the local nematic-like ordering is caused by higher lateral capillary forces along the length of a nanotube as compared to its width. This mechanism is virtually identical to that suggested for DNA combing with the only significant difference being a manner of the creation of microfluidic patterned flow not within closed microchannels, but directly on an open patterned surface of silicon wafers.

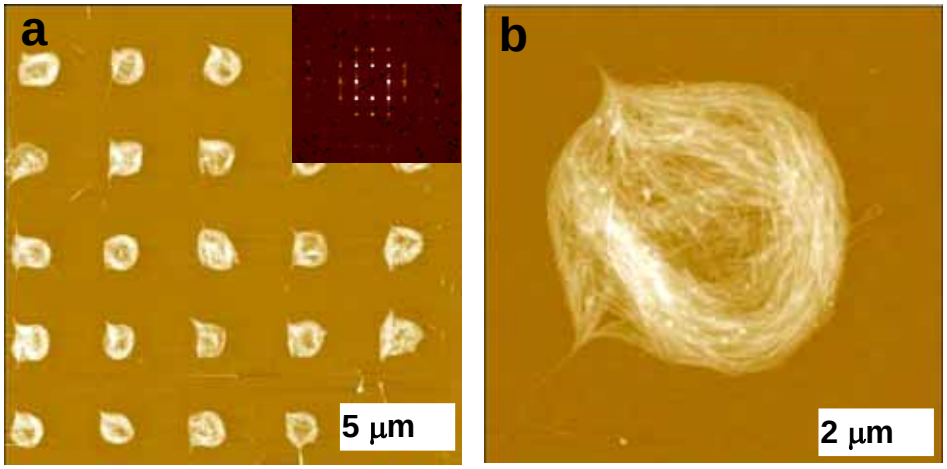

Figure 3.7. AFM topographical images of nest-shaped CNT assembly on amine-terminated areas obtained by casting CNT solution on rectangular- patterned substrates. The inset in (a) shows 2-D Fourier-transform demonstrating perfect positional ordering. Z-range is 100 nm for all images.

As can be seen in Figure 3.7, nest-shaped CNT assembly was selectively adsorbed on hydrophilic amine-terminated regions by casting CNT solution on patterned substrate. The patterned substrate is square-shape which is obtained by crossed microcontact

printing with stamp with parallel stripes of 10 μm pitch. From the Figure 3.7, even though the amine-terminated regions are rectangular shape, the shape of the adsorbed assembly of carbon nanotubes was observed to be circular shape, indicating that CNTs are likely to follow the motion of microfluidic flow and bend easily by the surface tension force. This feature also tells us the high elasticity of SWNTs. High-resolution AFM topographical images in Figure 3.7b show that nanotubes on the rim are bent along the circumference of the CNT nest, while nanotubes on the center region are in straight shape. From the overall tendencies of orientation and nanotube shapes, it is likely that the nanotubes are deposited along the contact line of evaporating CNT solution on the hydrophilic area.

3.3.4. Raman Spectroscopy Study of CNT Arrays

Figure 3.8a shows an AFM image of highly-packed CNT assembly on amine-terminated (NH_2–) monolayer obtained by casting CNT solution on patterned substrate. A Raman spectrum taken on this sample at a 532 nm laser excitation is shown in Figure 3.8c. We see typical Raman features of carbon nanotubes with RBM near ~180 cm^{-1}, D-band near 1340 cm^{-1}, G-band near 1590 cm^{-1}, and G′-band near 2670 cm^{-1}. The feature near 1740 cm^{-1} is the second-order Raman spectrum. A 3-D confocal Raman image of this CNT assembly was shown in Figure 3.8b which was obtained by integrating the intensity of Raman spectra at 1590 cm^{-1}. Similar to AFM image in Figure 3.8a, Raman image in Figure 3.8b clearly identify the highly packed CNT assembly on patterned surfaces. Locally high Raman intensity regions (bright color) along the stripes are possibly from the non-uniform thickness of CNT assembly.

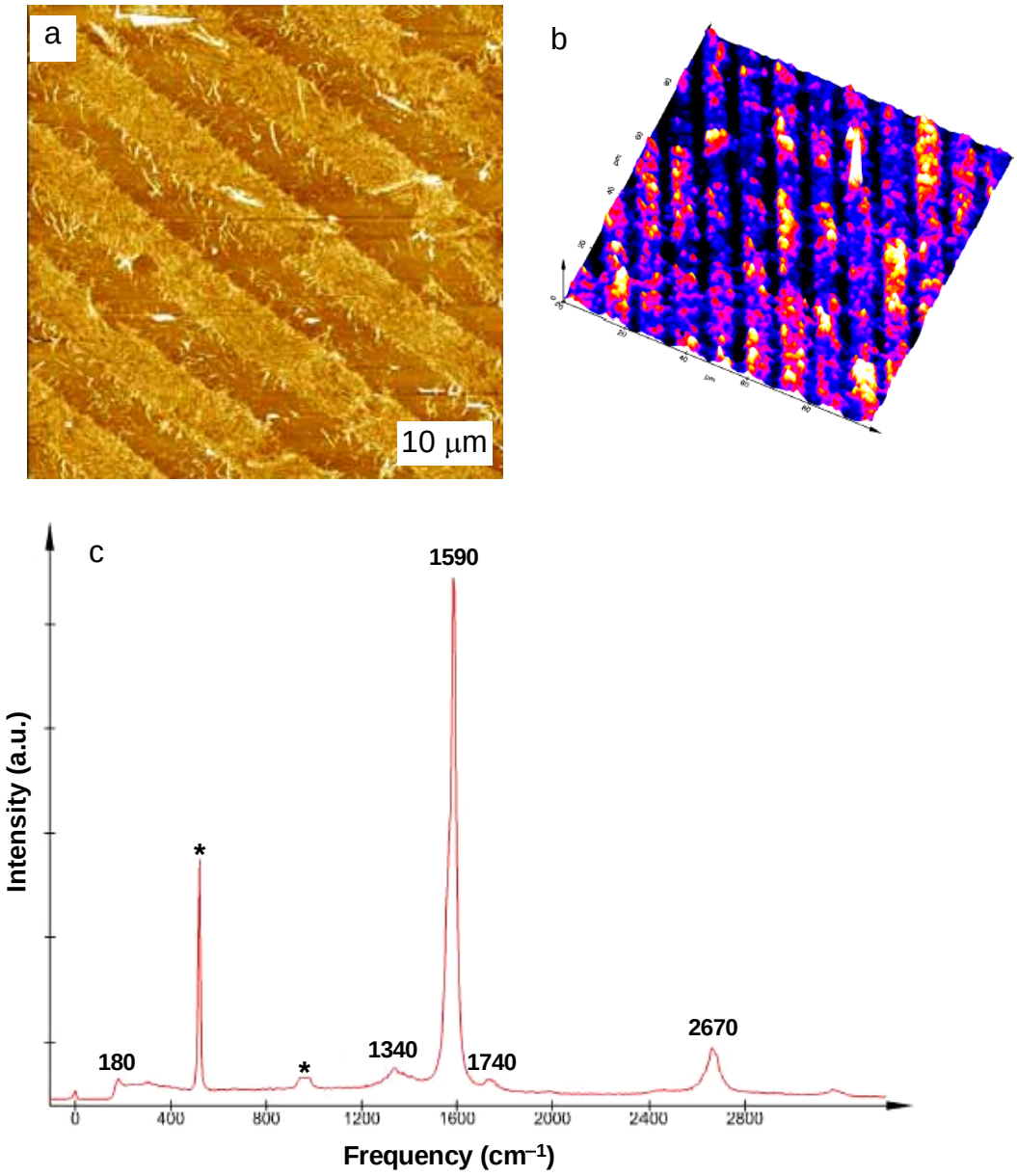

Figure 3.8. (a) AFM topographical image of densely packed arrays of carbon nanotubes on NH_2-terminated monolayer obtained by casting of CNT solution on patterned substrates. Z-range is 80 nm. (b) Confocal Raman scattering image of patterned assembly of carbon nanotubes of intensity at the Raman line 1590 cm^{-1}. c) Raman spectrum of CNT assembly taken with 532 nm laser excitation. The spectra marked with an asterisk (*) are from the silicon substrate.

CNT nest obtained by casting on rectangular-patterned substrate is shown in Figure 3.9a. A confocal Raman image of this nanotube "nest" is shown in Figure 3.9b, which represents the peak position of Raman line from 1588 cm^{-1} (dark color) to 1594

cm^{-1} (bright color). In accordance with the Raman peak position, Raman image exhibits dark color along the rim and bright color on the center region of the CNT nest. That is, Raman frequency is close to 1588 cm^{-1} along the rim and 1594 cm^{-1} on the center of the nest. Figure 3.9c shows the corresponding Raman spectra of these two areas, in which the blue spectrum (blue area in Figure 3.9b) is shifted 3 cm^{-1} to lower wavenumbers, while the width of the line is nearly constant. These changes in the Raman spectra clearly indicate that there is a change in nanotube structure along the tube axis. Changes in nanotube structure can have several origins such as external stress, due to catalyst particles, or local defects in the nanotube structure.

AFM images in Figure 3.9a show that nanotubes on the rim are bent along the circumference of the CNT nest, while nanotubes on the center region are in straight shape. Because of the nanotube bending and possibly shear stresses between neighboring CNT bundles, the bent nanotubes on the rim are likely to be under high tensile strain, which can cause some structural changes in nanotube. It has been known that the Raman G-band at ~1590 cm^{-1} varies with the C–C bond length of carbon nanotube.[44,45] For carbon nanotubes under hydrostatic pressure, compressive strain results in hardening of C–C bond length of carbon nanotubes.[46] In our experiments, the tensile strain of bent nanotubes may loosen the C–C bond length and consequently lower the frequency of G-band at ~1590 cm^{-1}. Previously, downward shift of D* band at around 2610 cm^{-1} was reported for SWNTs within a polymer under tensile strain.[47]

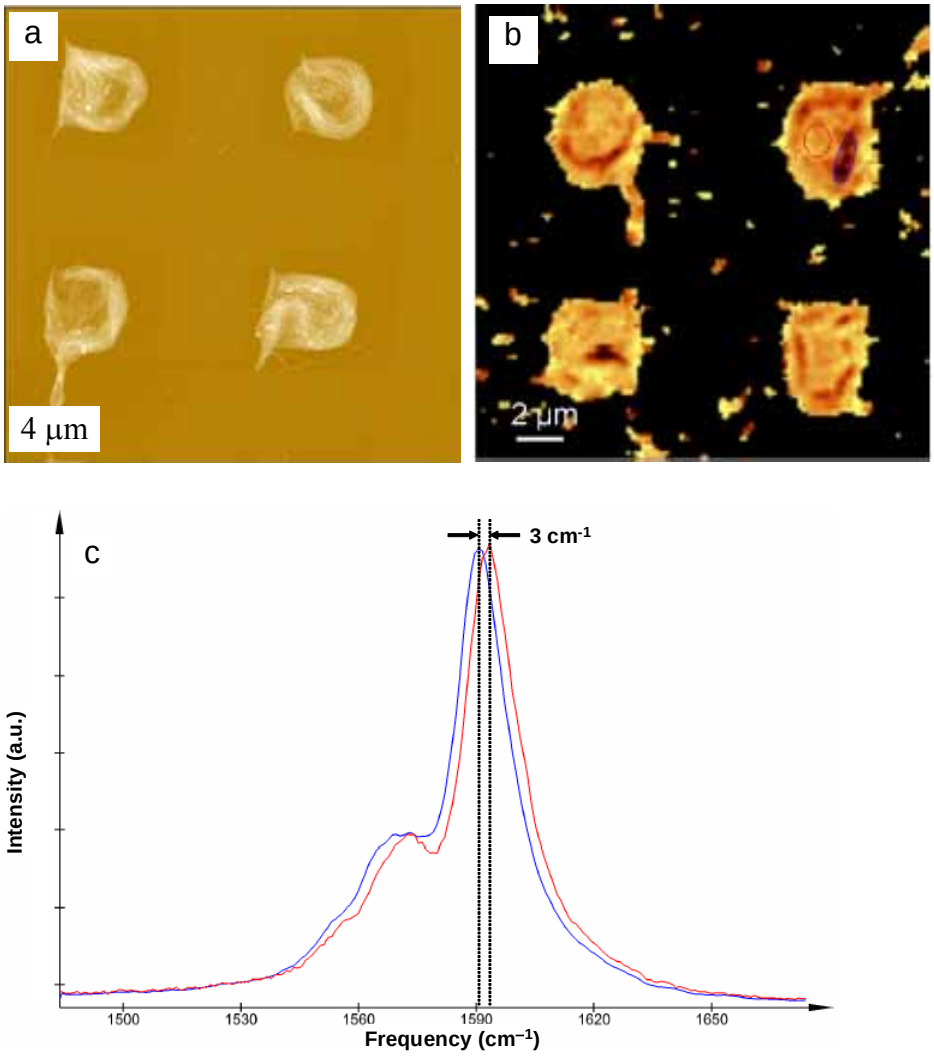

Figure 3.9. a) AFM topographical image of nest-shaped CNT assembly on amine-terminated rectangular pattern. b) Confocal Raman image of CNT "nest" at Raman line ~1590 cm^{-1}. The image is scaled from 1588 cm^{-1} (dark) to 1594 cm^{-1} (bright). c) Raman spectra obtained by integrating over all spectra in the marked areas. The red and blue spectra correspond to red and blue areas in Figure 3.9b, respectively. The spectra are scaled so that the intensity of the Raman line at 1590 cm^{-1} is identical in both spectra.

3.4. References

[1] Baughman, R. H.; Zakhidov, A. A.; de Heer, W. A. *Science* **2002**, *297*, 787.

[2] Tans, S. J.; Verschueren, A. R. M.; Dekker, C. *Nature* **1998**, *393*, 49.

[3] Rinzler, A.; Hafner, J. H.; Nikolaev, P.; Lou, L.; Kim, S. G.; Tomanek, D.; Nordlander, P. Colbert, D. T.; Smalley, R. E. *Science* **1995**, *269*, 1550.

[4] Dai, H.; Hafner, J. H.; Rinzler, A. G.; Colbert, D. T.; Smalley, R. E. *Nature* **1996**, *384*, 147.

[5] Wong, S. S.; Joselevich, E.; Woolley, A. T.; Cheung, C. L.; Lieber, C. M.; *Nature* **1998**, *394*, 52.

[6] Kong, J.; Franklin, M. R.; Zhou, C.; Chapline, M. G.; Peng, S.; Cho, K.; Dai, H. *Science* **2000**, *287*, 622.

[7] Collins, P. G.; Bradley, K.; Ishigami, M.; Zettl, A. *Science* **2000**, *287*, 1801.

[8] Tombler, T. W.; Zhou, C.; Alexseyev, L.; Kong, J.; Dai, H.; Liu, L.; Jayanthi, C. S.; Tang, M.; Wu, S. Y. *Nature* **2000**, *405*, 769.

[9] Vajtai, R.; Wei, B. Q.; Zhang, Z. J.; Jung, Y.; Ramanath, G.; Ajayan, P. M. *Smart Materials and Structures* **2002**, *11***,** 691.

[10] Zhang, X.; Cao, A.; Li, Y.; Xu, C.; Liang, J.; Wu D.; Wei, B. *Chem. Phys. Lett.* **2002**, *351*, 183.

[11] Cao, A.; Wei, B.; Jung, Y.; Vajtai, R.; Ajayan, P. M.; Ramanath, G. *App. Phys. Lett.* **2002**, *81*, 1297.

[12] Huang, S.; Mau, A. W. H.; Turney, T. W.; White, P. A.; Dai, L. *J. Phys. Chem. B* **2000**, *104*, 2193.

[13] Li, J.; Papadopoulos, C.; Xu, J. M.; Moskovits, M. *Appl. Phys. Lett.* **1999**, *75*, 367.

[14] Cai, L.; Bahr, J. L.; Yao, Y.; Tour, J. M. *Chem. Mater.* **2002**, *14*, 4235.

[15] Kong, J.; Zhou, C.; Morpurgo, A.; Soh, H. T.; Quate, C. F.; Marcus, C.; Dai, H. *Appl. Phys. A: Mater. Sci. Process* **1999**, *69*, 305.

[16] Huang, S.; Cai, X.; Liu, J. *J. Am. Chem. Soc.* **2003**, *125*, 5636.

[17] Krupke, R.; Hennrich, F.; Weber, H. B.; Beckmann, D.; Hampe, O.; Malik, S.; Kappes, M. M.; Lohneysen, H. V. *Appl. Phys. A* **2003**, *76*, 397.

[18] Ural, A.; Li, Y.; Dai H. *Appl. Phys. Lett.* **2002**, *81*, 3464.

[19] Fischer, J. E.; Zhou, W.; Vavro, J.; Llaguno, M. C.; Guthy, C.; Haggenmueller, R.; Casavant, M. J.; Walters, D. E.; Smalley, R. E. *J. Appl. Phys.* **2003**, *93*, 2157.

[20] Liu J.; Casavant, M. J.; Cox, M.; Walters, D. A.; Boul, P.; Lu, W.; Rimberg, A. J.; Smith, K. A.; Colbert D. T.; Smalley, R. E. *Chem. Phys. Lett.* **1999**, *303*, 125.

[21] Shimoda, H.; Oh, S. J.; Geng, H. Z.; Walker, R. J.; Zhang, X. B.; McNeil, L. E.; Zhou, O. *Adv. Mater.* **2002**, *14*, 899.

[22] Oh, S. J.; Cheng, Y.; Zhang, J.; Shimoda, H.; Zhou, O. *Appl. Phys. Lett.* **2003**, *82*, 2521.

[23] Burghard, M.; Duesberg, G.; Philipp, G.; Muster, J.; Roth, S. *Adv. Mater.* **1998**, *10*, 584.

[24] Gerdes, S.; Ondarcuhu, T.; Cholet, S.; Joachim, C. *Europhys. Lett.* **1999**, *48*, 292.

[25] Clauss, W.; Bergeron, D. J.; Johnson, A. T. *Phys. Rev. B* **1998**, *58*, R4266.

[26] Hertel, T.; Walkup, R. E.; Avouris, P. *Phys. Rev. B* **1998**, *58*, 13870.

[27] Salvetat, J.-P.; Briggs, G. A. D.; Bonard, J.-M.; Bacsa, R. R.; Kulik, A. J.; Stockli, T.; Burnham, N. A.; Forro, L. *Phys. Rev. Lett.* **1999**, *82*, 944.

[28] Minot, E. D.; Yaish, Y.; Sazonova, V.; Park, J.-Y.; Brink, M.; McEuen, P. L. *Phys. Rev. Lett.* **2003**, *90*, 156401.

[29] Maiti, A. *Nat. Mater.* **2003**, *2*, 440.

[30] Mews, A.; Koberling, F.; Basché, T.; Philipp, G.; Duesberg, G. S.; Roth, S.; Burghard, M. *Adv. Mater.* **2000**, *12*, 1210.

[31] Hartschuh, A.; Sanchez, E. J.; Xie, X. S.; Novotny, L. *Phys. Rev. Lett.* **2003**, *90*, 095503.

[32] Jiang, C.; Zhao, J.; Therese, H. A.; Friedrich, M.; Mews, A. *J. Phys. Chem. B.* **2003**, *107*, 8742.

[33] Dresselhaus, M. S.; Eklund, P. C. *Adv. Phys.* **2000**, *49*, 705.

[34] Hadjiev, V. G.; Iliev, M. N.; Arepalli, S.; Nikolaev, P.; Files, B. S. *Appl. Phys. Lett.* **2001**, *78*, 3193.

[35] Venkateswaram, U. D. *Phys. Rev. B* **1999**, *59*, 10928.

[36] Sandler, J.; Shaffer, M. S. P.; Windle, A. H.; Halsall, M. P.; Montes-Moran, M. A.; Cooper, C. A.; Young, R. J. *Phys. Rev. B.* **2003**, *67*, 035417.

[37] Tsukruk, V. V. *Adv. Mater.* **2001**, *13*, 95.

[38] Tsukruk, V. V.; Bliznyuk, V. N. *Langmuir* **1998**, *14*, 446

[39] Tsukruk, V. V.; Everson, M. P.; Lander, L. M.; Brittain, W. J. *Langmuir* **1996**, *12*, 3905.

[40] Darhuber, A. A.; Troian, S. M.; Davis, J. M.; Miller, S. M.; Wagner, S. *J. Appl. Phys.* **2000**, *88*, 5119.

[41] Nikoobakht, B.; Wang, Z. L.; El-Sayed, M. A. *J. Phys. Chem. B* **2000**, *104*, 8635.

[42] Shimoda, H.; Oh, S. J.; Geng, H. Z.; Walker, R. J.; Zhang, X. B.; McNeil, L. E.; Zhou, O. *Adv. Mater.* **2002**, *14*, 899.

[43] Petit, C. A. P.; Carbeck, J. D. *Nano Lett.* **2003**, *3*, 1141.

[44] Hadjiev, V. G.; Iliev, M. N.; Arepalli, S.; Nikolaev, P.; Files, B. S. *Appl. Phys. Lett.* **2001**, *78*, 3193.

[45] Gupta, S.; Hughes, M.; Windle, A. H.; Robertson, J. *J. Appl. Phys.* **2004**, *95*, 2038.

[46] Sandler, J.; Shaffer, M. S. P.; Windle, A. H.; Halsall, M. P.; Montes-Moran, M. A.; Cooper, C. A.; Young, R. J. *Phys. Rev. B.* **2003**, *67*, 035417.

[47] Frogley, M. D.; Zhao, Q.; Wagner, H. D. *Phys. Rev. B* **2002**, *65*, 113413.

Chapter 4. Liquid-crystalline processing of highly-oriented carbon nanotube arrays for thin film transistors

4.1. Introduction

Electronic devices based on solution-processable one-dimensional semiconducting materials and their arrays are generating significant research interest for the applications requiring low-cost fabrication, large-area coverage, and low-temperature processing on flexible substrates.[1,2,3] Semiconducting single wall carbon nanotubes (SWNTs) are one of the promising candidates for high-performance thin-film transistors (TFTs) due to their potential high carrier mobilities and large current carrying capacities.[4,5] However, because of the limited current-carrying capacity of individual SWNTs, random networks or parallel arrays of SWNTs would be required to provide the necessary current density of devices. The performance of carbon nanotube (CNT) TFTs can be improved by increasing surface density and controlling the uniform alignment of CNTs. Several approaches have been made to align CNTs by solution-based techniques,[6,7,8,9,10,11,12] but most of the methods are limited in their prospective applications due to low surface density of CNT array formed. Other solution-based approaches have been attempted to make highly dense CNTs, but the resulting CNT layer is randomly oriented.[13]

Highly dense, randomly oriented CNTs have been recently used as effective semiconducting layers for thin-film transistors, although the inter-nanotube contact resistance of many overlapping tubes limited the full exploitation of the intrinsic high

mobilities.[14,15,16,17,18] Recently, it has been demonstrated that carbon nanotubes, like other anisotropic and one-dimensional molecules, might form a lyotropic liquid crystalline phase.[19,20,21,22] Above a critical concentration, CNTs have shown a phase transition to nematic liquid crystal phase. This liquid crystalline behavior of CNT solution can offer novel solution-processable routes to large-scale alignment of CNTs in many potential applications requiring oriented CNT arrays.[23] However, inducing long-range nematic ordering with low misaligned defects within CNT surface layer still remains a big challenge.

Herein, we report the formation of long-range ordered and dense array of CNTs via liquid crystalline processing by simple tilted-drop casting of CNT solution on functionalized micropatterned geometries. As the solvent evaporates during tilted-drop casting, the carbon nanotubes diffuse from the bulk solution to the liquid-solid-air receding contact line by convective flow causing the concentrated solution to form nematic liquid crystalline phase. Confined geometry of the micropatterned surface induces uniform long-range orientation of dense CNTs films during the surface deposition. We further demonstrate that the electrical performance of thin-film transistors based on these densely-packed uniformly oriented CNT array is dramatically improved compared to random CNTs.

4.2. Sample preparations

Purification of single-wall carbon nanotubes synthesized by arc-discharge (Carbon Solutions, Inc) was performed by mild air oxidation (350 ^{o}C, 2hr), followed by a

6 M hydrochloric acid washing for 2 hr. Stable dispersion of CNTs was achieved by dissolving purified CNTs in 1% aqueous sodium dodecyl sulafate (SDS) solution by sonication for 2hr and centrifugation (18000 rpm, 1hr). The resulting SWNT bundles were 1.6±0.6 μm in length and 6.7±3.0 nm in diameter, as measured from atomic force microscope (AFM).[24] The concentration of resulting CNT solution was ~0.1 – 0.2 mg/ml. All the silicon substrate was modified with aminopropyltriethoxysilane to form NH_2-terminated surface. The CNT solution was tilted-drop cast on photolithographically patterned surfaces tilted about 5^o for unidirectional solvent evaporation. The tilted-drop casting process was conducted in a sealed container (within 2 days) for SWNT films in Figure 4.1 or in ambient laboratory conditions (within 18 hrs) without using any sealed container for other SWNT films. For CNT-TFT fabrication, a heavily doped silicon wafer was used as the substrate and the gate electrode. CNT films were fabricated on SiO_2 (200 nm)/Si substrate and subsequently Au electrodes were prepared with e-beam lithography followed by lift-off of photoresist (AZ 5214). The semiconducting properties of CNT-TFTs were measured by HP 4155 semiconductor parameter analyzer for 5–7 devices with variable channel lengths and presented as average values.

4.3. Results and Discussion

Figure 4.1a shows schematic of tilted-drop casting process of SWNT solution on a silicon wafer modified with NH_2-terminated self-assembled monolayer (SAM) according to the procedure described in detail elsewhere.[24,25] For this process, an appropriate amount of SWNT solution was spread on the tilted substrate and left without any perturbation inside a sealed container. As the solvent evaporated, the liquid-solid-air contact line sweeps

down the surface, accumulating highly concentrated solution in the vicinity and leaving dense CNT layer behind the receding line. Figure 4.1b shows AFM image of the resulting SWNT film formed after tilted-drop casting was completed. It shows a large area of dense SWNT film, in which SWNT bundles form monolayer surface film with the thickness 7 nm close to the diameter of the bundles with occasional defects and multilayer aggregates (indicated by arrows).

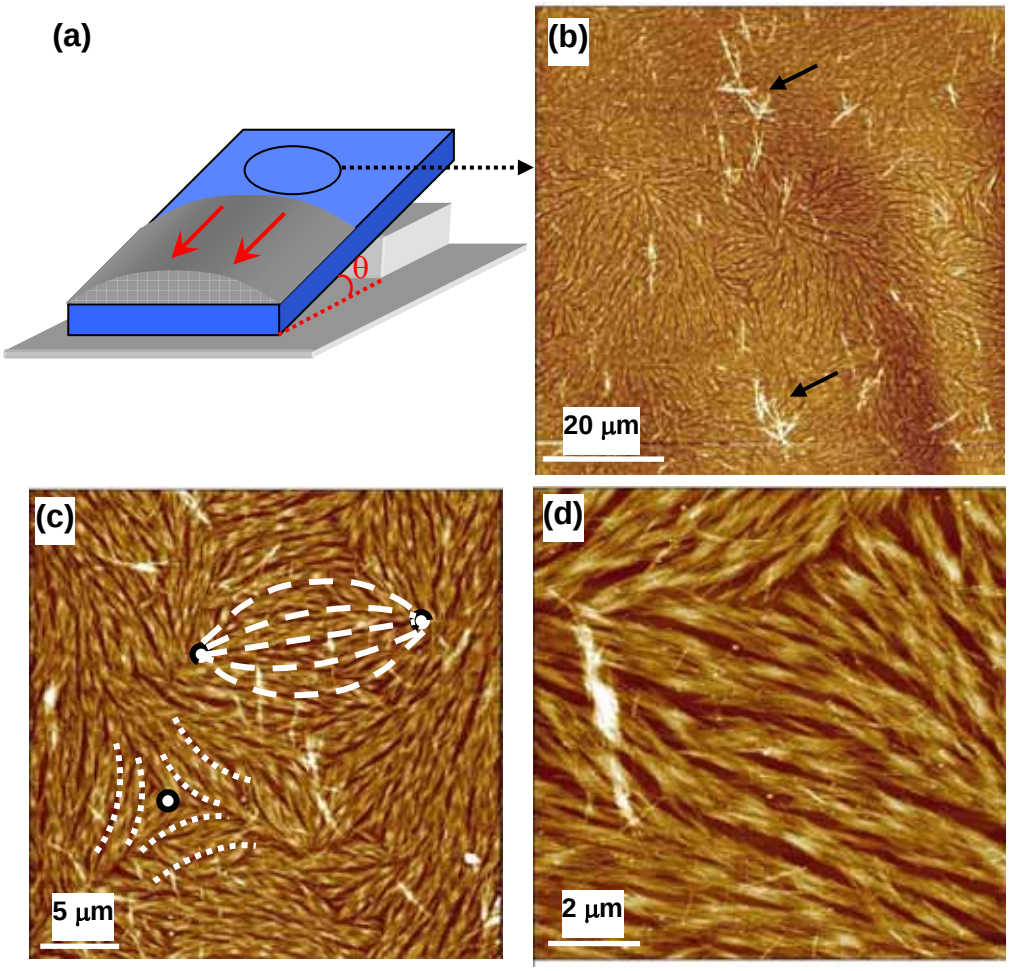

Figure 4.1. Surface ordering of carbon nanotube films by slow evaporation of carbon nanotube solution during tilted-drop casting on NH_2-terminated SAM surface of a silicon wafer. a) Scheme for the tilted-drop fabrication routine without physical confinement. b)-d) AFM topographical images of a CNT surface film at different magnifications showing liquid crystalline texture and ordering along with characteristic topological defects.

A higher resolution imaging revealed that SWNTs are assembled into small bundle-like structures and within each domain SWNTs are uniformly aligned (Figures 4.1c,d). This microstructure is similar to nematic-type ordering observed for liquid-crystalline CNT solutions and their footprints on a solid substrate.[21,26,27] While previous studies are based on highly concentrated CNT solutions, our observed liquid-crystalline like surface structures are achieved from low-concentration (~0.1–0.2 mg/ml) aqueous solution but involves ordering along the receding contact line. We suggest that the formation of liquid-crystalline structure is caused the high evaporation rate on the contact line resulting in highly concentrated solution in the vicinity of the receding contact line thus, promoting the liquid crystalline ordering. This phenomenon is well-known in colloid systems[28,29] and similar behavior has been previously observed for SWNT[30,31] and nanorod solutions.[32,33]

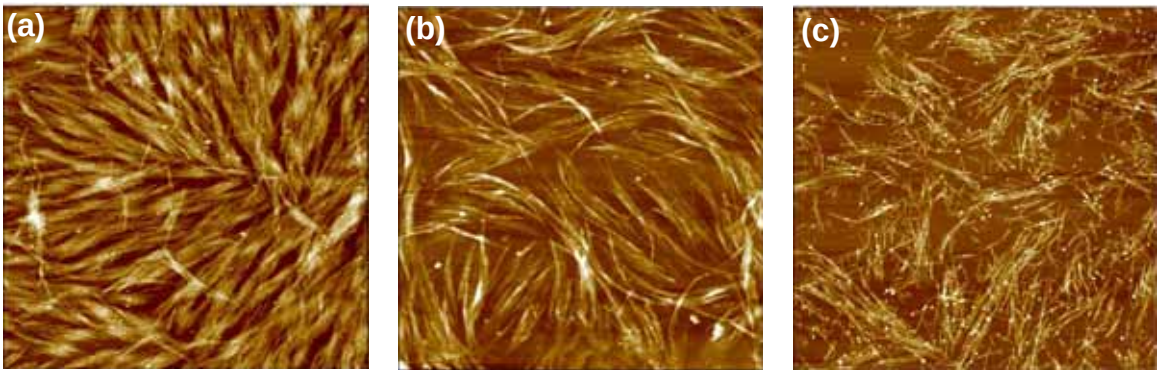

Figure 4.2. Different structures of CNT films when the solutions are evaporated within (a) 2 days, (b) 18 hrs, and (c) 4 hrs.

The surface textures and defects for our SWNTs closely remind those observed for liquid-crystalline CNTs.[20,31] The typical singularity defects of liquid crystalline types related to disclinations with a singular center and with two centers are presented in Figure

4.1c. It is worth to note that by changing the solvent evaporation rate, the structure of SWNT film can be controlled: with increasing the evaporation rate, the size of nematic-type domain decreased resulting in isotropic texture when the evaporation completed within several hours (Figure 4.2). Consequently, the higher nematic ordering is achieved by slowing down the solvent evaporation rate. Finally, surface cracks and undulations observed for these CNT films occur due to internal stresses from the coupling between the nematic ordering and elasticity in the formation process.

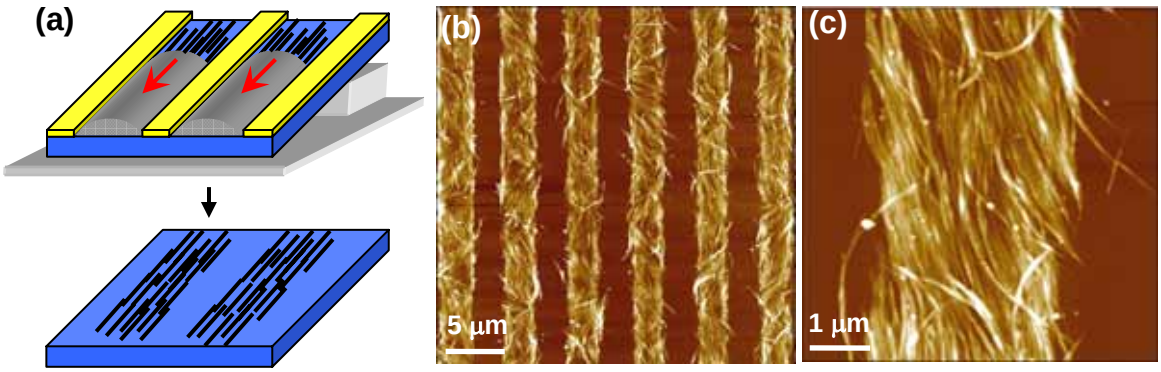

Figure 4.3. a) Schemes for the tilted-drop fabrication of thin film on amine-terminated SAM surface micropatterned with photoresist polymer stripes. b),c) AFM topographical images of carbon nanotube films showing uniaxially oriented, densely-packed CNT bundles.

The array of long-range nematic structures can be created by confining the drying process within micropatterned geometries (Figure 4.3). To control this process, we formed stripes of photoresist on top of amine-terminated SAM by using photolithography with the periodicity 5 μm. In this case the tilted-drop casting process splits in parallel microchannels with the solution confined between two parallel solid walls (height is 1.3 μm) (Figure 4.3a). This modification results in unidirectional microfluidic flow pattern

which causes the formation of multiple stripes of highly oriented SWNT films. Removing the photoresist micropattern leads to the densely-packed oriented SWNT stripes with 2.5 μm width and 5 μm periodicity (Figures 4.3b,c). Within these stripes, SWNTs form undulated structures with the director of the local orientation regularly modulating along the axis due to capillary instabilities in the receding front.[34] It is worth to note that when the width of confining channel increased and became much higher than the average nanotube length (1.6 μm), the nematic-like ordering vanished. This behavior indicates importance of the steric factors in the formation of highly oriented structures.

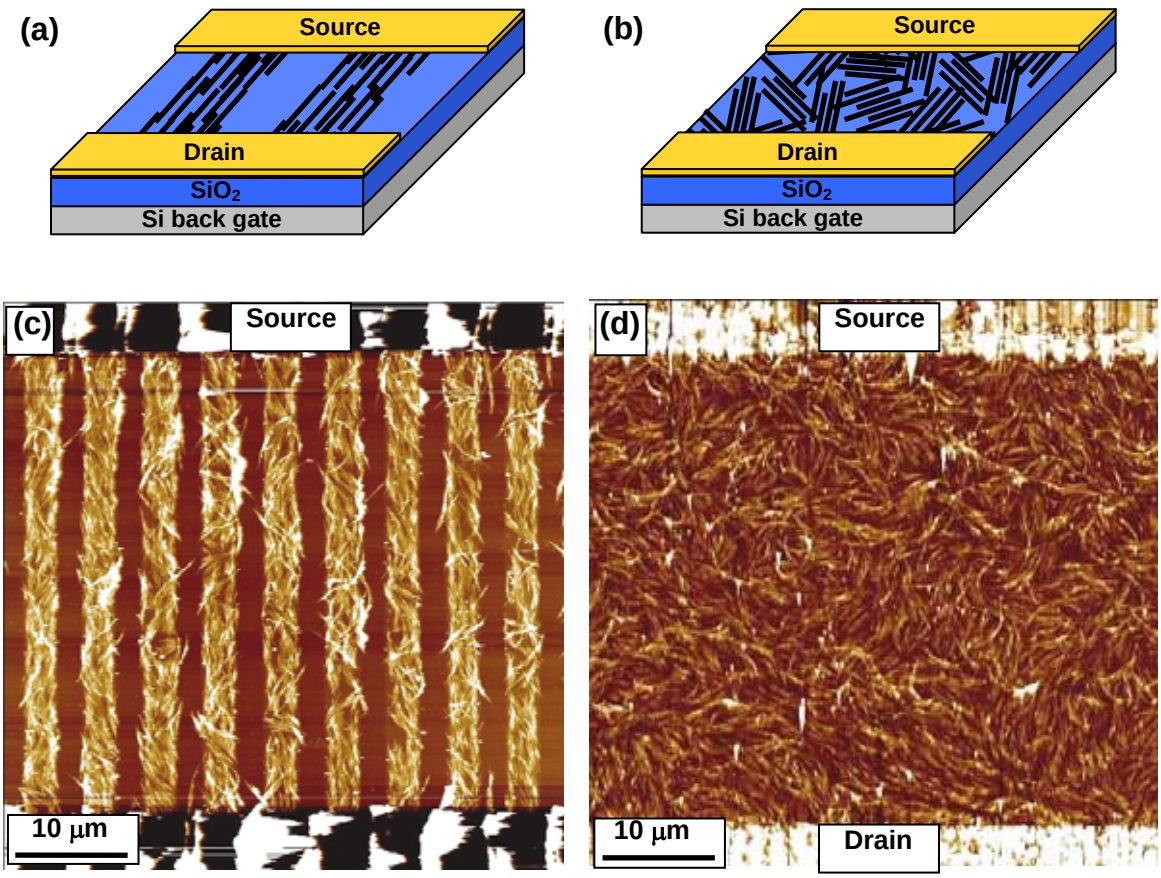

Figure 4.4. Device configurations of back-gated oriented (a) and random CNT-TFTs (b) with Au source/drain electrodes. c) AFM topographical image of CNT-TFT with uniaxially ordered micropatterned CNT array. d) AFM topographical image of CNT-TFT with randomly oriented CNT surface film.

These dense and highly oriented SWNT films can be exploited as component in high performance electronic devices. Without going into detailed study of the device performance but just to test their potential, we fabricated CNT thin film transistors (TFTs) in which densely packed CNT layer serves as semiconducting channels between source and drain electrodes (Figures 4.4a,b). For device fabrication, source-drain contact electrodes were made with Au (50 nm high) layer by using e-beam evaporation and subsequent lift-off process. Here, we used only Au contact with minimal Schottky barrier to carbon nanotubes.[35] As known, Au electrodes are strongly attached to the silicon surface due to the affinity to amine-terminated SAM and the use of additional interlayer can be avoided making the fabrication process simpler without compromising on structure robustness.

To analyze the preliminary electrical properties and device performances, we fabricated oriented and random CNT films which were formed with and without micropatterning, respectively (Figures 4.4c,d). CNT surface layers with confined geometries show strong preferential orientation with some modulation along the stripes due to flow instabilities while random texture was observed in traditional CNT film (Figures 4.4c,d). The nanotube density in both cases was about 18 bundles/μm that corresponds to surface density of 7 bundles/μm^2 with taking into account of the average bundle length (1.6 μm).

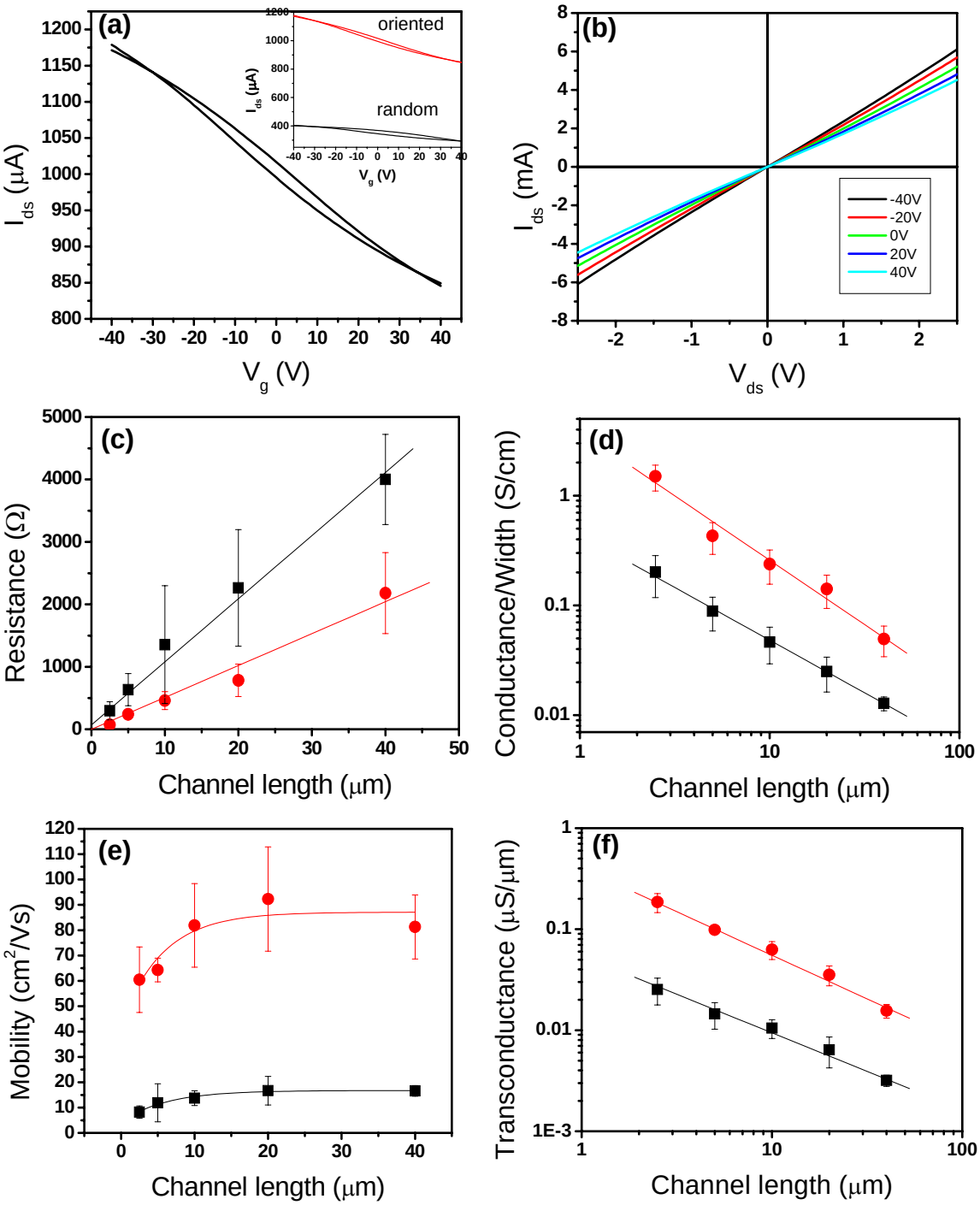

Figure 4.5. a) Transfer characteristics of oriented CNT-TFTs with 20 μm channel length. The bias voltage Vds is 0.5 V. The inset compares the transfer characteristics between oriented and random SWNTs. b) Output characteristics of oriented CNT-TFTs when the gate voltage is swept from –40 to 40 V in 20 V steps. c) – f) Electrical characteristics of oriented (circles) and random (squares) CNT-TFTs with different channel lengths: c) resistance measured at Vgs = –40V; d) normalized conductance measured at Vgs = –40V, channel width is 200 μm; e) career mobility; f) normalized transconductance.

The transfer and output characteristics of a CNT-TFT are shown in Fig 4.5a and b. The device exhibits p-type semiconducting behavior with a linear IV_{ds} characteristics and minor IV_g hysteresis, which is a typical behavior of SWNT transistors operated in air.37 The saturation regime was not reached under experimental conditions available. Also, the device shows a modest dependence on gate voltage due to the presence of CNT bundles containing metallic nanotubes. The transistor with random SWNTs shows similar p-type semiconducting behavior, but the current level is much lower than that of oriented SWNTs (see inset in Fig 4.5a). The electrical characteristics are compared in Figure 4.5c–f for CNT-TFTs with different channel length (different distance between electrodes). Considering that the effective channel width contributing to the observed transport properties is half of the full channel width (200 μm) for micropatterned array, we normalized device performances (conductance, mobility, and transconductance) correspondingly. As can be seen in Figure 4c, resistance of the oriented CNT-TFT is much lower (3–5 times) than that with random CNT surface layer. Moreover, the contact resistances of the gold/nanotube interface, as determined by the y-intercept of the linear fit, are negligible compared to the channel resistances, indicating an excellent property achieved by avoiding the use of adhesive metal interlayers.

Correspondingly, the normalized conductance of oriented CNT-TFTs is 4 – 7 times higher than those with random CNTs (Figure 4.5d). All CNT-TFTs show similar linear dependence of conductance upon channel length with the conductance exponent of –1.17 for oriented and –0.96 for random CNT-TFTs. The value of –0.96 for random SWNT film agrees very well with the experimental and theoretical studies based on

random network of SWNT films.[14,36] As known, the conductance exponent approaches −1.0 for high density (>3.0 μm^2) SWNT films and decreases with decreasing nanotube density.[36] Oriented CNT-TFTs possess similar conductance exponent with some higher-off deviation on channel 2.5 μm, which is possibly caused by the occasional ballistic transport through highly oriented longer nanotubes (over 2–3 μm) for short channel length (2.5 μm). As known, the ballistic transport for short channel length can make the transport scaling more rapidly with channel length.[14,36]

The linear hole mobility estimated from the relation $\mu = (dI_D/dV_G)(L/WCV_D)$, where I_D is the drain current, V_G is the gate voltage, L is the channel length, W is the channel width, C is the gate capacitance, and V_D is the drain voltage is presented in Figure 4.5e. The gate capacitance can be estimated from the relation $C = \varepsilon\varepsilon_0/t$, where ε is the dielectric constant of the silicon oxide (3.9), ε_0 is the vacuum permittivity, and t is the thickness of the gate dielectric (silicon oxide). The hole mobility increases with the channel length in the short channel range until saturation for the long channels. The hole mobility of oriented CNT-TFT is in the range of 60 – 92 cm^2/Vs which is much larger (5–6 times) than those of random CNT-TFTs. Both values are significantly larger than those of amorphous Si TFTs (<1 cm^2/Vs).[37] We suggest that the uniaxially oriented SWNTs significantly reduce the number of inter-tube contacts that the carriers should pass through, resulting in dramatically increased mobility. The highest mobility of 126 cm^2/Vs achieved for some oriented CNT-TFTs (for channel length of 20 μm) is comparable to the record mobility reported for the highly oriented SWNT TFTs (125

cm^2/Vs) prepared by CVD method.[38] On the other hand, this mobility is higher than that for the TFTs with parallel arrays of silicon nanowires (119 cm^2/Vs).[39]

Finally, normalized device transconductance ($g_m=(dI_D/dV_G)/W$) scales linearly with channel length for both TFTs (Figure 4.5f). The transconductance is within 0.02 – 0.2 μS/μm (at V_D=0.1V) for oriented CNT-TFTs, which is seven times higher than that for random CNT-TFTs (0.003–0.03 μS/μm). The transconductance value (0.02–0.2 μS/μm) for oriented CNT-TFTs is higher/comparable to that of oriented Si nanowires TFTs (0.09 μS/μm). These and other electrical characteristics of oriented CNT-TFTs quoted above are much higher than those for random CNT-TFTs. Moreover, they are very high as compared to usual literature values for CNT-TFTs and sometimes are close to record values reported for rather complicated TFT versions.

Although our CNT-TFTs show excellent electrical characteristics even without special optimization their relatively low on/off ratios (<3) is caused by the presence of metallic SWNTs in the semiconducting channels because of mixed character of CNT used here. However, the high device mobility and transconductance values demonstrate the potential application of high-density oriented SWNT films in low-cost, large-scale high-performance electronic devices.[1,40] Prospective realization of high performance CNT-TFTs will rely on the electronic purity of SWNTs which should be addressed in future studies. These issues are currently tackled by several research groups working towards effective separation of metallic and semiconducting nanotubes.[41,42] We believe that if highly purified carbon nanotubes will be exploited, the tilted-drop approach

suggested here will be instrumental in a simple fabrication of highly efficient thin film transistors and other electronic microdevices with breakthrough electronic characteristics.

4.4. References

[1] Forrest, S. R. *Nature* **2004**, *428*, 911.

[2] Mitzi, D. B. *J. Mater. Chem.* **2004**, *14*, 2355.

[3] Whang, D.; Jin, S.; Wu, Y.; Lieber, C.M. *Nano Lett.*, **2003**, *3*, 1255.

[4] Durkop, T.; Getty, S. A.; Cobas, E.; Fuhrer, M. S. *Nano Lett.* **2004**, *4*, 35.

[5] Yao, Z.; Kane, C. L.; Dekker, C. *Phys. Rev. Lett.* **2000**, *84*, 2941.

[6] Gao, J. B.; Yu, A. P.; Itkis, M. E.; Bekyarova, E.; Zhao, B.; Niyogi, S.; Haddon, R. C. *J. Am. Chem. Soc.* **2004**, *126*, 16698.

[7] McLean, R. S.; Huang, X. Y.; Khripin, C.; Jagota, A.; Zheng, M. *Nano Lett.* **2006**, *6*, 55.

[8] Wang, Y.; Maspoch, D.; Zou, S.; Schatz, G. C.; Smalley, R. E.; Mirkin, C. A. *Prod. Nat. Acad. Sci. U.S.A.* **2006**, *103*, 2026

[9] Lay, M. D.; Novak, J. P.; Snow, E. S. *Nano Lett.* **2004**, *4*, 603.

[10] Meitl, M. A.; Zhou, Y. X.; Gaur, A.; Jeon, S.; Usrey, M. L.; Strano, M. S.; Rogers, J. A. *Nano Lett.* **2004**, *4*, 1643.

[11] Shim, B. S.; Kotov, N. A. *Langmuir* **2005**, *21*, 9381.

[12] Xin, H. J.; Woolley, A. T. *Nano Lett.* **2004**, *4*, 1481.

[13] Park, J. U.; Meitl, M. A.; Hur, S. H.; Usrey, M. L.; Strano, M. S.; Kenis, P. J. A.; Rogers, J. A. *Angew. Chem. Int. Ed.* **2006**, *45*, 581.

[14] Snow, E. S.; Novak, J. P.; Campbell, P. M.; Park, D. *Appl. Phys. Lett.* **2003**, *82*, 2145.

[15] Bradley, K.; Gabriel, J. C. P.; Gruner, G. *Nano Lett.* **2003**, *3*, 1353.

[16] Seidel, R.; Graham, A. P.; Unger, E.; Duesberg, G. S.; Liebau, M.; Steinhoegl, W.; Kreupl, F.; Hoenlein, W. *Nano Lett.* **2004**, *4*, 831.

[17] Zhou, Y. X.; Gaur, A.; Hur, S. H.; Kocabas, C.; Meitl, M. A.; Shim, M.; Rogers, J. A. *Nano Lett.* **2004**, *4*, 2031.

[18] Ozel, T.; Gaur, A.; Rogers, J. A.; Shim, M. *Nano Lett.* **2005**, *5*, 905.

[19] Badaire, S.; Zakri, C.; Maugey, M.; Derre, A.; Barisci, J. N.; Wallace, G.; Poulin, P. *Adv. Mater.* **2005**, *17*, 1673.

[20] Islam, M. F.; Nobili, M.; Ye, F. F.; Lubensky, T. C.; Yodh, A. G. *Phys. Rev. Lett.* **2005**, *95*, 148301.

[21] Song, W. H.; Kinloch, I. A.; Windle, A. H. *Science* **2003**, *302*, 1363.

[22] DavisDavis, V. A.; Ericson, L. M.; Parra-Vasquez, A. N. G.; Fan, H.; Wang, Y. H.; Prieto, V.; Longoria, J. A.; Ramesh, S.; Saini, R. K.; Kittrell, C.; Billups, W. E.; Adams, W. W.; Hauge, R. H.; Smalley, R. E.; Pasquali, M. *Macromolecules* **2004**, *37*, 154.

[23] Ericson, L. M.; Fan, H.; Peng, H. Q.; Davis, V. A.; Zhou, W.; Sulpizio, J.; Wang, Y. H.; Booker, R.; Vavro, J.; Guthy, C.; Parra-Vasquez, A. N. G.; Kim, M. J.; Ramesh, S.; Saini, R. K.; Kittrell, C.; Lavin, G.; Schmidt, H.; Adams, W. W.; Billups, W. E.; Pasquali, M.; Hwang, W. F.; Hauge, R. H.; Fischer, J. E.; Smalley, R. E. *Science* **2004**, *305*, 1447.

[24] Ko, H.; Peleshanko, S.; Tsukruk, V. V. *J. Phys. Chem. B* **2004**, *108*, 4385.

[25] Tsukruk, V. V.; Ko, H.; Peleshanko, S. *Phys. Rev. Lett.* **2004**, *92*, 065502.

[26] Zhang, S.; Kinloch, I. A.; Windle, A. H. *Nano Lett.* **2006**, *6*, 568.

[27] Ramesh, S.; Ericson, L. M.; Davis, V. A.; Saini, R. K.; Kittrell, C.; Pasquali, M.; Billups, W. E.; Adams, W. W.; Hauge, R. H.; Smalley, R. E. *J. Phys. Chem. B* **2004**, *108*, 8794.

[28] Deegan, R. D.; Bakajin, O.; Dupont, T. F.; Huber, G.; Nagel, S. R.; Witten, T. A. *Nature* **1997**, *389*, 827.

[29] Kim, M. H.; Im, S. H.; Park, O. O. *Adv. Funct. Mater.* **2005**, *15*, 1329.

[30] Shimoda, H.; Oh, S. J.; Geng, H. Z.; Walker, R. J.; Zhang, X. B.; McNeil, L. E.; Zhou, O. *Adv. Mater.* **2002**, *14*, 899.

[31] Duggal, R.; Hussain, F.; Pasquali, M. *Adv. Mater.* **2006**, *18*, 29.

[32] Nikoobakht, B.; Wang, Z. L.; El-Sayed, M. A. *J. Phys. Chem. B* **2000**, *104*, 8635.

[33] Li, L. S.; Alivisatos, A. P. *Adv. Mater.* **2003**, *15*, 408.

[34] Reiter, G.; Sharma, A. *Phys. Rev. Lett.* **2001**, *87, 166103*

[35] Yaish, Y.; Park, J. Y.; Rosenblatt, S.; Sazonova, V.; Brink, M.; McEuen, P. L. *Phys. Rev. Lett.* **2004**, *92*, 046401.

[36] Kumar, S.; Murthy, J. Y.; Alam, M. A. *Phys. Rev. Lett.* **2005**, *95,* 066802

[37] Kagan, C. R.; Andry, P. *Thin-film Transistors*; Marcel Dekker: New York, 2003.

[38] Kocabas, C.; Hur, S. H.; Gaur, A.; Meitl, M. A.; Shim, M.; Rogers, J. A. *Small* **2005**, *1*, 1110.

[39] Duan, X. F.; Niu, C. M.; Sahi, V.; Chen, J.; Parce, J. W.; Empedocles, S.; Goldman, J. L. *Nature* **2003**, *425*, 274.

[40] Dimitrakopoulos, C. D.; Malenfant, P. R. L. *Adv. Mater.* **2002**, *14*, 99.

[41] Strano, M. S.; Dyke, C. A.; Usrey, M. L.; Barone, P. W.; Allen, M. J.; Shan, H. W.; Kittrell, C.; Hauge, R. H.; Tour, J. M.; Smalley, R. E. *Science* **2003**, *301*, 1519.

[42] Zheng, M.; Jagota, A.; Strano, M. S.; Santos, A. P.; Barone, P.; Chou, S. G.; Diner, B. A.; Dresselhaus, M. S.; McLean, R. S.; Onoa, G. B.; Samsonidze, G. G.; Semke, E. D.; Usrey, M.; Walls, D. J. *Science* **2003**, *302*, 1545.

Chapter 5. Strain Sensitive Carbon Nanotubes in Freely Suspended Nanomembranes

5.1. Introduction

Carbon nanotubes (CNTs) are considered as prospective elements for nanosensors due to their unique mechanical and electronic properties.[1] The strong dependence of their band electronic structures upon the external stress is promising for development of the nanoelectromechanical devices sensitive to pressure, fluid flow, and fracture.[2,3] Strain sensing was demonstrated by detecting the shift of Raman bands and changes in electronic properties of carbon nanotubes embedded in polymer matrix [4,5] or bent by the AFM tip.[2,6] The Raman spectroscopy is considered to be promising for highly sensitive detection if resonance Raman scattering (RRS) [7] or surface enhanced Raman scattering (SERS) [8] phenomena are in place. Due to the strong RRS phenomena in carbon nanotubes, Raman spectroscopy becomes a critical tool. [9,10,11] With the development of confocal Raman technique, it became possible to obtain Raman signal with a sub-micron spatial resolution [12, 13] and from individual carbon nanotubes and bundles.,[13]

Recently, flexible free-suspended nanomembranes with total thickness of several tens of a nanometer have been suggested as a novel platform for highly-sensitive microsensors.[14] These free suspended nanomembranes fabricated via layer-by-layer (LbL) assembly showed excellent robustness and sensitivity to external stimuli.[15,16] However, studies of micromechanical properties of these nanomembranes were limited to conventional testing routines which are not capable of providing structurally-sensitive

information for stressed nanomembranes [16,17] New approaches are required to monitor internal stresses and structural reorganizations of these nanoscale membranes in the course of their responsive behavior.

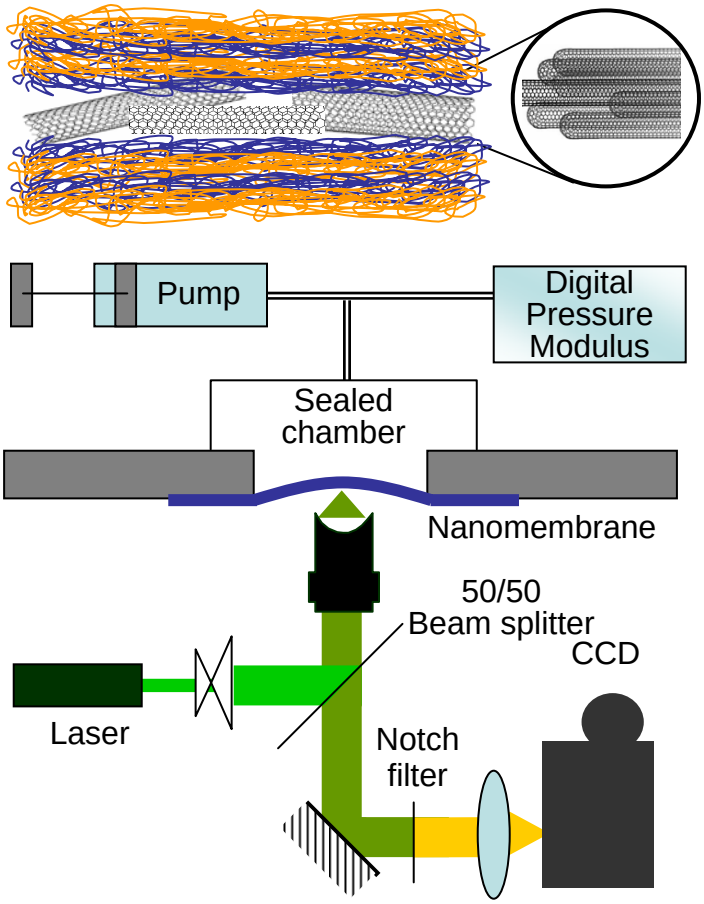

Figure 5.1. Schematic of 9CNT9 membrane, the carbon nanotubes are sandwiched between the polyelectrolyte multilayers (top); experimental schematic of combination of bulging test and confocal Raman spectroscopy (Bottom).

Here, we suggest a novel approach by applying confocal Raman spectroscopy in RRS modes for *in situ* monitoring of the deflecting freely suspended nanomembranes with embedded carbon nanotube array as a central nanolayer (Fig 5.1). This central layer provided not only for significant reinforcement of the nanomembranes essential for their

outstanding robustness but generated a strong resonance Raman scattering which can be used for the direct monitoring of internal membrane stresses with high precision, localization, and *in real-time*.

5.2. Sample Preparations

Single wall carbon nanotubes produced by arc discharge method (Carbolex, TX) were purified as described in Chapter 2 and used as bundles of 3-4 nm in diameter and 1-2 μm length. In this work, we would focus on the nanomembranes containing carbon nanotubes and nine bilayers, 9CNT9. Pure polymeric nanomembranes were also studied for comparative purpose. These nanomembranes have been free-suspended over the micromanufactured openings in copper substrates with lateral dimensions of 150 μm. The copper plates with nanomembranes were attached to a sealed chamber for a bulging test. The pressure inside the chamber was adjusted by the pressure pump and monitored by DPM-0.1 digital pressure module (SI Pressure Instruments Ltd, Birmingham, UK) with an accuracy of 0.02 mbar. The deflection of the membrane under variable pressure was measured by a home-built interferometry set-up.

Confocal Raman spectroscopy was conducted with a custom designed set-up based on Aurora-III NSOM microscope (Digital Instruments). A Nd:YAG laser (532 nm) was used as the light source with intensity of 1 mW on the sample. The spectra were recorded by a cooled CCD camera with resolution of 0.32 cm^{-1}. For the combination of the bulging test and confocal Raman measurements, the seal chamber was placed at the focus of the objective lens and data were collected in back scattering mode. During the

experiments, the nanomembrane was gradually deflected in a step-wise manner and Raman spectra were recorded *directly* during a reversible cycle of changing pressure.

5.3. Results and Discussion

The freely suspended nanomembranes fabricated with spin-assisted Layer-by-Layer assembly contain poly(allyl amine) / sulfonated polystyrene (PAH/PSS) with a general formula is $(PAH\text{-}PSS)_nPAH/CNT/(PAH\text{-}PSS)_nPAH$, or (nCNTn). The properties of 9CNT9 nanomembrane are summarized in Table 5.1. Carbon nanotubes randomly assembled within a central nanolayer covered 20 % of the surface of PAH topmost layer (Figure 5.2a). The overall volume fraction of carbon nanotube within the nanomembrane is estimated to be within 0.8 - 1.6 %. The surface of 9CNT9 nanomembrane is smooth with a microroughness of 8.7 nm within $1\times1\ \mu m^2$ which is only slightly higher than the microroughness of purely polymeric nanomembranes (Figure 5.2b). The total thickness of the nanomembranes was about 60 nm as measured from the edge height (Figure 5.2).

Table 5.1. Structural and mechanical properties of nanomembranes

Name	Central Layer	Thickness nm	roughness nm	Elastic modulus GPa	Pressure mbar	Deflections nm
9CNT9 [a]	Carbon nanotubes	60	8.7	8.8±2.1	0-100	0-5000
9_9 [b]	None	35	3.8	1.5±1.0	0-50	0-5000
11_11 [c]	None	53	4.1	Similar to 9_9	0-20	0-2000

[a], $(PAH\text{-}PSS)_9PAH/CNT/(PAH\text{-}PSS)_9PAH$. [b] $(PAH\text{-}PSS)_{18}$ (Ref. 14). [c] $(PAH\text{-}PSS)_{22}$

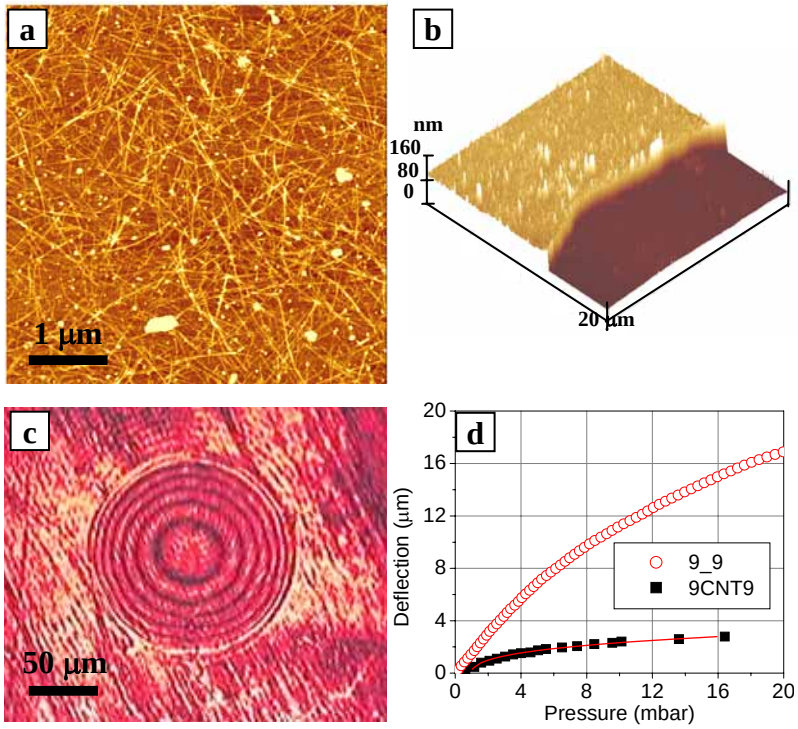

Figure 5.2. Structure, morphology and mechanical test of carbon nanotube contained nanomembranes. a) AFM topography of high density CNTs deposited onto the surface of polyelectrolyte multilayers; b) 3D topography of edge of 9CNT9 nanomembrane on silicon substrate; c) Interferometer pattern of bulged 9CNT9 membrane under pressure differential of 4 mbar; d) Deflection-pressure correlation of 9CNT9 and 9_9 free-suspended nanomembranes with diameter of 150 μm.

An interferometer pattern of deflecting nanomembranes displays a series of concentric Newton's rings indicating their dome-shape (Figure 5.2c). The deflection-pressure variation obtained from the interference patterns is presented in Figure 5.2d. The purely polymeric nanomembranes can be deflected multiple times to 15-18 μm with the applied pressure reaching 100 mbar. The 9CNT9 membrane shows much higher bending stiffness (deflections below 5 μm) caused by filler toughening effect due to the presence of the carbon nanotubes. In fact, the elastic modulus calculated from deflection-pressure data reached 8.8 GPa which is six times higher than that for purely polymeric

nanomembranes (Table 5.1). The values obtained here are similar to that reported earlier for thicker membranes reinforced with carbon nanotubes and clay/metal nanoparticles.[18]

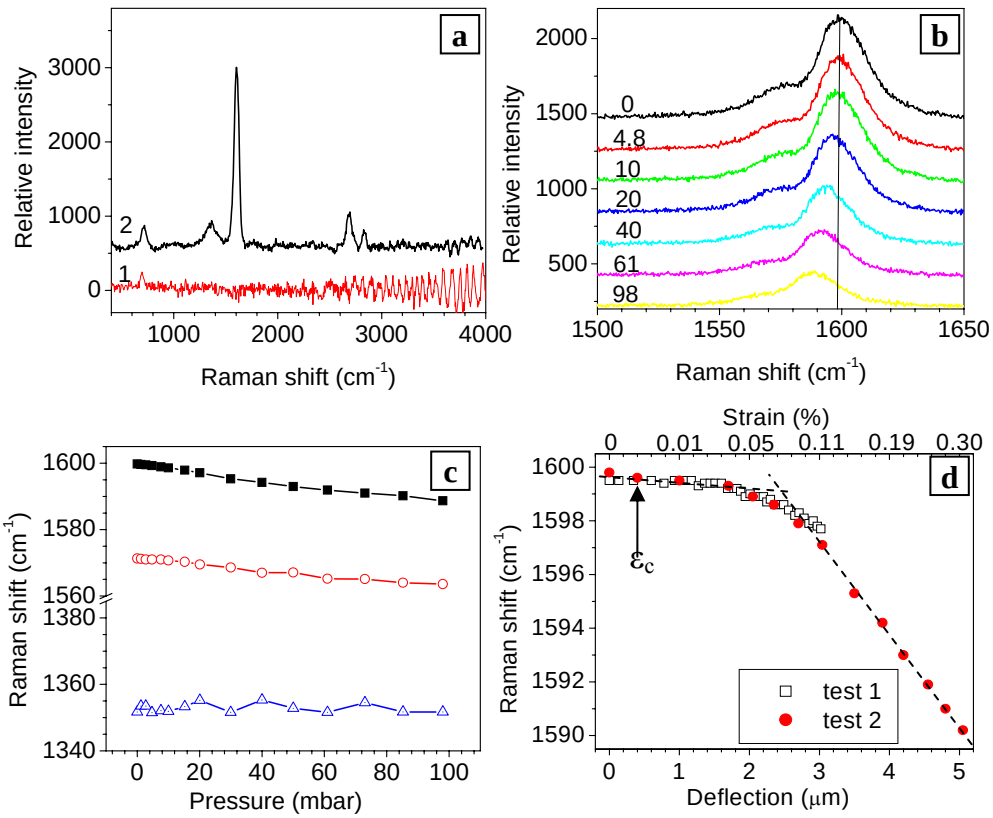

Figure 5.3. Raman spectra and data analysis of 9CNT9 nanomembranes. a) Comparison of Raman spectra of 9CNT9 nanomembrane (2) and pure polyelectrolyte multilayer 11_11 (1); b) High resolution Raman spectra of G bands of carbon nanotubes in the nanomembrane under pressure differential; c) Raman band shift of G bands and D band with the change of pressure differential applied to the 9CNT9 membrane; d) The relation of Raman G band position and nanomembrane deflection and strain during the bulging tests, low deflection region with small increments (1) and large deflection region with big steps (2).

A Raman spectrum of the free-suspended purely polymeric nanomembrane 11_11 in a rest state displayed noisy and low intensity background without any signs of peaks at 1400 and 1593 cm^{-1} which are most noticeable peaks for these polymers (Figure 5.3a,

oscillations in the range of 2600-4000 cm^{-1} is an instrumentation artifact).[19] Raman scattering changed dramatically for nanomembranes containing carbon nanotubes: the overall intensity increased by several orders of magnitude with strong peaks becoming clearly visible (Figure 5.3a). The characteristic CNT resonance Raman bands (G, D and G*) were clearly observed with other weaker Raman bands caused by the polymer matrix.[20, 21] For the rest state, the high resolution Raman spectrum of 9CNT9 nanomembrane gave peak positions as follows: D band at 1352 cm^{-1} and a G band (G^+) at 1599 cm^{-1} with the a left-side shoulder (G^-) of 1571 cm^{-1}. The peak width of G band, 20±3 cm^{-1}, was close to that reported on individual CNTs and bundles.[22,23]

The 9CNT9 nanomembranes were directly monitored with confocal Raman spectroscopy during the bulging test. This monitoring showed that the peak positions of both G and D band were shifted to lower frequency (Figure 5.3b,c). For the maximum deflection at 98 mbar, the G band was shifted to 1589 cm^{-1} (G^+ band) and to 1564 cm^{-1} (G^- band) (Figure 5.3b). The G^+ band was shifted by 10 cm^{-1} and the G^- band shift reached 8 cm^{-1}. The position of the D band remained unchanged within the experimental error (Figure 5.3c). All changes were completely reversible and repeatable. For further analysis, we selected G band at 1599 cm^{-1}, the sharpest peak in the Raman spectrum and collected high-resolution scans with a small pressure increment (Figure 5.3d). For further analysis, we plotted the peak position vs membrane deflection and converted deflection-pressure (*d*-*P*) into stress-strain (σ–ε) data according to the known relationship:[24]

$$\sigma = \frac{P a^2}{4 h d} \text{ and } \varepsilon = \frac{2 d^2}{3 a^2} \qquad (1)$$

This analysis revealed very intriguing features of the carbon nanotube deformation within deflected nanomembranes under combined bending and tensile stresses never observed before. Indeed, the peak position shifts were different for small and large deflections (Figure 5.3d). Below 2 μm deflection which corresponds to very low strain of <0.05% and stress below 10 MPa, the peak position shifted insignificantly, within 1 cm^{-1}. The behavior changed dramatically for higher deformations: the shift to a lower frequency became much more pronounced and reached 10 cm^{-1} for deflections within 2 - 5 μm, strains within 0.05 - 0.3%, stresses reaching 50 MPa, and the shift rate close to 36 cm^{-1} per 1% (Figure 5.3d).

This non-trivial behavior can be understood considering a complex regime of elastic deformation in free-suspended membranes and results on the deformed carbon nanotubes. [6,25] It has been already demonstrated that the mechanical strain modifies the CNTs band gap. Confocal Raman spectroscopy have shown that nanotube microstructure may change under mechanical stresses due to local bond stretching and defect reorganization.[26,27] For CNT composites, it was reported that the compressive strain can induce a higher frequency shift of the G-mode. [28] Significant shift to a lower frequency was predicted theoretically and observed experimentally for carbon nanotubes under stresses.[3,5,,29,30] It has been demonstrated that a shift rate can reach 10-20 cm^{-1} per 1% strain and can be used to monitor internal stresses and load transfer.[31]

We suggest that two different modes of Raman peak changes visualize two deformational regimes of the elastic deformation.[32] At small membrane deflections, the

deformation predominantly occurs through bending while in-plane tensile stress (the membrane regime) dominates larger deflections. Considering this mechanism, we suggest that initial small Raman shift reflects bending and buckling of carbon nanotubes. In fact, for sideways buckling, the critical strain ε_c can be estimated from:[33]

$$\varepsilon_c = (\pi a / L)^2 / 2. \qquad (2)$$

where a is a nanotube bundle diameter (3 nm) and L is the nanotube length (1-2 μm). Although the bending angle in this deformation range is low, the carbon nanotubes are already above the critical bending strain (ε_c = 0.005%). With this condition, bending stress causes the buckling of carbon nanotubes which releases local strain and bond deformation, thus, making the Raman shift very small. However, at higher deformations the membrane regime is taking place with predominant tensile stress acting within membrane interior. The membrane deflection higher than 2 μm results in the transition from the bending deformation to tensile regime. As a result of this change in deformation scenario, the shift rate increases dramatically and becomes even higher than that usually detected in tensile experiments for CNT composites. This difference indicates significant elastic deformation and high load transfer between LbL polyelectrolyte matrix and embedded nanotubes facilitated by wrapping them into amine-enriched PAH layer.

5.4. References

[1] Saito, R.; Dresselhaus, G.; Dresselhaus, M. S. *Physical Properties of Carbon Nanotubes*; Imperial College Press: London, **1998**.

[2] Tombler, T. W.; Zhou, C.; Alexseyev, L.; Kong, J.; Dai, H.; Liu, L.; Jayanthi, C. S.; Tang, M.; Wu, S. Y. *Nature* **2000**, *405*, 769.

[3] Li, Z.; Dharap, P.; Nagarajaiah, S.; Barrera, E. V.; Kim, J. D. *Adv. Mater.* **2004**, *16*, 640.

[4] a) Wood, J. R.; Zhao, Q.; Frogley, M. D.; Meurs, E. R.; Prins, A. D.; Peijs, T.; Dunstan, D. J.; Wagner, H. D. *Phys. Rev. B* **2000**, *62*, 7571. b) Zhao, Q.; Frogley, M. D.; Wagner, H. D. *Polym. Adv. Technol.* **2002**, *13*, 759. c) Zhao, Q.; Wanger, H. D. *Composites: Part A* **2003**, *34*, 1219.

[5] Zhang, X.; Liu, T.; Sreekumar, T. V.; Kumar, S.; Moore, V. C.; Hauge, R. H.; Smalley, R. E. *Nano Lett.* **2003**, *3*, 1285.

[6] Minot, E. D.; Yaish, Y.; Sazonova, V.; Park, J.-Y.; Brink, M.; McEuen, P. L. *Phys. Rev. Lett.* **2003**, *90*, 156401.

[7] Cronin, S. B.; Swan, A. K.; Ünlü, M. S.; Goldberg, B. B.; Dresselhaus, M. S.; Tinkham, M. *Phys. Rev. Lett.* **2004**, *93*, 167401.

[8] a) Lorén, A.; Engelbrektsson, J.; Eliasson, C.; Josefson, M.; Abrahamsson, J.; Abrahamsson, K. *Nano Lett.* **2004,** *4*, 309. b) Tian, Z-Q.; Ren, B.; Wu, D-Y. *J. Phys. Chem. B* **2002,** *106,* 9463. c) Pettinger, B.; Picardi, G.; Schuster, R.; Ertl, G. *Single Mol.* **2002,** *3,* 285.

[9] Thomsen, C.; Reich, S.; Maultzsch, J. *Phil. Trans. R. Soc. Lond. A.* **2004**, *362*, 2337.

[10] Doorn, S. K. ; O'Connell, M. J. ; Zheng, L. ; Zhu, Y. T. ; Huang, S.; Liu, J. *Phys. Rev. Lett.*, **2005**, *94*, 016802.

[11] Loa, I. *J. Raman Spectrosc.* **2003**, *34,* 611.

[12] Bridges, T. E.; Houlne, M. P.; Harris, J. M. *Anal. Chem.* **2004**, *76*, 576.

[13] a) Jiang, C.; Li, J.; Zhao, J.; Kolb, U.; Mews, A. *Nano Lett.*, **2002**, *2,* 1209. b) Jiang, C.; Kempa, K.; Zhao, J.; Schlecht, U.; Kolb, U.; Basché, T.; Burghard, M.; Mews, A.; *Phys. Rev. B* **2002**, *66*¸161404. c) Ko, H.; Pikus, Y.; Jiang, C.; Jauss, A.; Hollricher, O.; Tsukruk, V. V. *Appl. Phys. Lett.* **2004,** *85*, 2598.

[14] a) Jiang, C.; Markutsya, S.; Tsukruk, V. V. *Adv. Mater.* **2004***, 16,* 157. b) Jiang, C.; Markutsya, S.; Tsukruk, V. V. *Langmuir* **2004**, *20*, 882.

[15] a) Decher, G.; Schlenoff, B. S. (eds.) *Multilayer Thin Films,* Wiley-VCH, Weinheim, **2003.** b) P. T. Hammond, *Adv. Mater.* **2004**, *16*, 1271.

[16] a) Jiang, C.; Markutsya, S.; Pikus, Y.; Tsukruk, V. V. *Nature Mater*. **2004**, *3*, 721. b) Jiang, C.; Rybak, B. M.; Markutsya, S.; Kladitis, P. E.; Tsukruk, V. V. *Appl. Phys. Lett*. **2005**, *86*, 121912.

[17] Mamedov, A. A.; Kotov, N. A.; Prato, M.; Guldi, D.; Wicksted, J. P.; Hirsch, A. *Nature Mater.* **2002**, *1*, 190.

[18] Tang, Z.; Kotov, N. A.; Magonov, S.; Ozturk, B. *Nature Mater.* **2003**, *2*, 413.

[19] Sears, W. M.; Hunt, J. L.; Stevens, J. R. *J. Chem. Phys.* **1981**, *75*, 1589.

[20] a) Jorio, A.; Saito, R.; Dresselhaus, G.; Dresselhaus, M. S. *Phil. Trans. R. Soc. Lond. A.* **2004**, *362*, 2311. b) Jorio, A.; Pimenta, M. A.; Filho, A. G.; Saito, R.; Dresselhaus, G.; Dresselhaus, M. S. *New J. Phys.* **2003**, *5*, 139.

[21] Zhao, J.; Jiang, C.; Fan, Y.; Burghard, M.; Basché, T.; Mews, A. *Nano Lett.* **2002**, *2*, 823.

[22] Jorio, A.; Fantini, C.; Dantas, M. S. S.; Pimenta, M. A.; Souza, A. G.; Samsonidze, G. G.; Brar, V. W.; Dresselhaus, G.; Dresselhaus, M. S.; Swan, A. K.; Ünlü, M. S.; Goldberg, B. B.; Saito, R. *Phys. Rev. B* **2002**, 66, 115411.

[23] Ko, H.; Peleshanko, S.; Tsukruk, V. V. *J. Phys. Chem. B* **2004**, *108*, 4385.

[24] Beams, J. W. in *Structure and Properties of Thin Solid Film*, (Eds: C. A. Neugebauer, J. B. Newkirk, D. A. Vermilyea), John Wiley: New York **1959**, p 183.

[25] Maiti, A. *Nature Mater.* **2003**, *2*, 440.

[26] Hartschuh, A.; Sanchez, E. J.; Xie, X. S.; Novotny, L. *Phys. Rev. Lett.* **2003**, *90*, 095503.

[27] Jiang, C.; Zhao, J.; Therese, H. A.; Friedrich, M.; Mews, A. *J. Phys. Chem. B* **2003**, *107*, 8742.

[28] Dresselhaus, M. S.; Eklund, P. C. *Adv. Phys.* **2000**, *49*, 705.

[29] Yang, L.; Han, J. *Phys. Rev. Lett.* **2000**, *85*, 154.

[30] Ajayan, P. M.; Schadler, L. S.; Giannaris, C.; Rubio, A. *Adv. Mater.* **2000**, *12*, 750.

[31] Zhao, Q.; Wagner, H. D. *Phil Trans. R. Soc. Lond. A* **2004**, *362*, 2407.

[32] Timoshenko, S.; Woinowsky-Krieger, S. *Theory of Plates and Shells,* McGraw-Hill, New York, **1959**.

[33] Yakobson, B. I.; Brabec, C. J.; Bernholc, J. *Phys. Rev. Lett.* **1996**, *76*, 2511.

Chapter 6. Patterned Carbon nanotube arrays encapsulated into freely suspended flexible films

6.1. Introduction

Long-living free-standing organized micro- and nanostructures composed of nanowires and nanotubes are rarely demonstrated due to their extremely fragile nature. Instead, a vast majority of known nanostructures are fabricated and stay at solid surfaces which provide firm support but can severely alter their properties. Several rare examples of free-standing nanostructures include freely suspended carbon nanotubes, nanotube forests, and multilayered films.[1,2,3] Here, we suggest a novel approach for the fabrication of freely standing microarrays of carbon nanotubes by encapsulating them into robust albeit compliant polymeric nanofilms. For such sandwiched structures only nanoscale compliant barriers (below 20 nm thick) stand between a sandwiched carbon nanotube array and environment.

Freely suspended ultrathin (thickness of 100 – 1000 nm) membranes incorporating different functional nanomaterials have been recently suggested.[4,5,6,7] Freely suspended membranes containing nanoparticles have been fabricated by a number of approaches including layer-by-layer (LbL) assembly,[7] cast at air-water interfaces,[8] and spin-coating on sacrificial layer.[9] Carbon nanotube-containing membranes have recently been demonstrated to show several interesting properties such as high tensile strength approaching that of hard ceramics, electrical conductivity,[10] and controlled molecular transport.[11] On the other hand, freely suspended nanoscale (thickness below 100 nm)

membranes containing gold nanoparticles with high elasticity and robustness have been recently fabricated.[12] These nanomembranes might serve as pressure or acoustic microsensors replacing stiff silicon membranes.[13] Carbon nanotubes, with its excellent mechanical strength and unique electrical properties, represent excellent candidates for these multifunctional membrane sensors requiring high electrical conductivity and extreme robustness.[14]

Here, we demonstrate the successful fabrication of carbon nanotube microscopic arrays embedded into freely suspended LbL membranes by using spin-assisted LbL assembly and microcontact printing via sacrificial polymer patterning. Free-standing patterned polymer films have been fabricated by growth of polymer on patterned self-assembled monolayer.[15] Patterned assembly on polyelectrolyte multilayer has been previously demonstrated with colloids,[16,17] biological materials,[18,19] and nanoparticles.[20,21] These approaches involve patterning LbL multilayers by using polymer-on-polymer stamping technique with subsequent selective adsorption controlled by electrostatic interactions.[22,23]

6.2. Sample Preparations

For freely suspended nanomembranes, cellulose acetate was used as sacrificial layer and LbL multilayers were prepared by the spin-assisted self-assembly method which was described in detail elsewhere.[12,24] The experimental procedure for patterned arrays of carbon nanotubes is outlined schematically in Figure 6.1. Sacrificial PS micropatterns on LbL surfaces (PAH as a top layer) were obtained by microcontact

printing of PS ink (Mw=200000, 2% in toluene) with PDMS stamp.[25,26] CNT deposition was accomplished by blow-drying CNT solution with N_2 gas on the PS patterned substrate. The sacrificial PS layers were rinsed away with toluene, leaving only the patterned array of the carbon nanotubes strongly attached to the LbL multilayer. On the other hand, this removal exposed intact PAH-covered surface areas. On top of this patterned surface, additional polyelectrolyte multilayers were deposited by spin-assisted LbL. By dissolving sacrificial supporting CA layer in acetone, we transferred the patterned nanomembranes on either a TEM grid or a copper substrate with a 150μm opening. The overall microstructure is described by a general formula $(PAH/PSS)_9PAH/CNT/(PAH/PSS)_9PAH$. For confocal Raman characterization, the membranes were transferred on a glass surface. The bulging test of the freely suspended nanomembranes was conducted according to the procedure described elsewhere. Raman mapping and spectroscopy of the nanomembranes were conducted with a custom designed confocal Raman instrument based on Aurora-III near-field scanning optical microscope (DI).[27] A Nd:YAG laser (532 nm wavelength) was used as the light source.

6.3. Results and Discussion

We began the fabrication of the freely suspended carbon nanotube arrays by preparing LbL multilayer films on top of sacrificial layer by using spin-assisted LbL (Figure 6.1a). The thickness of such nanocomposite films with a formula $(PAH/PSS)_9/PAH/CNT/PAH(PAH/PSS)_9PAH$, was about 43 nm. The patterned nanotube array sandwiched between two LbL multilayers was transferred onto an opening in a copper substrate according to usual routine showed continuous parallel

stripes with spacing 10 microns (pre-determined by a stamp spacing) extended over the whole opening area, which indicates intact carbon nanotube arrays after transfer.

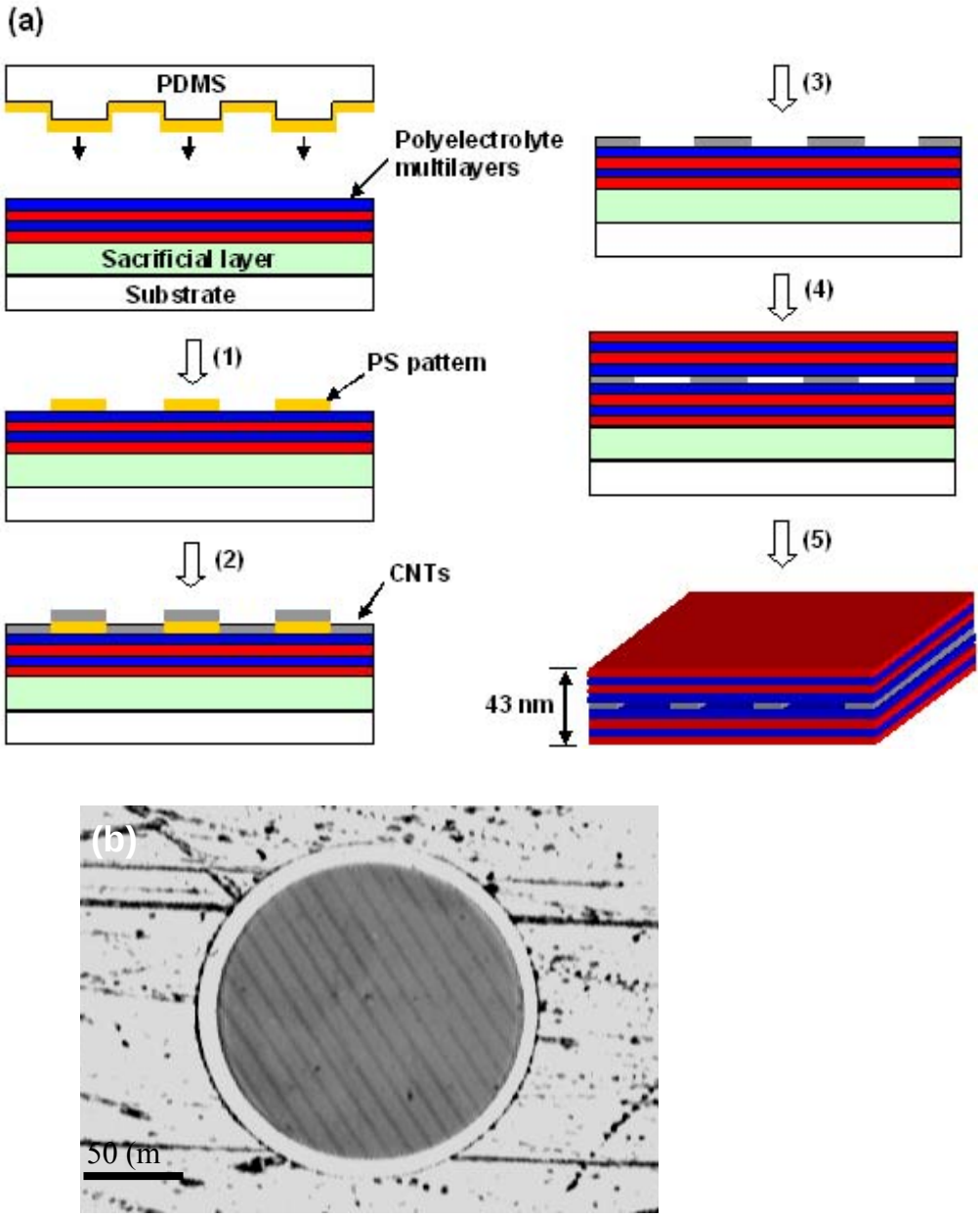

Figure 6.1. a) Schematic illustration of the fabrication procedure of the freely suspended carbon nanotube arrays: 1) the microcontact printing of PS onto polyelectrolyte multilayers; 2) Deposition of carbon nanotubes on the patterned substrates; 3) Removing PS layers; 4) Formation of topmost polyelectrolyte multilayers by LbL assembly; 5) Releasing carbon nanotube arrays by rinsing away the supporting sacrificial film. b) Optical image of freely suspended carbon nanotube array suspended over 150 μm hole.

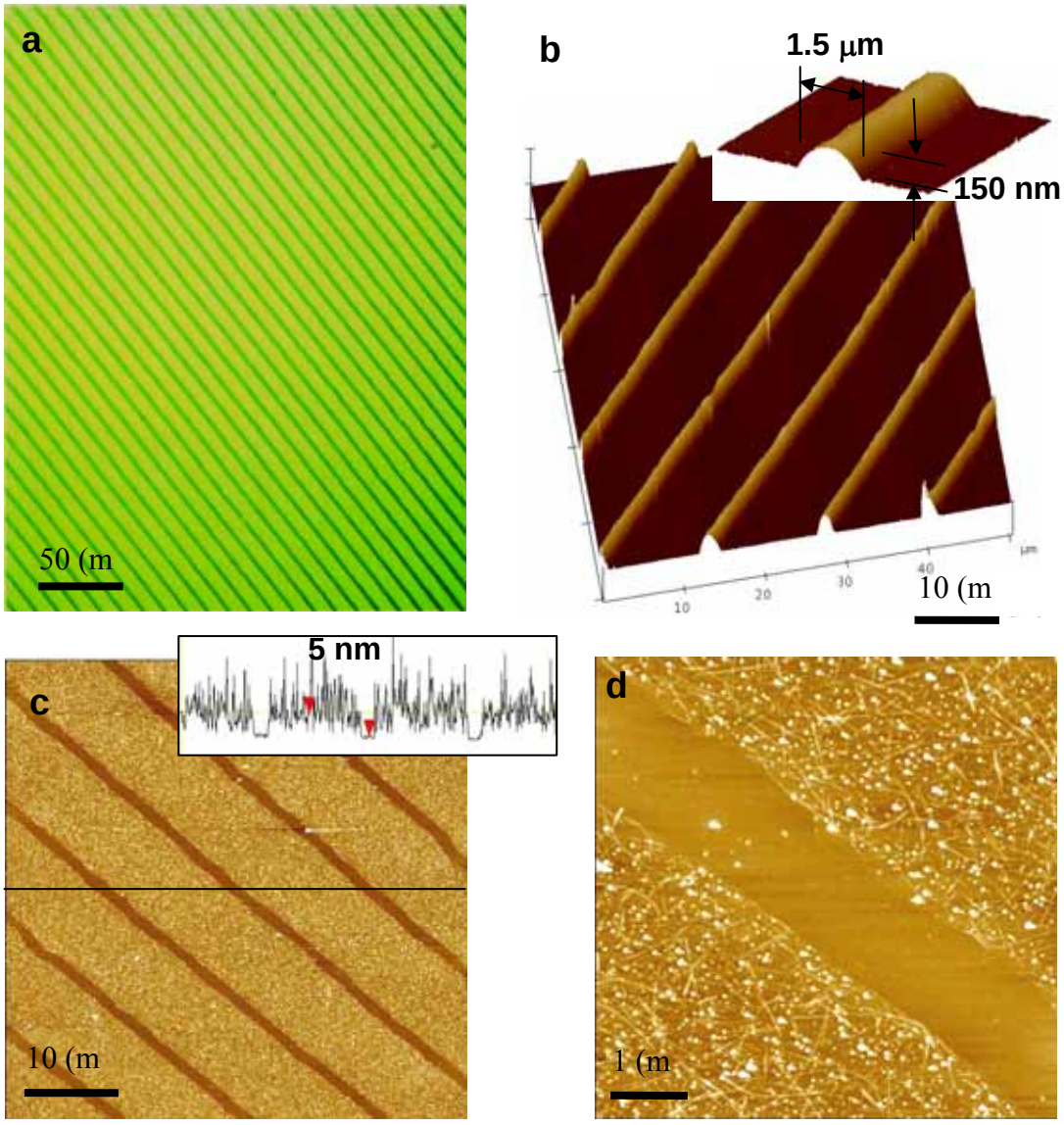

Figure 6.2. a) Optical and b) AFM images of Polystyrene micropatterns on top of PAH surface on a silicon substrate; c) and d) AFM images of patterned carbon nanotubes after removal of the PS template.

Figure 6.2a shows optical image of the PS sacrificial micropattern on PAH-terminated LbL surface on a silicon wafer, which demonstrates its high quality across a whole view area (~400 μm). Actually, the patterned area was limited by physical dimension of PDMS stamp (3×3 mm^2). The efficient transfer of PS layers from PDMS stamp to PAH surface was efficient and driven by differences in surface energies between

PDMS and PAH.[25, 28] Figure 6.2b shows AFM topographical images of the PS micropattern with close to ideal, rounded, semi-cylindrical shape of PS layers with a width of 1.5 μm and a height of 150 nm. This round shape is caused by the action of surface tension on transferred PS solution in the course of it evaporation.

We deposited carbon nanotubes on the patterned substrate and removed PS layers with toluene (Figure 6.2c). The quality of selective adsorption was high: we found almost no carbon nanotubes on the regions protected by PS layers (Figure 6.2d). Dissolving of the PS layer did not damage the polyelectrolyte multilayers. The height of carbon nanotube layer was close to 5 nm, which indicates a monolayer of carbon nanotube bundles (bundle diameter measured independently was within 3-5 nm). The surface density of nanotubes was estimated to be 18 tubes/μm^2 and can be controlled by solution concentration. These observations indicate that the interactions between PS sacrificial layers and PAH surface are strong enough to sustain solution processing for nanotube deposition and weak enough to be easily removed with a good solvent, which are key elements for successful patterning and transfer.

Confocal Raman mapping of the patterned films demonstrated excellent optical contrast caused by strong resonance Raman scattering from carbon nanotube areas. Figure 6.3a shows the surface distribution of the Raman G-mode obtained by integrating intensity at 1590cm^{-1} (a main resonance peak for carbon nanotubes).[29,30,31] Raman mapping shows clearly recognizable parallel lines separated by narrower dark stripes with 10 micron spacing.

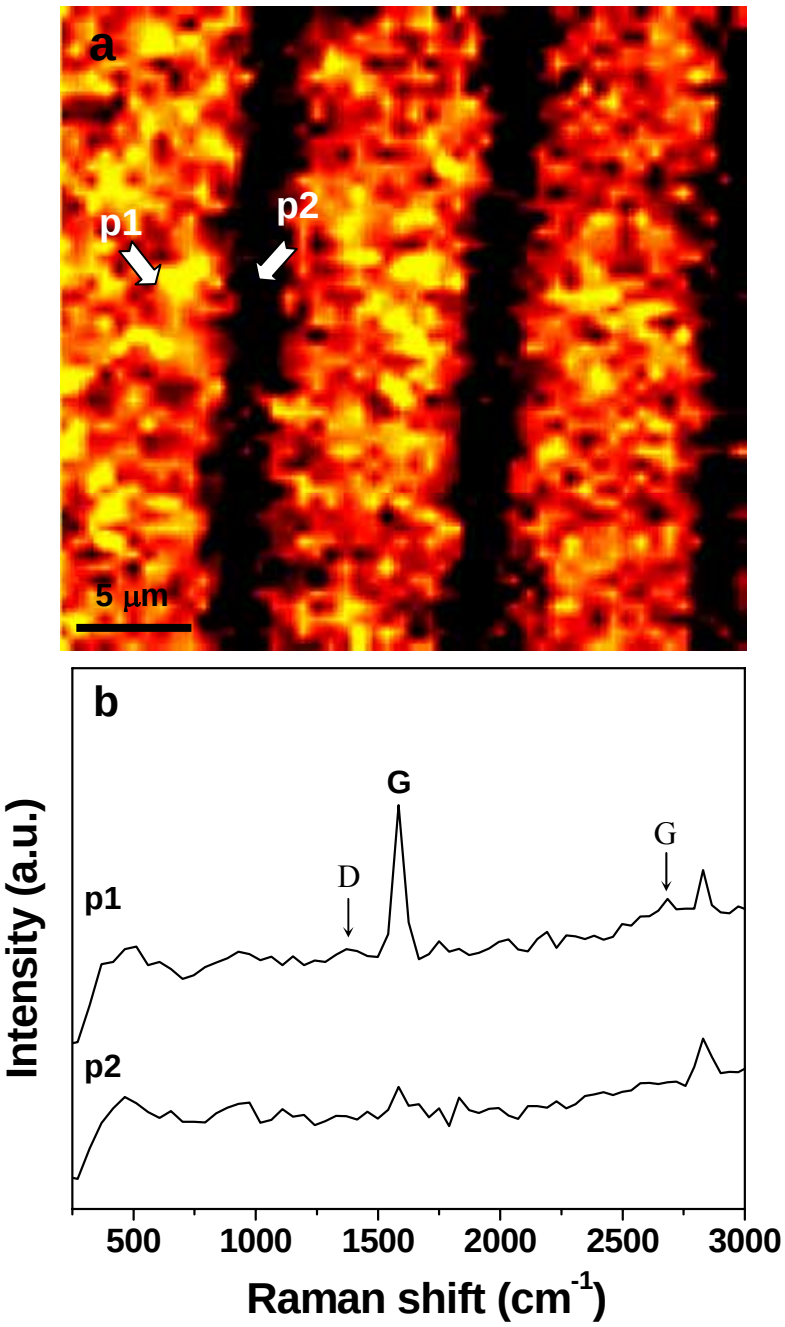

Figure 6.3. a) Raman mapping of the LbL membrane with embedded carbon nanotube array; b) Raman spectra of two different locations (with and without carbon nanotubes) in Figure 6.3a.

This Raman image clearly identifies the patterned carbon nanotube array inside the LbL membrane. Figure 6.3b shows representative Raman spectra on two different areas with (position 1, p1) and without (position 2, p2) carbon nanotubes (Figure 6.3a).

Raman spectra at position 2 showed no signs of known Raman features of carbon nanotubes with several weak features originated from PSS/PAH matrix.[32] In contrast, Raman spectra at position 1 displayed all typical spectral features of carbon nanotubes including D, G, and G′-modes with peak frequencies close to that of well-known peaks for as-obtained carbon nanotubes. This result indicates that neither oxidation process nor deposition routine affected significantly microstructure of carbon nanotubes encapsulated into LbL membranes. High optical contrast caused by the alternating layers into LbL membrane creates an efficient Raman grating with the variation of G-band intensity of 1:1000 and higher.

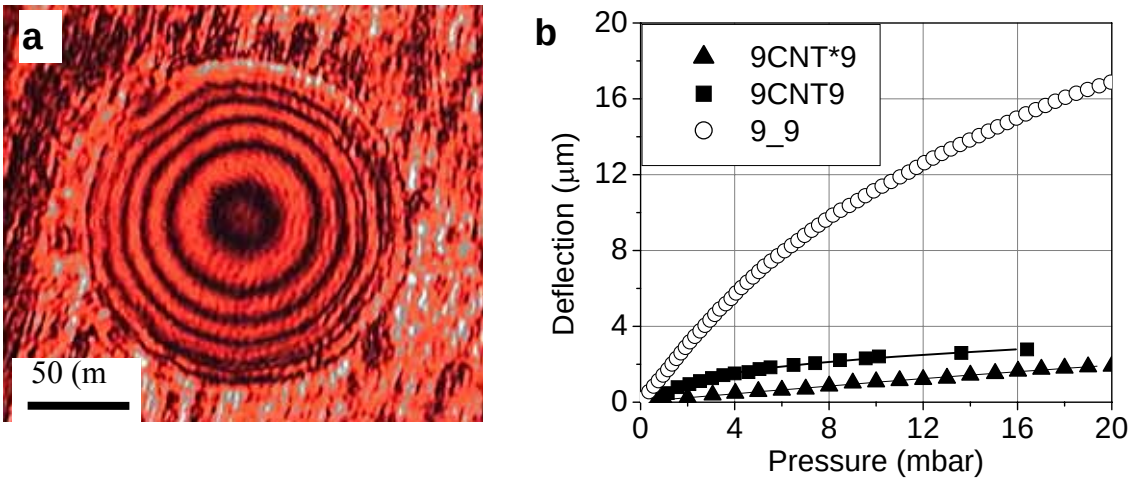

Figure 6.4. a) An interference pattern of the deflected freely suspended carbon nanotube array under bulging test; b) Deflection of freely suspended membranes with different content of carbon nanotubes determined from the bulging experiments.

As known, embedding carbon nanotubes into LbL free-standing films enhances their mechanical properties due to the filler toughening phenomenon. However, the question of the effect of the carbon nanotube encapsulation on the elastic properties of *patterned membranes* has been never addressed. Thus, we investigated the mechanical

behavior of freely suspended membranes by using interferometry. Figure 6.4a shows an example of interference pattern arising from membrane deflection under air pressure. By analyzing the interference pattern we calculated the deflection vs. applied pressure (Figure 6.4b). The deflection of the patterned membranes containing carbon nanotubes (9CNT*9) was much smaller than that for purely polymeric membranes (9_9) (Figure 6.4b). This difference indicates increasing bending stiffness and higher elastic modulus. Indeed, the analysis of the deflection vs. pressure according to the theory of the membrane elasticity, showed the elastic modulus of the freely suspended films with nanotube array within 6-9 GPa, which is much higher than that for purely polymer membranes (Table 6.1). The elastic modulus measured here for films containing a single layer of carbon nanotubes is very high as compared to regular polymer composites with similar matrices. This result confirms that the filler toughening mechanism is effectively enhances the elastic properties of the *patterned nanomembranes* similarly to that demonstrated for thick homogeneous LbL films. The observed elastic moduli were close to the composite elastic moduli predicted by the Takayanagi model assuming the elastic modulus of carbon nanotubes of 1 TPa and the isostrain condition for two phases (Table 6.1).[33]

These results suggest that the patterned geometry *does not prevent* the toughening of membrane elastic properties via encapsulation of nanoparticulate material. On the other hand, this result implies that we can fabricate freely suspended carbon nanotube arrays embedded in nanoscale polymer films without losing their excellent mechanical properties. This microfabrication routine proposed can be extended to the assembly of

freely suspended arrays of a variety of other nanomaterials, nanoparticles, and biological materials. These carbon nanotube arrays encapsulated into freely suspended films are expected to show anisotropic mechanical and electrical properties, which can be explored for potential applications for directional sensing and anisotropic electrical conducting.[34] These anisotropic properties are currently under investigation.

Table 6.1. Mechanical properties of freely suspended carbon nanotube membranes

Name	Thickness (nm)	CNT volume %	Elastic modulus (GPa)	Theoretical Elastic modulus (GPa)
9CNT*9[a]	43	0.4-0.8	5.9±0.9	5.5-9.5
9CNT9[b]	60	0.8-1.6	8.8±2.1	9.5-13.5
9_9[c]	35	0	1.5±1.0	NA

[a] $(PAH/PSS)_9/PAH/CNT/PAH(PAH/PSS)_9PAH$ with patterned carbon nanotube arrays
[b] $(PAH/PSS)_9/PAH/CNT/PAH(PAH/PSS)_9PAH$
[c] $(PAH/PSS)_{18}/PAH$

6.4. References

[1] Tombler, T. W.; Zhou, C. W.; Alexseyev, L.; Kong, J.; Dai, H. J.; Lei, L.; Jayanthi, C. S.; Tang, M. J.; Wu, S. Y. *Nature* **2000**, *405*, 769.

[2] Fan, S. S.; Chapline, M. G.; Franklin, N. R.; Tombler, T. W.; Cassell, A. M.; Dai, H. J. *Science* **1999**, *283*, 512.

[3] Wei, B. Q.; Vajtai, R.; Jung, Y.; Ward, J.; Zhang, R.; Ramanath, G.; Ajayan, P. M. *Nature* **2002**, *416*, 495.

[4] Decher, G.; Schlenoff, J. B. (Eds) *Multilayer Thin Films*; Wiley-VCH: Weinheim, 2003.

[5] Hammond, P. T. *Adv. Mater.* **2004**, *16*, 1271.

[6] Korchev, A. S.; Bozack, M. J.; Slaten, B. L.; Mills, G. *J. Am. Chem. Soc.* **2004**, *126*, 10.

[7] Mamedov, A. A.; Kotov, N. A.; Prato, M.; Guldi, D. M.; Wicksted, J. P.; Hirsch, A. *Nat. Mater.* **2002**, *1*, 190.

[8] Lim, M. H.; Ast, D. G. *Adv. Mater.* **2001**, *13*, 718.

[9] Porel, S.; Singh, S.; Harsha, S. S.; Rao, D. N.; Radhakrishnan, T. P. *Chem. Mater.* **2005**, *17*, 9.

[10] Wu, Z. C.; Chen, Z. H.; Du, X.; Logan, J. M.; Sippel, J.; Nikolou, M.; Kamaras, K.; Reynolds, J. R.; Tanner, D. B.; Hebard, A. F.; Rinzler, A. G. *Science* **2004**, *305*, 1273.

[11] Hinds, B. J.; Chopra, N.; Rantell, T.; Andrews, R.; Gavalas, V.; Bachas, L. G. *Science* **2004**, *303*, 62.

[12] Jiang, C.; Markutsya, S.; Pikus, Y.; Tsukruk, V. V. *Nat. Mater.* **2004**, *3*, 721.

[13] Elsenspoek, M.; Wiegerink, R. *Mechanical Microsensors*; Springer: New York, 2001.

[14] Dresselhaus, M. S.; Dresselhaus, G.; Avouris, Ph. (Eds) *Carbon nanotubes: Synthesis, Structure, Properties, and Applications*; Springer: New York, 2001.

[15] Huck, W. T. S.; Stroock, A. D.; Whitesides, G. M. *Angew. Chem. Int. Ed.* **2000**, *39*, 1058.

[16] Zheng, H. P.; Lee, I.; Rubner, M. F.; Hammond, P. T. *Adv. Mater.* **2002**, *14*, 569.

[17] Lee, I.; Zheng, H. P.; Rubner, M. F.; Hammond, P. T. *Adv. Mater.* **2002**, *14*, 572.

[18] Kidambi, S.; Lee, I.; Chan, C. *J. Am. Chem. Soc.* **2004**, *126*, 16286.

[19] Berg, M. C.; Yang, S. Y.; Hammond, P. T.; Rubner, M. F. *Langmuir* **2004**, *20*, 1362.

[20] Jaffar, S.; Nam, K. T.; Khademhosseini, A.; Xing, J.; Langer, R. S.; Belcher, A. M. *Nano Lett.* **2004**, *4*, 1421.

[21] Tokuhisa, H.; Hammond, P. T. *Langmuir* **2004**, *20*, 1436.

[22] Jiang, X. P.; Hammond, P. T. *Langmuir* **2000**, *16*, 8501.

[23] Jiang, X. P.; Zheng, H. P.; Gourdin, S.; Hammond, P. T. *Langmuir* **2002**, *18*, 2607.

[24] Jiang, C.; Markutsya, S.; Tsukruk, V. V. *Adv. Mater.* **2004**, *16*, 157.

[25] Kim, Y. S.; Baek, S. J.; Hammond, P. T. *Adv. Mater.* **2004**, *16*, 581.

[26] Xia, Y. N.; Whitesides, G. M. *Angew. Chem. Int. Ed.* **1998**, *37*, 551.

[27] Ko, H.; Pikus, Y.; Jiang, C.; Jauss, A.; Hollricher, O.; Tsukruk, V. V. *Appl. Phys. Lett.*

2004, *85*, 2598.

[28] Meitl, M. A.; Zhou, Y. X.; Gaur, A.; Jeon, S.; Usrey, M. L.; Strano, M. S.; Rogers, J. A. *Nano Lett.* **2004**, *4*, 1643.

[29] Rao, A. M.; Richter, E.; Bandow, S.; Chase, B.; Eklund, P. C.; Williams, K. A.; Fang, S.; Subbaswamy, K. R.; Menon, M.; Thess, A.; Smalley, R. E.; Dresselhaus, G.; Dresselhaus, M. S. *Science* **1997**, *275*, 187.

[30] Saito, R.; Dresselhaus, G.; Dresslhaus, M. S. *Physical Properties of Carbon nanotubes*; Imperial College Press: London, 1998.

[31] Jorio, A.; Saito, R.; Hertel, T.; Weisman, R. B.; Dresselhaus, G.; Dresselhaus, M. S. *MRS Bull.* **2004**, 29, 276.

[32] Dong, W. F.; Sukhorukov, G. B.; Mohwald, H. *Physical Chemistry Chemical Physics* **2003**, *5*, 3003.

[33] Sperling, L. H. *Polymeric Multicomponent Materials* (Wiley, New York, 1997).

[34] Hulvat, J. F.; Stupp, S. I. *Adv. Mater.* **2004**, *16*, 589.

Chapter 7. Capillary Transfer Lithography for Patterned CNT Membranes

7.1. Introduction

Functionalized organic and polymeric thin films containing conducting, sensitive, optically active, and luminescent nanomaterials are of great importance in many emerging applications in sensors, photonics, and electronics.[1,2,3,4] Layer-by-layer (LbL) assembly, which is based on electrostatic assembly of oppositely charged species, is effective and versatile approach to the creation of ultrathin organic multilayered films with well-defined internal structure.[5,6] This technique has been extended to incorporate a variety of functional materials such as colloids,[7,8] biomaterials[9], inorganic nanoparticles,[10,11] quantum dots,[12,13] and carbon nanotubes[14] into LbL films. For the successful applications of these functionalized films in microelectronic devices, the controlled assembly of two- and three-dimensional (2D/3D) organized arrays within these multilayered structures is critical.

Microscopic patterning of different functional materials on polyelectrolyte films with high lateral resolution has been recently demonstrated by using chemical composition variation imposed by polymer-on-polymer stamping technique.[15,16] Subsequent selective attachment of functional materials on these patterned surfaces using electrostatic and other intermolecular interactions has been obtained. This way, a variety of complex patterns from various materials such as colloids,[17,18] biological materials,[19,20] and nanoparticles[21,22] has been demonstrated on chemically patterned LbL films.

However, strict control over the LbL surface morphology and pH or ionic strength of solution is required to achieve high selectivity over large areas which can be a challenge for some materials. In addition, the pattern contrast in these cases is limited by the selectivity of site-specific deposition, which can be masked by strong nonspecific attractions for systems with weak chemical contrast.

Controlling the selectivity in the surface assembly by tuning the chemical affinity of the patterned surfaces and solution conditions is even harder for materials with low surface charge density and for materials with strong non-specific interactions. One example is the oxidized carbon nanotubes which show modest-to-weak deposition selectivity for chemical patterns of self-assembled monolayers [23,24] as well as for positively charged poly(allylamine hydrochloride) (PAH) and negatively charged poly(sodium 4-styrenesulfonate) (PSS), classical polyelectrolytes for LbL technology. This weak selectivity is possibly due to strong van der Waals attraction combined with weak specific chemical interactions of few chemical groups available. Therefore, the reliable fabrication of precisely designed micropatterned arrays of carbon nanotubes or other weakly-interacting materials on top of weakly interacting polymer multilayers with variable surface composition [25] represents a great challenge. To overcome this challenge, a number of alternative methods have been recently suggested. For example, patterned LbL multilayers[26] or amphiphilic molecules[27] have been prepared by depositing target materials on a poly(dimethylsiloxane) (PDMS) stamp and then transferring them to LbL multilayers. Direct application of photolithography to LbL films has been recently suggested.[28] Selective build-up of 3D structures of multiple quantum dots has been

reported by modification of quantum dot surface coatings and choosing a proper assembly partner.[29] Although these approaches have shown high pattern contrast and good lateral resolution, there were some limitations for achieving high surface density of functional materials because of low reactivity of PDMS surface. On the other hand, the fabrication of well-defined 3D structures was limited by confined space between substrate and protruding areas of a stamp.

Utilizing polymer pattern as a sacrificial template or mask for subsequent assembly is widely used in microelectronic technology (photoresists for lift-off process).[30] Similar approach can be exploited to increase selectivity and contrast of patterned arrays avoiding non-specific adsorption on the protected surface areas. In fact, polymer nano- and microstructures have proven to be very successful in patterned etching of solid substrates or in selective deposition of functional materials.[31,32,33] Soft-lithography, which uses PDMS elastomer as a stamp or a mold, has been an efficient technique to prepare 2D and 3D polymer nano- or microstructures on various solid surfaces including silicon, glass, and metal substrates.[32,33,34,35] For example, nanoscale patterns of 2D polymer has been prepared by microcontact printing and used as a scaffold for the deposition of gold nanoparticles.[36] Moreover, well-defined 3D polymer microstructures have been fabricated by using various molding methods including imprint lithography,[37,38] microtransfer molding,[39] micromolding in capillaries,[40,41] solvent-assisted micromolding,[42] and capillary force lithography.[43] In these processes, an elastomeric master is usually pressed into a compliant polymer film which has been softened by heat or solvent, enabling the polymer to fill the recessed areas of the master

by capillary forces. In most cases, additional dry etching process is needed to remove a residual film of the polymer remainings in the compressed areas. Exceptions were found when the residual film was thin and the interaction between the polymer and substrate was very weak.[43,44] As was discussed for capillary force lithography, the microcontact printing uses the protruding region of PDMS stamp to transfer thin polymer layer onto target substrate. [45] In this method, lateral spacing is determined by original stamp dimension, but the control of the vertical dimension and a 3D shape are limited by de-wetting behavior of polymer solution confined between the stamp and the substrate.

There are several issues to be addressed in order to use polymer microstructures as a sacrificial template for subsequent assembly of weakly-interacting functional materials on the surface of polyelectrolyte multilayers. First, the process of patterning should be compatible with the polyelectrolyte multilayer surface composition. Heat treatment or etching process may affect some polyelectrolytes. Second, the polymer pattern should form "open" microstructure exposing surface chemicals of the underlying substrate for the subsequent adsorption. Third, the sacrificial polymer pattern should be easily removed without *affecting* the underlying substrate after being used as mask. For this purpose, the interaction between polymer protective layer deposited and the polyelectrolyte surface should be weak with secondary interactions such as van der Waals attraction. Finally, the fidelity and the edge sharpness of 3D polymer microstructures should be high enough for 2D or 3D assembly of functional materials with a submicron resolution.

Finally, although the microcontact printing has been widely used for the patterning polymer structures on the surface of LbL multilayers as we discussed above, it is usually limited in the formation of well-defined *open* 3D polymer microstructures. The high-resolution patterning with the open possibility for the fabrication of the *encapsulated arrays* by conformal coverage of these arrays with a topmost LbL multilayer is rarely demonstrated.

Here, we demonstrate the extensive capabilities of polymer sacrificial templates for the encapsulation of organized arrays from both carbon nanotubes and gold nanoparticles within polyelectrolyte multilayers by introducing novel polymer patterning technique for the sake of well-defined, high resolution 3D patterning. We suggest a variant of soft-lithography technique, termed capillary transfer lithography (CTL), which is based on capillary filling approach and transfer molding for the creation of 3D polymer open-structures onto polyelectrolyte LbL multilayers. We employed the easy creation of transferable polymer microstructures inside the recessed regions of the PDMS mold. Finally, we demonstrated the ability of CTL approach for the creation of sacrificial 3D polymer microstructures onto LbL surfaces and the fabrication of the well-defined 2D arrays encapsulated into LbL films.

7.2. Sample Preparations

The experimental procedures for patterning polymer onto polyelectrolyte multilayers, deposition of nanoparticulate materials, and their encapsulation are outlined schematically in Figure 7.1. LbL multilayers were prepared on silicon substrate by the

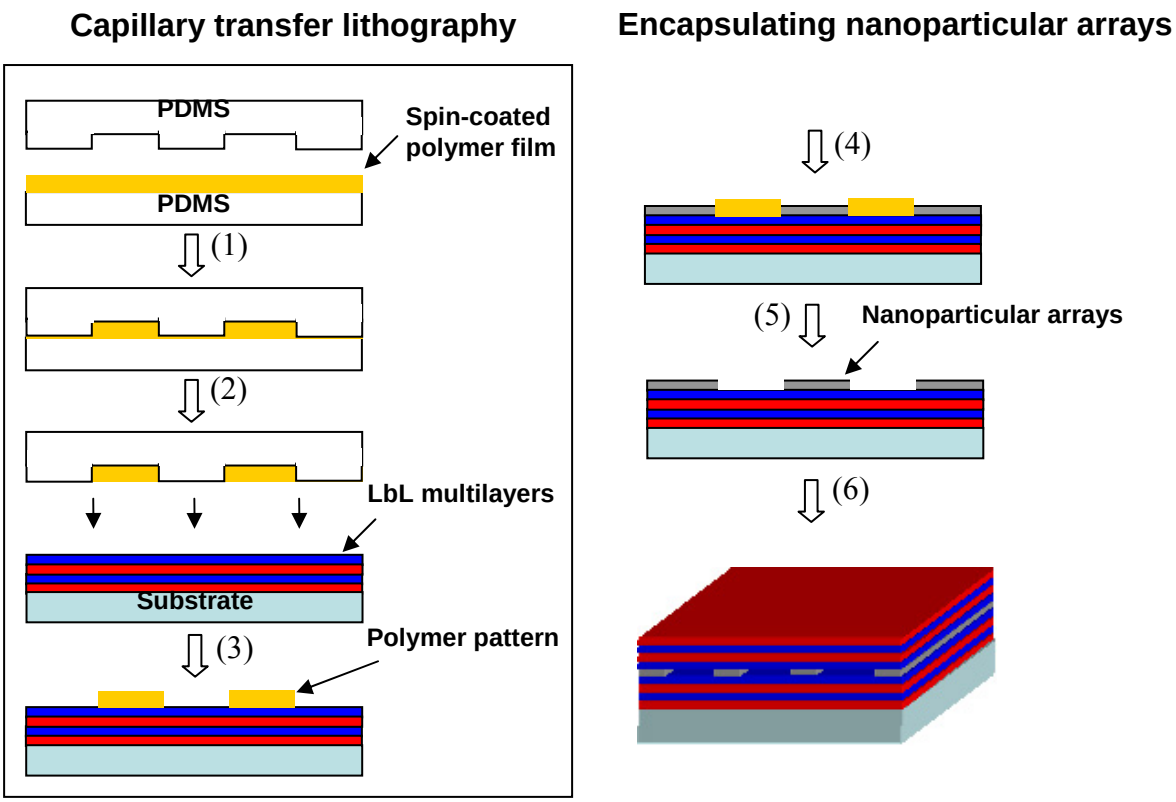

Figure 7.1. Schematic of patterning process by capillary transfer lithography and the subsequent assembly of encapsulated nanoparticular arrays: 1) The PDMS mold contacting spin-coated polymer film. 2) Release the PDMS mold. 3) Contacting the LbL multilayer and transferring the polymer pattern. 4) Selective deposition of nanoparticular arrays on unprotected surface areas. 5) Removal of sacrificial polymer pattern by rinsing with solvent. 6) Encapsulation of the nanoparticle array by the assembly of topmost LbL film.

spin-assisted LbL (SA-LbL) method which is described in detail elsewhere.[4,46] For LbL deposition, PAH (0.2wt %) and PSS (0.2wt %) aqueous solutions were prepared. Sacrificial polystyrene (PS) micropatterns on top of LbL multilayers (PAH as a top layer) were obtained by using capillary transfer lithography (Figure 7.1). For this process, PDMS substrate was soaked in toluene for 1–2 min before a thin PS film was prepared on a PDMS substrate by spin-coating of PS ink (Mw=200,000, 2% in toluene) at 3000 rpm for 20 s. A PDMS mold with the appropriate pattern was then brought in the conformal contact with the PS film on the PDMS substrate and pressed for 1 min. When PDMS

mold was detached from the PDMS substrate, the patterned polymer layer was trapped inside the recessed regions of the PDMS mold. The polymer pattern formed this way was then immediately transferred onto LbL surface by the conformal contact of the PDMS mold with the LbL film for 1 min.

For gold nanoparticle adsorption, a few drops of gold nanoparticle solution were evenly placed onto the patterned substrate and stored for 30 min at ambient laboratory conditions. The substrate was then washed with Nanopure water several times and dried with nitrogen gas. For CNT adsorption, a few drops of CNT solution were evenly distributed onto the patterned substrates and blow-dried with N_2 gas. This step was repeated for several times to increase the surface density of CNTs. After adsorption of gold nanoparticles or CNTs, the sacrificial PS template pattern was gently rinsed away with toluene, leaving only the patterned array of gold nanoparticles or CNTs strongly attached to the PAH-terminated areas of LbL multilayers. The removal of PS templates exposed intact PAH-terminated surface areas, which was further used for encapsulating nanoparticular arrays into LbL multilayers by continuing SA-LbL deposition of the LbL film starting from PSS. The resulting topmost film conformably covered the complete specimen (Figure 7.1).

7.3. Results and Discussion

7.3.1. Polymer Pattern Formation

Figure 7.2 shows topographical images of the PS micropattern obtained onto LbL film by this microcontact printing. The line spacing was 10 μm (Figure 7.2a) and the line

width was 1.5 μm (Figure 7.2b), which all are close to original stamp dimensions. Figure 7.2c, d show 3D PS microstructure with close to ideal, rounded, semi-cylindrical

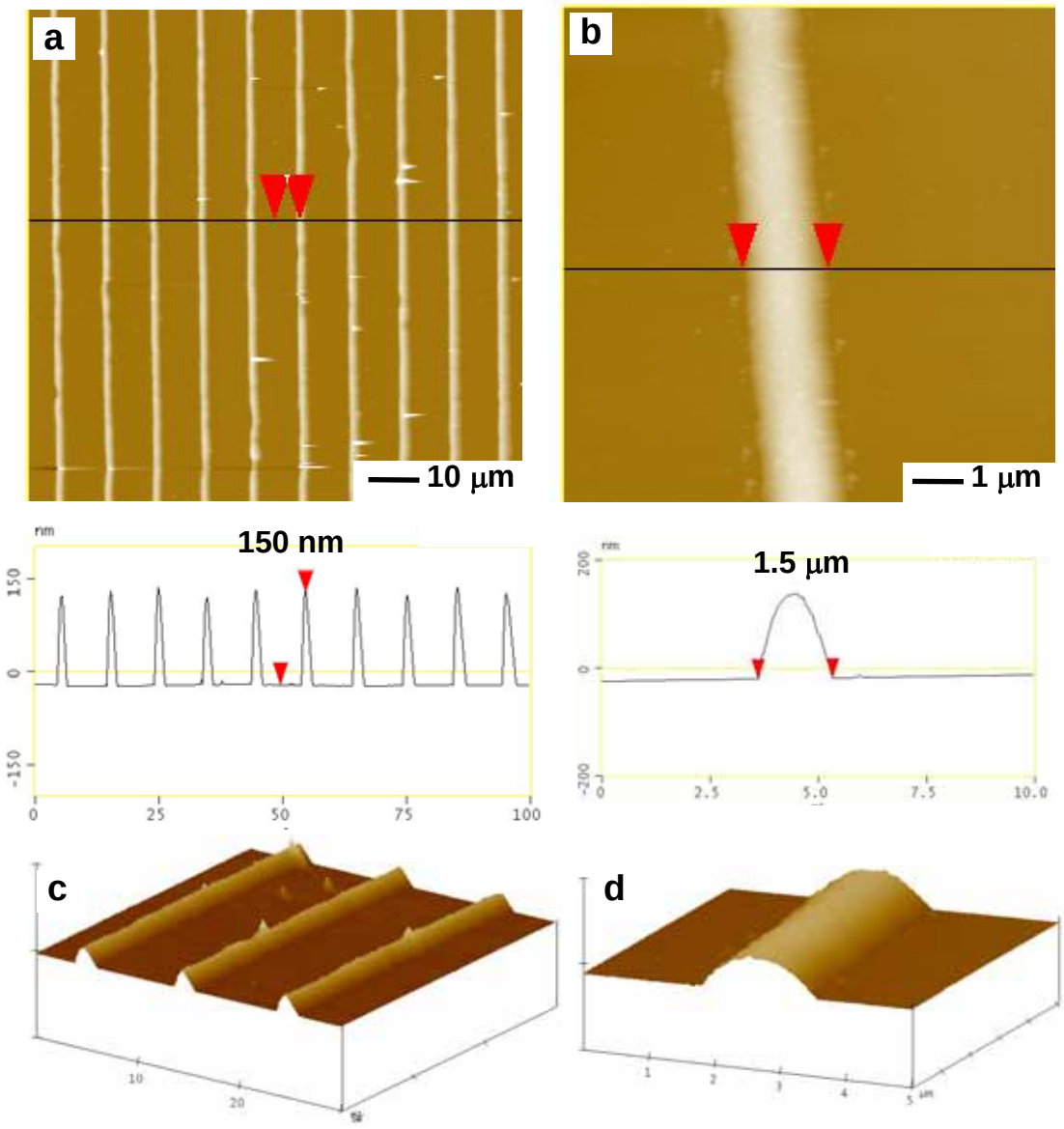

Figure 7.2. AFM images of PS micropattern prepared by microcontact printing on top of PAH-terminated LbL film on a silicon substrate: a,b) topographical images and corresponding cross-sections at different scales c, d) 3D AFM images.

shape of PS layers with a width of 1.5 μm and a height of 150 nm. The sharp boundaries

between protected and unprotected areas typically have a width of 50 nm and less (Figure 7.2b). This round shape is caused by the action of surface tension on transferred PS solution in the course of its evaporation.

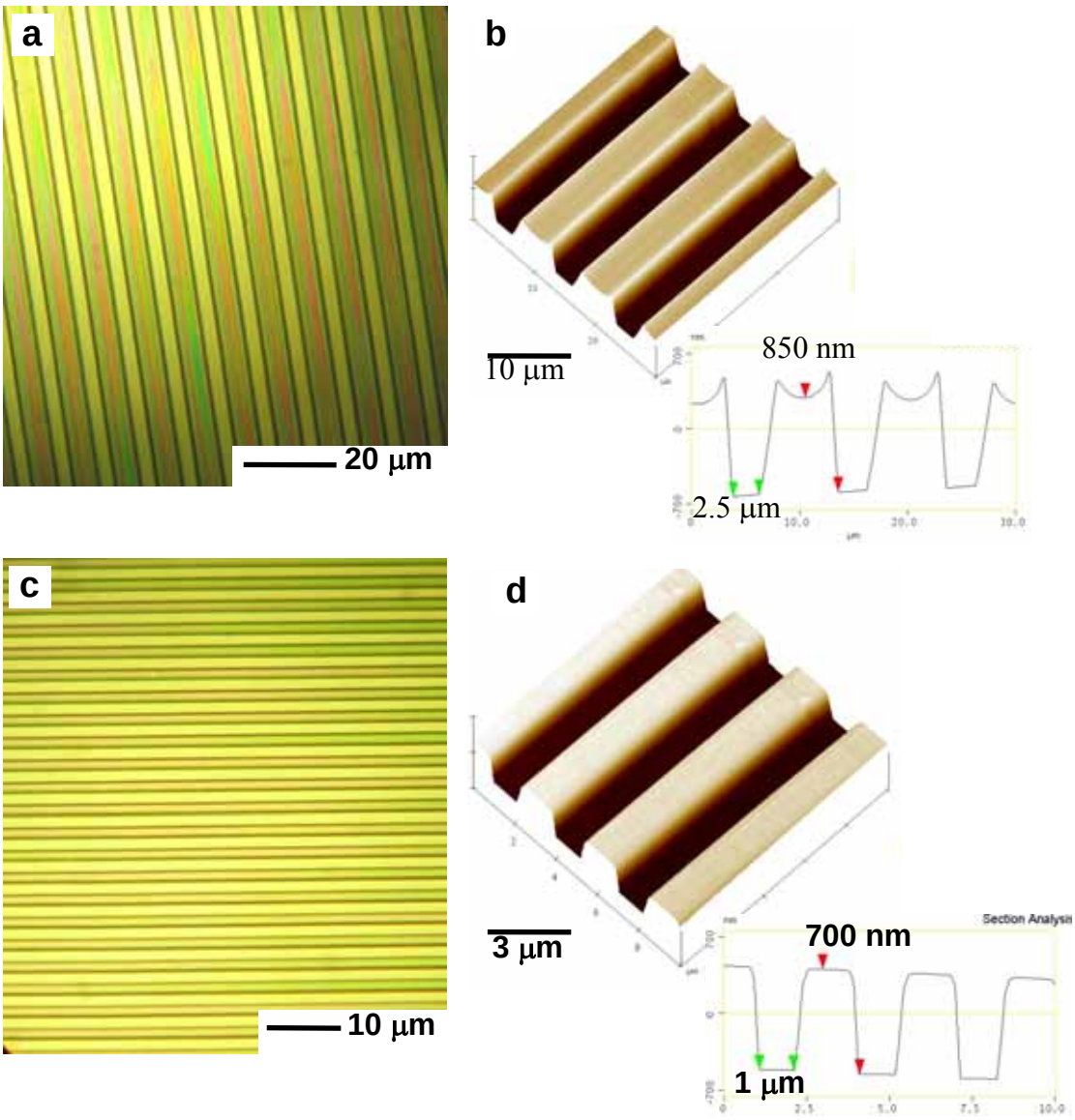

Figure 7.3. Optical (a,c) and AFM (b,d) topographical images and cross-sections for PS micropatterns prepared by capillary transfer lithography with two different PDMS molds on PAH-terminated LbL film.

PS microstructures prepared by CTL method are slightly different from that prepared by conventional microcontact printing reflecting different physical processes occurring. Figure 7.3a shows optical image of the PS micropattern formed by CTL printing onto the PAH-terminated LbL multilayer surface, which demonstrates its high quality and sharp edges. AFM image (Figure 7.3b) illustrates well-defined 3D PS microstructure with 2.5 μm spacing and 850 nm height, which is a replica of the PDMS mold. A meniscus edge on the top of polymer features was caused by incomplete filling the recessed regions of the mold. Recently, this kind of the meniscus edge has been used to generate PDMS stamp for high-resolution soft-lithography.[47]

CTL printing was also successful in preparing 3D PS microstructures with smaller lateral dimensions. As can be seen in Figure 7.3c, smaller PS micropattern showed uniform parallel stripes with 1.5 μm width and perfect spacing. AFM image (Figure 7.3d) clearly revealed the well-defined 3D structure of parallel lines with 700 nm height and 3 μm spacing (1.5 μm separation between polymer areas) with the width of the polymer-substrate transition zone below 50 nm. We observed no meniscus edges, which indicates that the soften polymer completely fills the recessed region of the mold. From these observations, we concluded that the softened polymer inside the recessed regions of mold can be effectively trapped by the PDMS mold and completely transferred to the PAH surface due to the compression elasticity of the PDMS mold and differences in surface energies between PDMS and PAH.[48]

The basic principle of CTL printing, which uses capillary filling of polymers softened by solvent, is similar to capillary force lithography or solvent-assisted micromolding introduced recently.[42,43] First, as illustrated in Figure 7.4, the solvent can be constantly re-supplied from the pre-soaked PDMS substrate to the polymer layer and soften the polymer. The resulting polymer solution fills the recessed region of PDMS mold by capillary filling. Second, the low surface energy of the PDMS substrate decreases the interaction with polymer enabling the formation of polymer open-structure. Softened polymer film between two PDMS surfaces is repelled with no residual polymer film found between the PDMS mold and substrate (Figure 7.4).

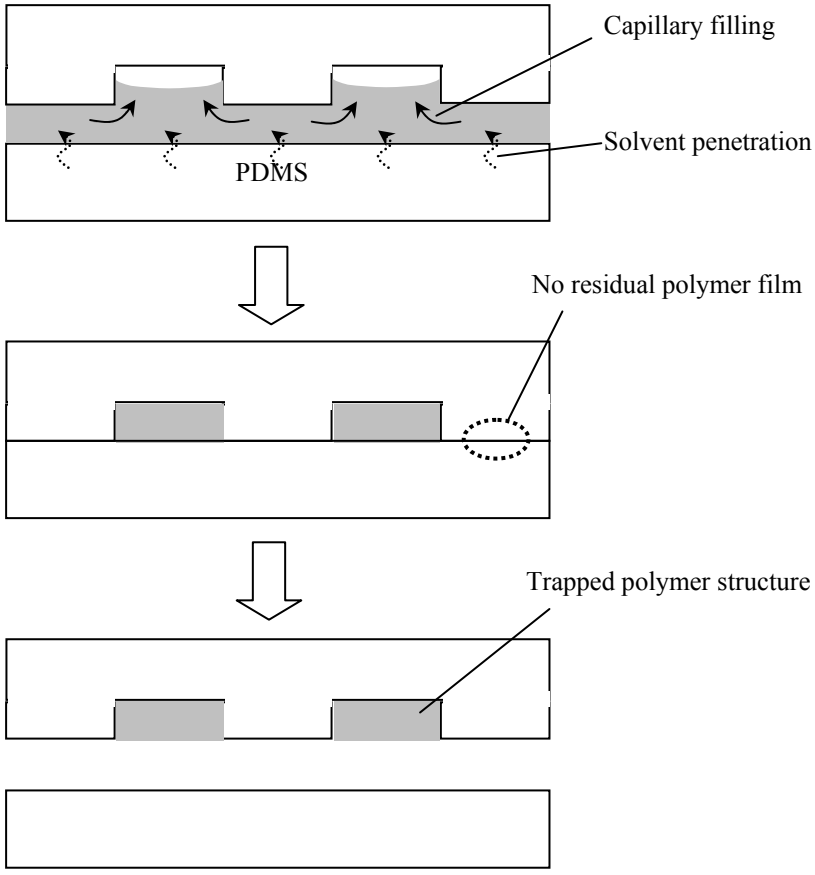

Figure 7.4. Schematic of interactions between PDMS mold, polymer layer, and PDMS substrate during the capillary transfer lithography.

The employment of the PDMS substrate in molding process makes our process versatile. The use of PDMS in our CTL process has several advantages for preparing 3D polymer microstructures due to its low surface energy, elasticity, and solvent swelling properties.[49,50] The elasticity and low surface energy of PDMS also enables the efficient transfer of this polymer microstructure to other substrates with higher surface energy. When this mold is immediately placed on the LbL film and pressed, the polymer inside the negative structure is transferred to the polyelectrolyte surface, resulting in 3D patterned polymer microstructure with sharp boundaries which is complementary to PDMS pattern.

7.3.2. Formation of Open Nanoparticulate Arrays

Next, we used these patterned polymer microstructures as sacrificial templates for the formation of carbon nanotube and gold nanoparticle arrays located on the surface of LbL films. After the selective deposition of these nanomaterials on the protected LbL surfaces, the PS micropattern was easily removed by rinsing with toluene, a good solvent for PS, leaving only the patterned array of carbon nanotubes or gold nanoparticles strongly attached to the LbL multilayers alternating with intact surface areas of LbL film (Figures 7.5–8).

Figure 7.5 shows the patterned arrays of carbon nanotubes and gold nanoparticles fabricated by using 10 μm PS micropatterns. Apparently that dissolving the PS pattern did not damage the polyelectrolyte multilayers, because the thickness of multilayer did not change and the surface morphology appeared unchanged. The boundaries between

areas remained sharp as well (about 50 nm) (Figure 7.5). The height of gold nanoparticles of 13 nm indicated a monolayer of gold nanoparticles. The height of carbon nanotube layer was around 5 nm, which indicates a monolayer of carbon nanotube bundles. We were able to achieve high quality patterns complementary to PS patterns with good uniformity over the entire surface area. These observations indicate that the interaction between PS sacrificial structures and the PAH surface was strong enough to sustain solution treatment in deposition step but weak enough to allow easily dissolving with a good solvent. This balance is a critical element for successful patterning and transfer suggested here.

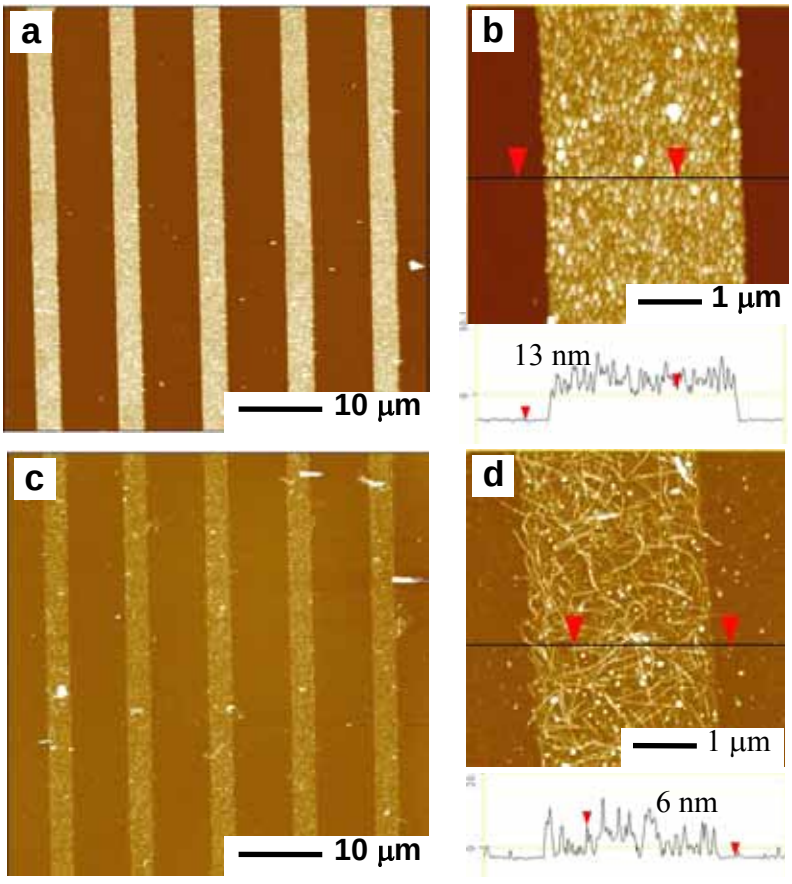

Figure 7.5. AFM topographical images at different scales and corresponding cross-sections of stripes of gold nanoparticle (a, b) and carbon nanotube (c, d) selectively deposited on LbL film.

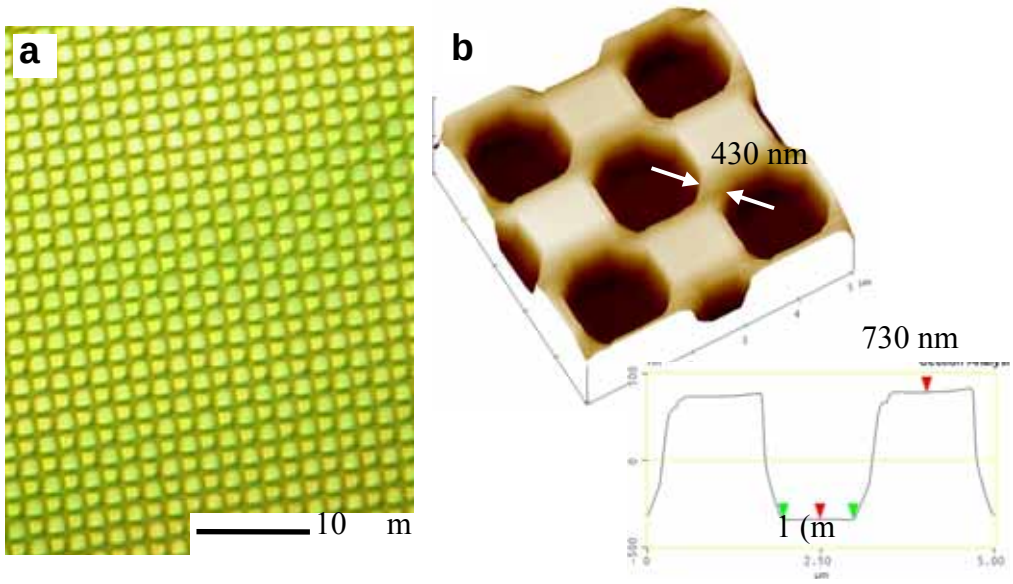

Figure 7.6. Optical (a) and AFM topographical (b) images at different scales and corresponding cross-sections of chess-board PS micropattern prepared by capillary transfer lithography on LbL film.

We obtained similar results for different spacings and more complex shapes of PDMS molds. We prepared PS micropatterns using PDMS mold containing the chess-board pattern with 430 nm distance from corner to corner and 1 μm distance from side to side of square surface areas (Figure 7.6). The optical image in Figure 7.6a shows a very uniform PS micropattern complementary to the PDMS mold over large surface areas. AFM image in Figure 7.6b illustrates that the spacings in PDMS mold has been successfully replicated by the PS micropattern. This kind of well-defined 3D polymer microstructure with sharp boundaries was not easily achievable by using conventional microcontact printing on the LbL surfaces. The subsequent formation of gold nanoparticle arrays on these surfaces clearly showed that the original chess-board pattern has been replicated with good accuracy (Figure 7.7). Importantly, the edge sharpness

remained high (below 50 nm), and the regular and alternating rectangular shapes were faithfully transferred from the original features of the PDMS mold.

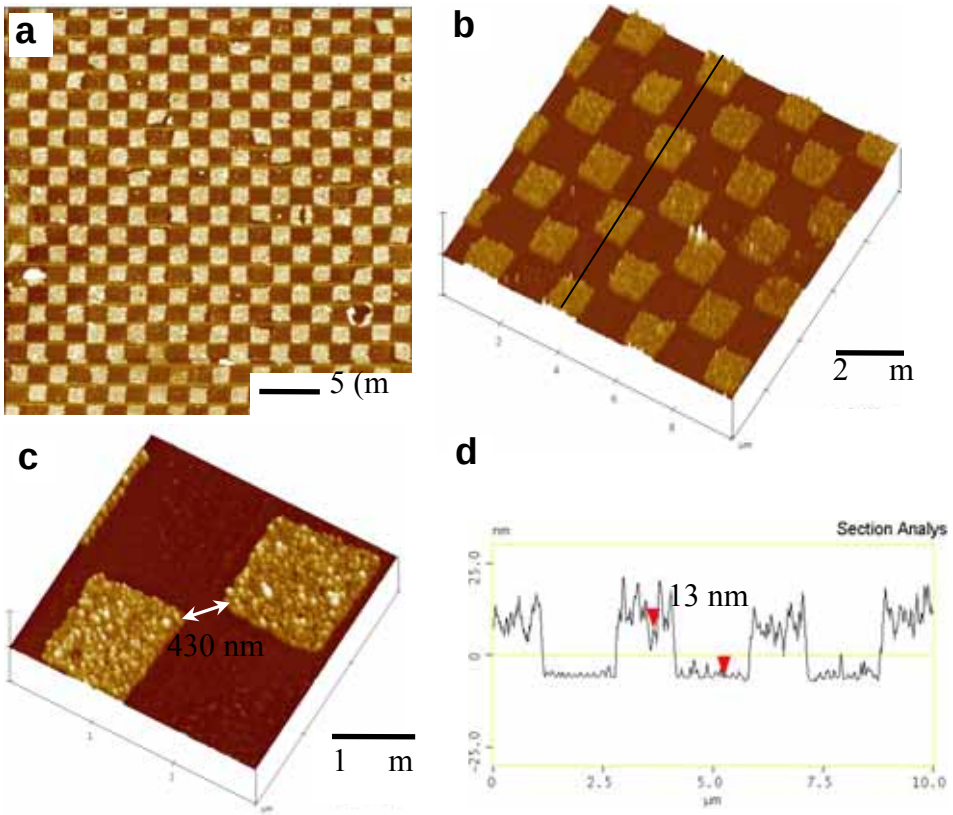

Figure 7.7. Topographical images at different scales (a-c) and corresponding cross-section for the chess-board array of gold nanoparticles (d).

Another application in which CTL printing has proven useful was the preparation of hierarchical multi-component arrays by multistep CTL printing (Figure 7.8). The PS sacrificial template allowed for the sequential formation of two different microarrays on the intact surface areas of LbL film. We sequentially applied two different PDMS molds for the formation of the gold nanoparticle stripe pattern with 3 μm spacing as a first layer followed by the formation of the carbon nanotube pattern with 10 μm spacing oriented perpendicularly to the gold nanoparticle stripes (Figure 7.8c). Figure 7.8c shows AFM

image of a large area of well-defined crossed stripes with each wide stripe containing gold nanoparticles and each perpendicular thinner and less visible stripe containing carbon nanotubes (Figure 7.8d). This demonstrates that the PS protected LbL surface areas were intact after removal of PS and can be further modified. We observed that no carbon nanotubes appeared on the surface of gold nanoparticle areas whereas they are both have strong interaction with intact PAH surface.

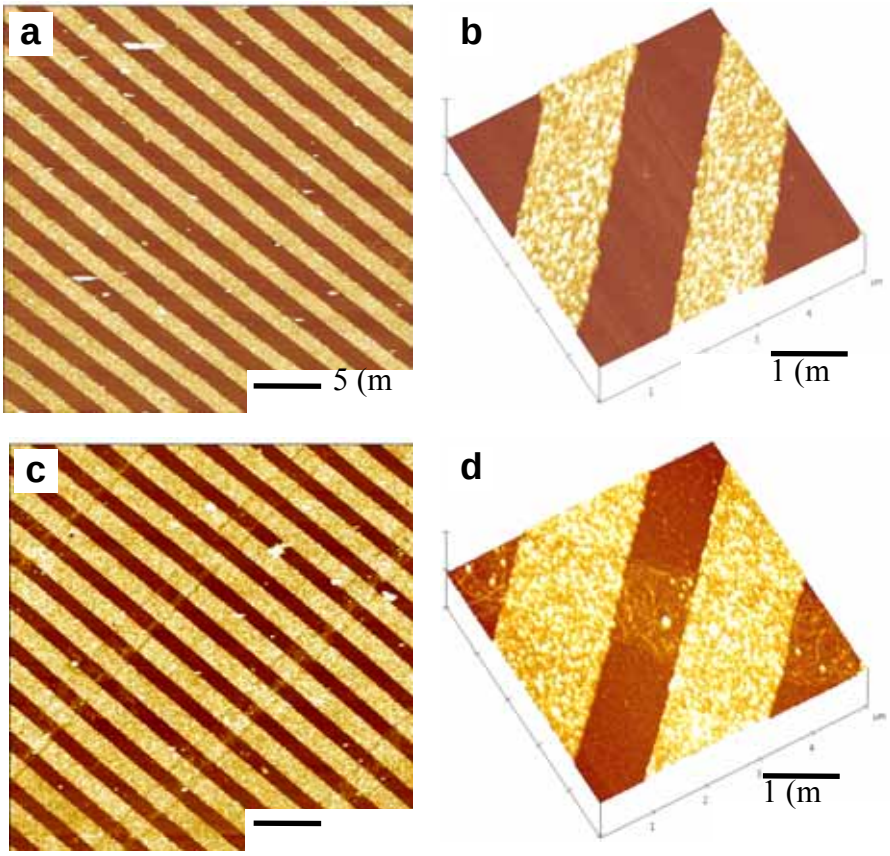

Figure 7.8. Topographical images of patterned gold nanoparticle array before (a, b) and after (c, d) sequential deposition of orthogonal carbon nanotube array (weaker stripes with larger spacing oriented perpendicularly to initial stripes).

7.3.3. Formation of Encapsulated Patterned Arrays

The intact polyelectrolyte surface, which was originally covered by the sacrificial PS template was further used for encapsulating nanoparticulate arrays into LbL multilayers as shown in Figure 7.9. To demonstrate the feasibility of this approach for the encapsulation of the nanoparticle arrays into LbL multilayers, we further deposited 9 bilayers of PAH/PSS on top of the patterned arrays formed by both gold nanoparticles and carbon nanotubes (see Figure 7.5 for their surface morphology).

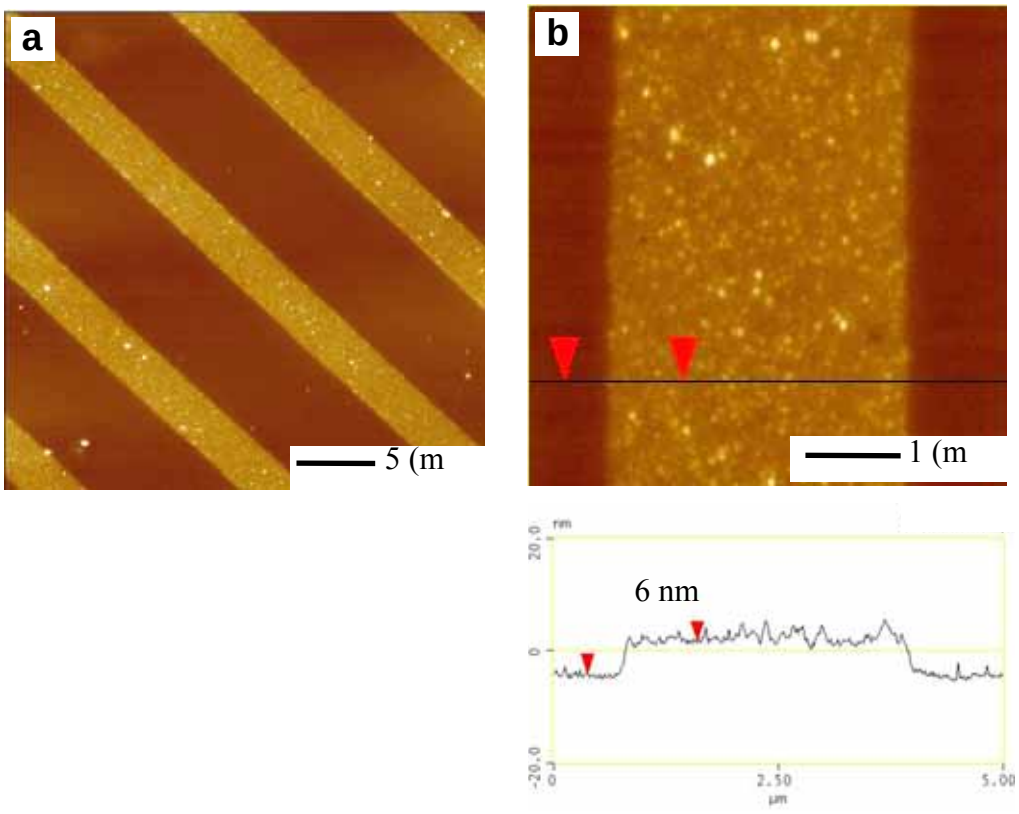

Figure 7.9. Topographical images at different scales (a, b) and corresponding cross-section of the gold nanoparticle array encapsulated into LbL film.

Figure 7.9 shows AFM topographical images of gold nanoparticle arrays encapsulated between two LbL multilayers. Well-defined stripes of the encapsulated

gold nanoparticles are clearly visible on a large scale even after coverage with relatively thick LbL multilayers (19 nm). High contrast is similar to that observed for open array (Figure 7.5). However, the high-resolution AFM image shows relatively densely filled surface areas along the stripes and fuzzy boundaries, a significant difference from the initial gold nanoparticle array (Figure 7.9). Cross-section of these areas shows modest peak-to-value height variation indicating deposition of the topmost LbL film in a conformal manner by filling open space between nanoparticles (surface coverage below 50%). This filling resulted in effective reduction of the apparent elevation of the gold nanoparticle areas from original 13 nm (Figure 7.5b) to 6 nm (Figure 7.9a).

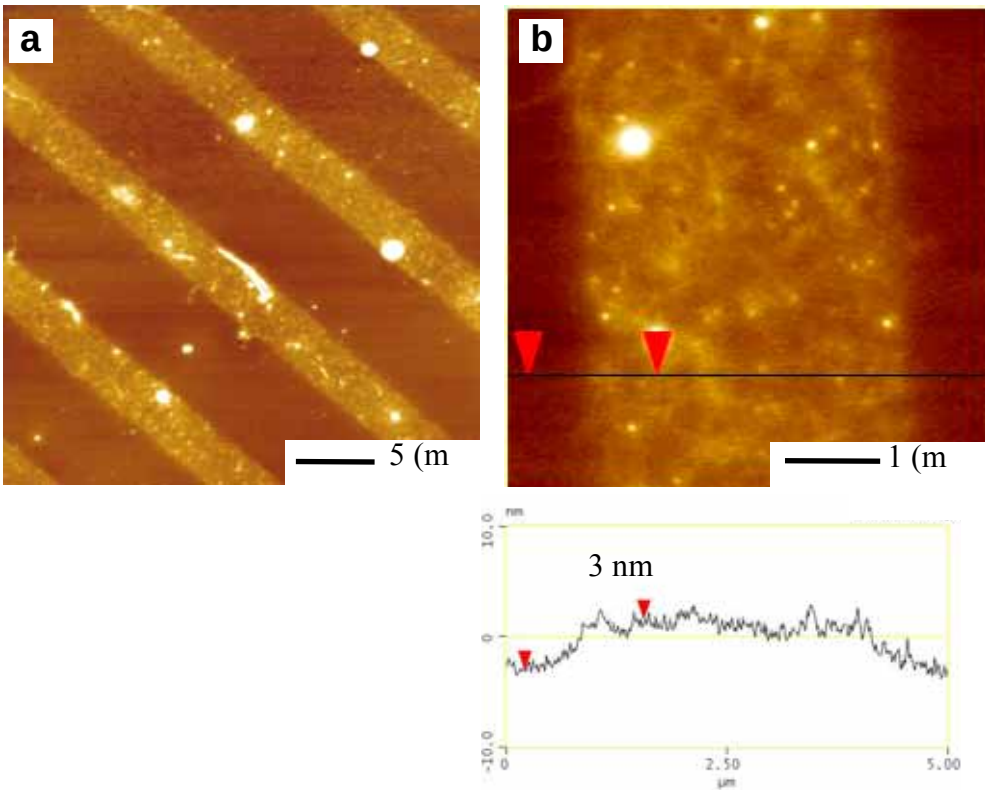

Figure 7.10. Topographical images at different scales (a, b) and corresponding cross-section of the carbon nanotube array encapsulated into LbL film.

Uniform coverage with the topmost LbL multilayer was achieved for carbon nanotube arrays as well. At medium resolution, we still easily observed parallel stripes of carbon nanotube arrays (Figure 7.10). However, at higher resolution, the original surface morphology of carbon nanotube arrays (Figure 7.5d) appeared smeared due to the coverage with the topmost LbL multilayered film (Figure 7.10). Details of carbon nanotube bundle packing within these areas became poorly visible. AFM cross-section showed the decrease of the height differences from initial 5–6 nm to 2-3 nm (Figure 7.10).

7.4. References

[1] Hammond, P. T. *Adv. Mater.* **2004**, *16*, 1271.

[2] Tsukruk, V. V. *Prog. Polym. Sci.* **1997**, *22*, 247.

[3] Hiller, J.; Mendelsohn, J. D.; Rubner, M. F. *Nat. Mater.* **2002**, *1*, 59.

[4] Jiang, C.; Markutsya, S.; Pikus, Y.; Tsukruk, V. V. *Nat. Mater.* **2004**, *3*, 721.

[5] Decher, G. *Science* **1997**, *277*, 1232.

[6] Decher, G.; Schlenoff, J. B. (Eds) *Multilayer Thin Films*; Wiley-VCH: Weinheim, 2003.

[7] Kotov, N. A.; Dekany, I.; Fendler, J. H. *Adv. Mater.* **1996**, *8*, 637.

[8] Zheng, H. P.; Lee, I.; Rubner, M. F.; Hammond, P. T. *Adv. Mater.* **2002**, *14*, 569.

[9] Lvov, Yu.; Möhwald, H. (Eds) *Protein Architecture: Interfacial Molecular Assembly and Immobilization Biotechnology*; Marcel Dekker: New York, 2000.

[10] Lvov, Y.; Ariga, K.; Onda, M.; Ichinose, I.; Kunitake, T. *Langmuir* **1997**, *13*, 6195.

[11] Koktysh, D. S.; Liang, X. R.; Yun, B. G.; Pastoriza-Santos, I.; Matts, R. L.; Giersig, M.; Serra-Rodriguez, C.; Liz-Marzan, L. M.; Kotov, N. A. *Adv. Funct. Mater.* **2002**, *12*, 255.

[12] Mamedov, A. A.; Belov, A.; Giersig, M.; Mamedova, N. N.; Kotov, N. A. *J. Am. Chem. Soc.* **2001**, *123*, 7738.

[13] Crisp, M. T.; Kotov, N. A. *Nano Lett.* **2003**, *3*, 173.

[14] Mamedov, A. A.; Kotov, N. A.; Prato, M.; Guldi, D. M.; Wicksted, J. P.; Hirsch, A. *Nat. Mater.* **2002**, *1*, 190.

[15] Jiang, X.; Hammond, P. T. *Langmuir* **2000**, *16*, 8501.

[16] Jiang, X.; Zheng, H.; Gourdin, S.; Hammond, P. T. *Langmuir* **2002,** *18*, 2607.

[17] Zheng, H.; Lee, I.; Rubner, M. F.; Hammond, P. T. *Adv. Mater.* **2002**, *14*, 569.

[18] Lee, I.; Zheng, H.; Rubner, M. F.; Hammond, P. T, *Adv. Mater.* **2002**, *14*, 572.

[19] Kidambi, S.; Lee, I.; Chan, C. J. Am. Chem. Soc. **2004**, *126*, 16286.

[20] Berg, M. C.; Yang, S. Y.; Hammond, P. T.; Rubner, M. F. *Langmuir* **2004**, *20*, 1362.

[21] Jaffar, S.; Nam, K. T.; Khademhosseini, A.; Xing, J.; Langer, R. S.; Belcher, A. M. *Nano Lett.* **2004**, *4*, 1421.

[22] Tokuhisa, H.; Hammond, P. T. *Langmuir* **2004**, *20*, 1436.

[23] Tsukruk, V. V.; Ko, H.; Peleshanko, S. *Phys. Rev. Lett.* **2004**, *92*. 065502.

[24] Ko, H.; Peleshanko, S.; Tsukruk, V. V. *J. Phys. Chem. B* **2004**, *108*, 4385.

[25] Tsukruk, V. V.; Bliznyuk, V. N.; Visser, D. W.; Campbell, A. L.; Bunning, T.; Adams, W. W. *Macromolecules,* **1997***, 30,* 6615.

[26] Park, J.; Hammond, P. T. *Adv. Mater.* **2004**, *16*, 520.

[27] Kohli, N.; Worden, R. M.; Lee, I. *Chem. Commun.* **2005**, 316.

[28] Hua, F.; Cui, T.; Lvov, Y. M. *Nano Lett.* **2004**, *4*, 823.

[29] Zhou, D.; Bruckbauer, A.; Abell, C.; Klenerman, D.; Kang, D.-J. *Adv. Mater*. **2005**. ASAP.

[30] Madou, M. *Fundamentals of Microfabrication*; CRC Press: New York, 1997.

[31] Kim, Y. S.; Lee, H. H. *Adv. Mater.* **2003**, *15*, 332.

[32] Xia, Y. N.; Whitesides, G. M. *Angew. Chem. Int. Ed.* **1998**, *37*, 551.

[33] Geissler, M.; Xia, Y. N. *Adv. Mater.* **2004**, *16*, 1249.

[34] Gates, B. D.; Xu, Q. B.; Love, J. C.; Wolfe, D. B.; Whitesides, G. M. *Annu. Rev. Mater.*

Res. **2004**, *34*, 339.

[35] Gates, B.; Xu, Q.; Stewart, M.; Ryan, D.; Willson, C. G.; Whitesides, G. M. *Chem. Rev.* **2005**, *105*, 1171.

[36] Li, H. W.; Muir, B. V. O.; Fichet, G.; Huck, W. T. S. *Langmuir* **2003**, *19*, 1963.

[37] Chou, S. Y.; Krauss, P. R.; Renstrom, P. J. *Appl. Phys. Lett.* **1995**, *67*, 3114.

[38] Chou, S. Y.; Krauss, P. R.; Renstrom, P. J. *Science* **1996**, *272*, 85.

[39] Zhao, X. M.; Xia, Y. N.; Whitesides, G. M. *Adv. Mater.* **1996**, *8*, 837.

[40] Kim, E.; Xia, Y. N.; Whitesides, G. M. *Nature* **1995**, *376*, 581.

[41] Beh, W. S.; Kim, I. T.; Qin, D.; Xia, Y. N.; Whitesides, G. M. *Adv. Mater.* **1999**, *11*, 1038.

[42] Kim, E.; Xia, Y. N.; Zhao, X. M.; Whitesides, G. M. *Adv. Mater.* **1997**, *9*, 651.

[43] Suh, K. Y.; Kim, Y. S.; Lee, H. H. *Adv. Mater.* **2001**, *13*, 1386.

[44] Khademhosseini, A.; Jon, S.; Suh, K. Y.; Tran, T. N. T.; Eng, G.; Yeh, J.; Seong, J.; Langer, R. *Adv. Mater.* **2003**, *15*, 1995.

[45] Wang, M. T.; Braun, H. G.; Kratzmuller, T.; Meyer, E. *Adv. Mater.* **2001**, *13*, 1312.

[46] Jiang, C.; Markutsya, S.; Tsukruk, V. V. *Adv. Mater.* **2004**, *16*, 157.

[47] Bruinink, C. M.; Peter, M.; de Boer, M.; Kuipers, L.; Huskens, J.; Reinhoudt, D. N. *Adv. Mater.* **2004**, *16*, 1086.

[48] Meitl, M. A.; Zhou, Y. X.; Gaur, A.; Jeon, S.; Usrey, M. L.; Strano, M. S.; Rogers, J. A. *Nano Lett.* **2004**, *4*, 1643.

[49] McDonald, J. C.; Whitesides, G. M. *Acc.Chem. Res.* **2002**, *35*, 491.

[50] Lee, J. N.; Park, C.; Whitesides, G. M. *Anal. Chem.* **2003**, *75*, 6544.

Chapter 8. Gold Nanoparticle-Decorated Nanocanal Arrays for Surface Enhanced Raman Scattering

8.1. Introduction

Robust and reliable chemical sensing materials with improved sensitivity and selectivity are in high demand for the detection of hazardous chemical and biological materials. Sensors based upon surface-enhanced Raman scattering (SERS) phenomenon are considered as prospective tools because of fast detection, characteristic "fingerprint" signature of analytes along with the availability of portable systems for field analysis.[1] In SERS phenomenon, the enormous Raman enhancement arises on the localized spots ("hot spots") in metallic nanostructures due to the strong local electromagnetic fields associated with the surface plasmon resonances of metal nanostructures.[2,3,4] SERS on colloidal metal aggregates[5,6] and resonance Raman have been utilized for trace detection of explosives,[7,8] chemical and biological warfare agents,[9] internal mechanical stresses [10,11,12] and toxic environmental pollutants.[13] However, an outstanding challenge of SERS-based detection is the lack of robust and facile fabrication routine for SERS substrates with huge enhancement. Traditionally, electrochemically roughened metal surfaces,[14] metal colloids,[15] metal island films[16,17,18], metal nanowires, [19,20] periodic arrays of metal nanostructures,[21,22,23] and self-assembled metal nanoparticles,[24,25] are employed as SERS-active substrates. However, the stability of suspended metal nanoparticles is the main obstacle and the sensitivity of two-dimensional (2D) metal structures remains modest due to a limited number of hot spots available within laser-activated footprint.

Thus, 3D porous structures have been suggested as active SERS substrates with the advantage of large surface area available for the formation of hot spots and the adsorption of target analyte. Consequently, SERS substrates have been fabricated by depositing Au or Ag films on porous silicon,[26,27] GaN,[28] and filter paper.[29] Alternatively, deposition of metal nanoparticles on the porous aluminum membranes[30], colloidal crystal templates[31,32] , or 1D microwires[33] have been exploited. However, most of these studies have not been fully utilized the 3D structures for SERS effects mainly because of limited light propagation through the porous materials. For example, the extraordinary light transmission of metallic porous arrays can be used for further enhancement of light interaction with hot spots and thus SERS spectra.[34] Indeed, the nanopores in gold films have been proven to show enhanced Raman scattering due to intense electromagnetic fields generated by the surface plasmons.[35,36] The use of dielectric materials such as porous alumina membranes will be also interesting with respect to efficient light interaction with SERS media because of the optical transparency and waveguide properties.[37,38]

Here, we introduce nanocanal array decorated with metal nanoparticles as robust and facile SERS substrate with high Raman intensity. These substrates are successfully employed here for the trace detection of 2,4-dinitrotoluene (2,4-DNT), a model nitroaromatic compound for trinitrotoluene-based explosives.[39] Figure 8.1 shows a schematic of fabrication procedures for nanocanal array decorated with gold nanoparticles via polyelectrolyte monolayers (see Experimental).

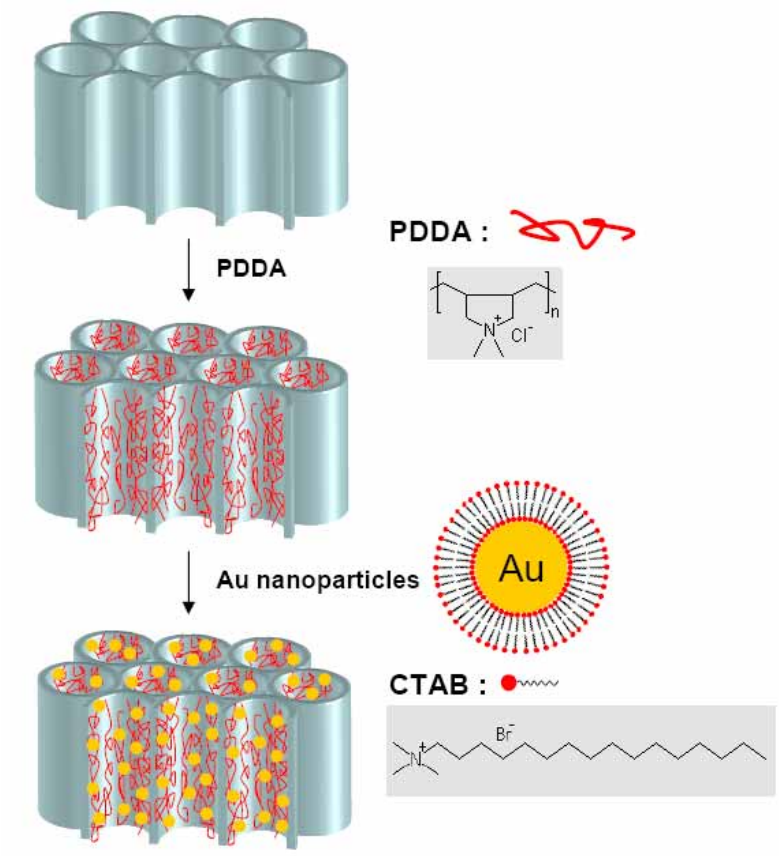

Figure 8.1. Schematic of fabrication procedures for nano-hole arrays decorated with gold nanoparticles. Porous alumina membranes are functionalized with positively charged amine-groups by modification with PDDA. CTAB-capped gold colloids are then passed through the PDDA-modified porous alumina membranes resulting in Au nanoparticle immobilization.

8.2. Sample Preparations

Porous alumina membranes were purchased from Whatman (Anodisc 47) and the average pore size was 243±20 nm (measured from SEM images) with 60 μm thickness. The immobilization of Au nanoparticles on porous alumina membranes was done by modified literature procedure.[40,41] Typically, inner surface of porous membranes were modified with PDDA (M_w=60,000, Aldrich) by spin-coating (4000 rpm, 30 sec) of 0.2% aqueous solution followed by rinsing with Nanopure water (18 MΩ cm). The excess amounts of CTAB surfactant in the Au colloid solution was removed by repeated

centrifugation and multi-step dilution. The immobilization of Au nanoparticles was done by the filtration of this solution through PDDA-modified membrane on top of polycarbonate membrane filters (0.4 μm pore diameter) followed by filtration of copious amount of Nanopure water to rinse surfactant away. To increase the adsorption of DNT on the Au surface, additional PDDA was used to cover gold nanoparticles. Finally the prepared samples were then attached on the silicon substrates by using epoxy glue and 10 μl of 2,4-dinitrotoluene (2,4-DNT, Aldrich) solution in ethanol was drop-evaporated on SERS substrate with area of 1 cm^2.

A field-emission scanning electron microscopy (FESEM, LEO 1530) was used to investigate the assembled structures of decorated membranes. The Raman spectra of DNT on SERS substrates were recorded with a Holoprobe Raman microscope (Hololab series 5000 spectrometer, Kaiser Optical Systems, Inc) with back-scattered configuration using a 10× objective lens. The excitation laser is diode laser with 785 nm wavelength and the power is 20 mW to the sample. The collection time is 20 sec with no accumulation and three points were averaged for each sample.

8.3. Results and Discussion

The representative cross-sectional scanning electron microscope (SEM) image of decorated nanocanals (240 nm diameter) within porous alumina membranes shows that most of the gold nanoparticles (32 nm) are immobilized in an isolated state with occasional aggregated clusters inside the pore walls modified with poly(diallyldimethylammonium chloride) (PDDA) polyelectrolyte (Figure 8.2a). The

immobilized nanoparticles inside the pores can be also observed from the SEM image obtained with tilt angle (Figure 8.2b). The energy dispersive spectroscopy (EDS) confirmed the presence of gold nanoparticles immobilized inside the through nanocanals (Figure 8.2a). Few nanoparticles have been observed on the outer surface of nano-hole arrays as compared to the nanoparticle immobilization inside the pore walls. Immobilization inside the PDDA-modified pores can be related to partial replacement of the cetyltrimethylammonium bromide (CTAB) ligands with amine functional groups of PDDA layer (see Figure 8.1 for chemical structures).

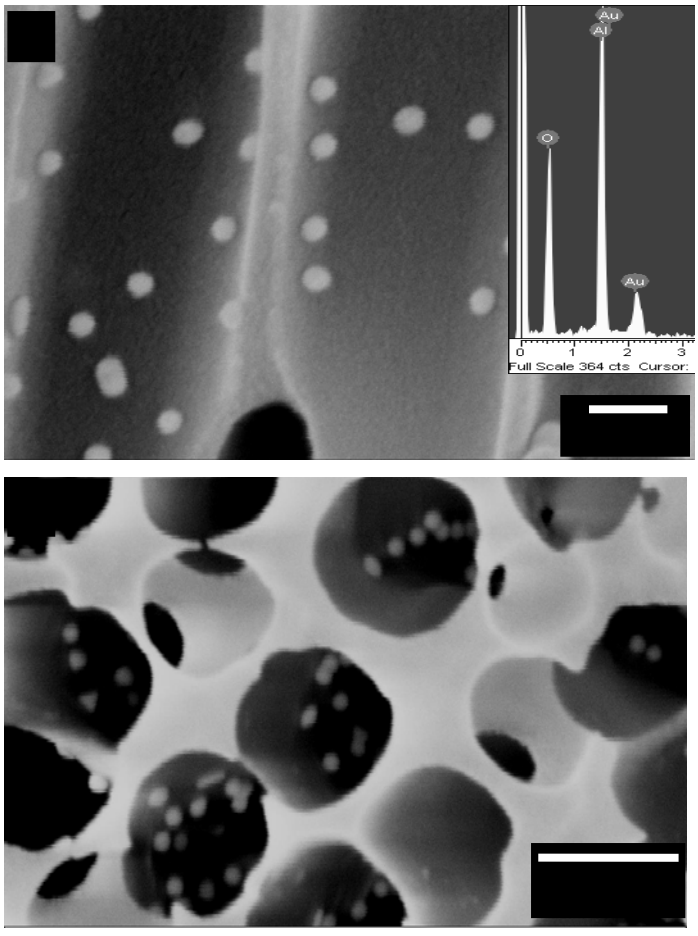

Figure 8.2. Cross-sectional (a) and angle-view (b) SEM images of porous alumina membranes decorated with Au nanoparticles. The inset in (a) shows EDS spectrum indicating the presence of Au inside the pore walls.

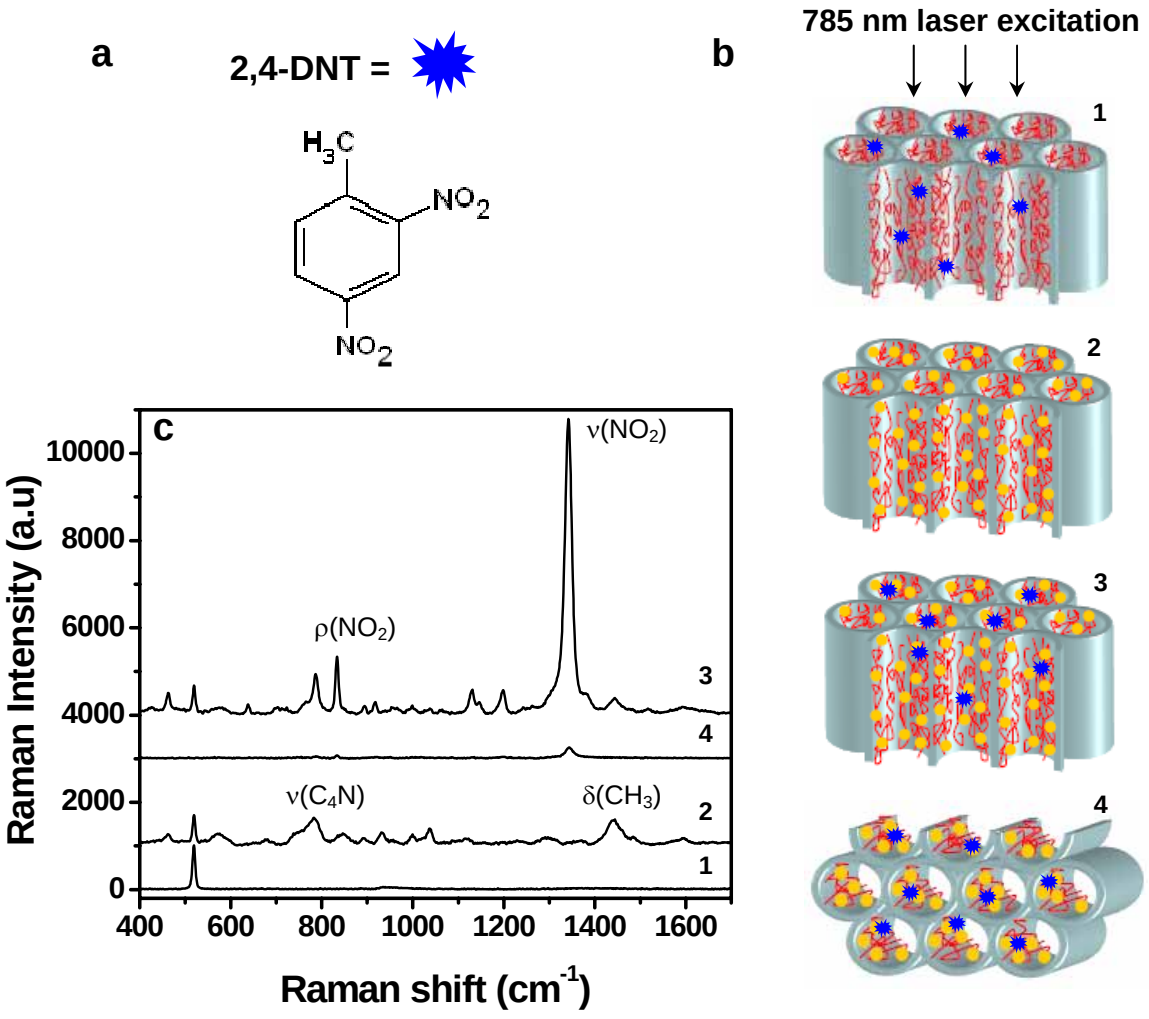

Figure 8.3. (a) Chemical structure of 2,4-DNT. (b) Schematic of Raman measurement of 2,4-DNT with different configurations and light incidences to the SERS substrates. The excitation light incidence is parallel (1,2,3) and perpendicular (4) to the pore axes. (c) Raman spectrum of 1000 ppm 2,4-DNT on each substrate shown schematically in (b). 10 μl of 2,4-DNT solution in ethanol was drop-evaporated on the 1 cm^2 area substrates.

PDDA polyelectrolyte used here can act as a selective coating to increase the adsorption of DNT on the gold nanoparticle surface due to the interactions between the electron-donating amine-groups in PDDA and electron-deficient NO_2 groups in 2,4-DNT.[42] A control Raman experiment of 2,4-DNT adsorbed on PDDA-modified porous membrane (case 1, Figure 8.3b) provides no measurable signals (spectrum 1, Figure 8.3c).

In this study, we used a near-IR laser (785 nm) as the excitation source because its wavelength is close to the expected coupled surface plasmon resonance[43] and the higher transmission through the aluminum membrane. It is worth to note that our attempts to use 514 nm wavelength showed extremely low intensity due to high absorption similarly to that reported in the literature.[44]

A strong silicon peak at 520 cm^{-1} arises from the supporting silicon substrate indicating that the excitation light passes through whole thickness (60 μm) of the membrane and reflects back traveling via vertically aligned nanocanals (Figure 8.1c). Adding gold nanoparticles activates the SERS phenomenon for PDDA layer (case 2, Figure 8.3b), revealing their characteristic Raman signatures: C_4N stretching modes (ν_{C4N}) at 783 cm^{-1} and CH_3 asymmetric bending modes (ρ_{CH3}) at 1444 cm^{-1} (spectrum 2, Figure 8.3c).[45]

Deposition of 2,4-DNT analyte via drop-casting routine (case 3, Figure 8.3b) dramatically changes the SERS spectra with two intense peaks corresponding to two representative 2,4-DNT vibration modes: NO_2 out-of-plane bending modes (ρ_{NO2}) at 834 cm^{-1} and NO_2 stretching modes (ν_{NO2}) at 1342 cm^{-1} (spectrum 3, Figure 8.3c). Moreover, silicon peak is still strong indicating reflection of the laser beam after passing through the modified nanocanals. Indeed, considering the initial diameter of nanocanals to be 240 nm and the thickness of polyelectrolyte layer with immobilized nanoparticles on both walls does not exceed 70 nm, we can conclude that the light passes through vertical nanocanals without much absorption. The critical importance of the ability of the laser

beam to pass whole membrane thickness is illustrated by the tremendous reduction of the Raman signal when the light is directed in transversal direction (case 4, Figure 8.3b). Only very weak ν_{NO2} mode at 1342 cm^{-1} is observed under this orientation with silicon band disappearing completely (spectrum 4, Figure 8.3c). Apparently, the optical loss across walls is tremendous and attenuates the laser beam to reduce the overall effect to a trivial case of active topmost layer with few transversal nanocanals involved.

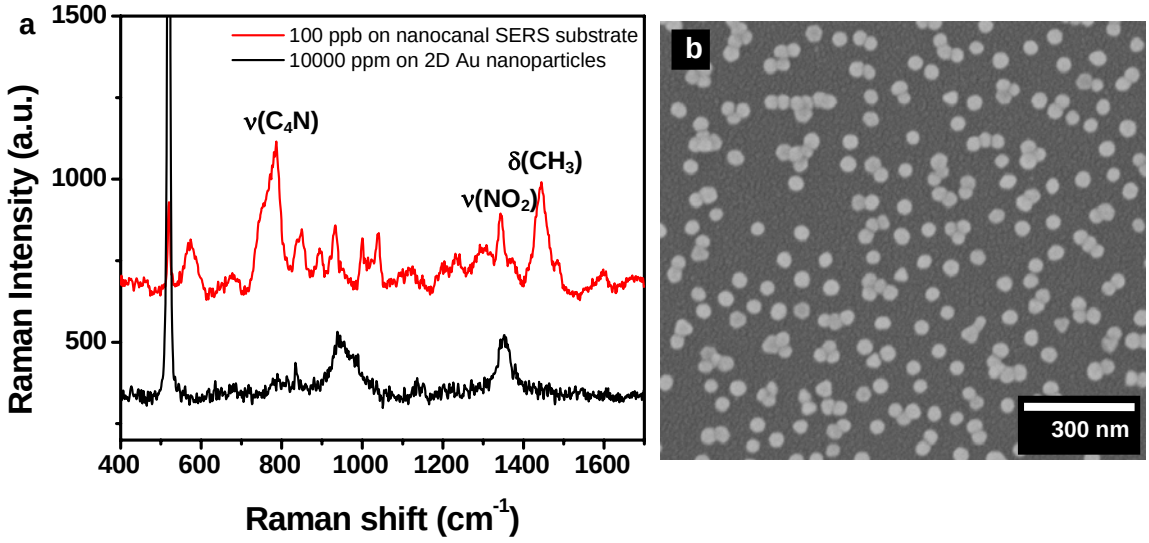

Figure 8.4. (a) Raman spectra of 100 ppb 2,4-DNT drop-evaporated on the SERS substrates with PDDA/Au nanopaticles/PDDA/PAM on top of silicon substrates and control Raman spectra of 10000 ppm 2,4-DNT on 2D gold nanoparticle substrate. (b) SEM image of 2D gold nanoparticle substrate.

Much higher Raman enhancement from vertically oriented nanocanals (case 3, Figure 8.3b) allows for trace level detection of DNT (Figure 8.4a). The Raman spectrum of 100 ppb 2,4-DNT solution (10µl) evaporated on SERS substrate clearly shows NO_2 stretching modes of DNT at 1342 cm^{-1} distinctive from several PDDA related Raman peaks such as ν_{C4N} at 783 cm^{-1} and ρ_{CH3} at 1444 cm^{-1}. The minimum detection limit for our current measurement conditions (20 sec acquisition time, 20 mW laser power, 10 µl

of DNT solution drop-evaporated uniformly on 1cm^2 substrates) estimated from signal-to-noise ratio (S/N ratio of 15) for this spectrum can be as low as 10 fg which corresponds to 3x10^7 molecules located within nanocanals. This detection limit is three orders of magnitude better than typical values of 1–10 pg of 2,4-DNT detectable with highly oriented silver nanowire films and roughened gold substrate.[46]

The estimation of Raman enhancement factor (EF) has been conducted by using a reference sample without SERS contribution: EF= $I_{SERS}/I_{Ref}\times[reference]/[sample]$,[47,48] where I_{SERS} and I_{Ref} are Raman intensities at certain Raman spectra and [SERS] and [reference] are the concentrations of target molecules in the SERS and reference samples, respectively. By comparing the peak intensity at characteristic band at 1342 cm^{-1} with normal Raman peak of reference 2,4-DNT film of the known thickness, we estimate the SERS enhancement factor to be about 1.1×10^6. This unexpectedly high SERS enhancement can not be caused by the trivial increase in specific surface area. A control Raman study on 2D gold nanoparticle array with similar nanoparticle surface density has been conducted to evaluate this contribution (Figure 8.4b). The Raman spectrum of 10000 ppm 2,4-DNT solution showed only weak and broad NO_2 stretching modes of DNT at 1342 cm^{-1} (Figure 8.4a). From the Raman peak intensities, we estimate that the SERS enhancement of the 3D nanocanal array is about five orders of magnitude higher than that observed on gold nanoparticle monolayer which is three orders of magnitude higher than that expected for increase in geometrical surface area.

The excessive Raman enhancement at first glance can be associated with the effect of resonance coupling between neighboring nanoparticles localized on inner walls of nanocanals (hot spots). However, the estimation of the average distance between gold nanoparticles does not support this suggestion. In fact, the value obtained is close to 100 nm or distance/diameter ratio, d/D of about 3, well above the value (ratio of about 1.5D) suggested for maximum enhancement.[49,50,51] Thus, at given interparticulate distances, no traditional hot spots are presented in the system.

Thus considering the geometry of the nanocanals array and minor contributions from specific surface area and traditional hot spots, we suggest that the optical waveguide effect of vertical alumina-pore arrays with excited evanescent electrical field is responsible for the observed enhancement of Raman scattering. As known, the propagating light can be trapped inside the alumina nanowalls with total internal reflection caused by high refractive index difference between alumina (n~1.6) and air/polymer monolayer (n = 1 and 1.5). This multiple reflection can leads to higher photon density of states at the alumina-inner coating interface,[52] resulting in increased probability of Raman scattering via interaction between the evanescent field and the gold nanoparticles tethered to the inner surface of nanocanals. This Raman enhancement resembles optical microcavities with micrometer-sized cylindrical or spherical resonators.[53,54] and nanoribbon waveguides with tethered nanoparticles.[55] In these systems, additional optical gains of more than two to five orders of magnitude have been acquired through microcavity resonances. However, the waveguide effect of nanoporous alumina membranes is advantageous compared to those microcavity systems due to large surface

area and efficient guiding the incident and scattered light through inhibition of light propagation in the x-y plane. Moreover, we speculate that coupling of this phenomenon with traditional hot-spot design, the enhancement factor can be increased by several orders of magnitude and approach limits of robust facile detection of few molecules, a venue open only for few resonance-enhanced Raman detection under point-short detection conditions.[9] The combination of high specific surface area with hot spots and optical wave-guiding properties will open a new framework for the design of robust, field-friendly, ultra-sensitive SERS-based sensors for the trace-level or even single molecule detection of non-resonant chemicals and biomolecules.

8.4. References

[1] Baker, G. A.; Moore, D. S. *Anal. Bioanal. Chem.* **2005**, *382*, 1751.

[2] Kneipp, K.; Kneipp, H.; Itzkan, I.; Dasari, R. R.; Feld, M. S. *Chem. Rev.* **1999**, *99*, 2957.

[3] Genov, D. A.; Sarychev, A. K.; Shalaev, V. M.; Wei, A. *Nano Lett.* **2004**, *4*, 153.

[4] Imura, K.; Okamoto, H.; Hossain, M. K.; Kitajima, M. *Nano Lett.* **2006**, *6*, 2173.

[5] Nie, S. M.; Emery, S. R. *Science* **1997**, *275*, 1102.

[6] Kneipp, K.; Wang, Y.; Kneipp, H.; Perelman, L. T.; Itzkan, I.; Dasari, R.; Feld, M. S. *Phys Rev Lett* **1997**, *78*, 1667.

[7] Sylvia, J. M.; Janni, J. A.; Klein, J. D.; Spencer, K. M. *Anal Chem* **2000**, *72*, 5834.

[8] Tao, A.; Kim, F.; Hess, C.; Goldberger, J.; He, R. R.; Sun, Y. G.; Xia, Y. N.; Yang, P. D. *Nano Lett* **2003**, *3*, 1229.

[9] Haynes, C. L.; Yonzon, C. R.; Zhang, X. Y.; Van Duyne, R. P. *J Raman Spectrosc* **2005**, *36*, 471.

[10] Jiang, C. Y.; Lio, W. Y.; Tsukruk, V. V. *Phys Rev Lett* **2005**, *95*, 115503.

[11] Jiang, C. Y.; Ko, H. Y.; Tsukruk, V. V. *Adv Mater* **2005**, *17*, 2127.

[12] Ko, H. H.; Pikus, Y.; Jiang, C. Y.; Jauss, A.; Hollricher, O.; Tsukruk, V. V. *Appl Phys Lett* **2004**, *85*, 2598.

[13] Olson, L. G.; Uibel, R. H.; Harris, J. M. *Appl. Spectrosc.* **2004**, *58*, 1394.

[14] Fleischmann, M.; Hendra, P. J.; McQuillan, A. J. *Chem. Phys. Lett.* **1974**, *26*, 163.

[15] Torres, E. L.; Winefordner, J. D. *Anal. Chem.* **1987**, *59*, 1626.

[16] Freeman, R. G.; Grabar, K. C.; Allison, K. J.; Bright, R. M.; Davis, J. A.; Guthrie, A. P.; Hommer, M. B.; Jackson, M. A.; Smith, P. C.; Walter, D. G.; Natan, M. J. *Science* **1995**, *267*, 1629.

[17] Wang, Z. J.; Pan, S. L.; Krauss, T. D.; Du, H.; Rothberg, L. *Proc. Natl. Acad. Sci. USA* **2003**, *100*, 8638.

[18] Nikoobakht, B.; El-Sayed, M. A. *J. Phys. Chem. A* **2003**, *107*, 3372.

[19] Lee, S. J.; Morrill, A. R.; Moskovits, M. *J. Am. Chem. Soc.* **2006**, *128*, 2200.

[20] Schierhorn, M.; Lee, S. J.; Boettcher, S. W.; Stucky, G. D.; Moskovits, M. *Adv. Mater.* **2006**, *18*, 2829.

[21] Jensen, T. R.; Schatz, G. C.; Van Duyne, R. P. *J Phys Chem B* **1999**, *103*, 2394.

[22] Haynes, C. L.; Van Duyne, R. P. *J Phys Chem B* **2003**, *107*, 7426.

[23] Felidj, N.; Aubard, J.; Levi, G.; Krenn, J. R.; Hohenau, A.; Schider, G.; Leitner, A.; Aussenegg, F. R. Appl. Phys. Lett. **2003**, *82,* 3095.

[24] Wang, H.; Levin, C. S.; Halas, N. J. *J Am Chem Soc* **2005**, *127*, 14992.

[25] Qiu, T.; Wu, X. L.; Shen, J. C.; Chu, P. K. *Appl. Phys. Lett.* **2006**, *89*, 131914.

[26] Chan, S.; Kwon, S.; Koo, T. W.; Lee, L. P.; Berlin, A. A. *Adv. Mater.* **2003**, *15*, 1595.

[27] Lin, H. H.; Mock, J.; Smith, D.; Gao, T.; Sailor, M. J. *J Phys Chem B* **2004**, *108*, 11654.

[28] Williamson, T. L.; Guo, X. Y.; Zukoski, A.; Sood, A.; Diaz, D. J.; Bohn, P. W. *J. Phys. Chem. B* **2005**, *109*, 20186.

[29] Laserna, J. J.; Sutherland, W. S.; Winefordner, J. D. *Analytica Chimica Acta* **1990**, *237*, 439.

[30] Sutherland, W. S; Winefordner, J. D. *J. Colloid Interf. Sci.* **1992**, *148*, 129.

[31] Tessier, P. M.; Velev, O. D.; Kalambur, A. T.; Rabolt, J. F.; Lenhoff, A. M.; Kaler, E. W. *J. Am. Chem. Soc.* **2000**, *122*, 9554.

[32] Lu, L. H.; Eychmuller, A.; Kobayashi, A.; Hirano, Y.; Yoshida, K.; Kikkawa, Y.; Tawa, K.; Ozaki, Y. *Langmuir* **2006**, *22*, 2605.

[33] Qin, L. ; Zhou, S. ; Xue, C. ; Atkinson, A. ; Schatz, G. C.; Mirkin, C. A. *Proc. Natl. Acad. Sci. USA*, **2006**, *103*, 13300.

[34] Ebbesen, T. W.; Lezec, H. J.; Ghaemi, H. F.; Thio, T.; Wolff, P. A. *Nature* **1998**, *391*, 667.

[35] Brolo, A. G.; Arctander, E.; Gordon, R.; Leathem, B.; Kavanagh, K. L. *Nano Lett* **2004**, *4*, 2015.

[36] Bahns, J. T.; Yan, F. N.; Qiu, D. L.; Wang, R.; Chen, L. H. *Appl. Spectroscopy* **2006**, *60*, 989.

[37] Saito, M.; Shibasaki, M.; Nakamura, S.; Miyagiet, M. *Opt. Lett.* **1994**, *19*, 710.

[38] Lau, K. H. A.; Tan, L. S.; Tamada, K.; Sander, M. S.; Knoll, W. *J. Phys. Chem. B* **2004**, *108*, 10812.

[39] Moore, D. S. Rev. *Sci. Instrum.* **2004**, *75*, 2499.

[40] Lahav, M.; Sehayek, T.; Vaskevich, A.; Rubinstein, I. *Angew. Chem. Int. Edit.* **2003**, *42*, 5575.

[41] Dotzauer, D. M.; Dai, J. H.; Sun, L.; Bruening, M. L. *Nano Lett.* **2006**, *6*, 2268.

[42] Thery-Merland, F.; Methivier, C.; Pasquinet, E.; Hairault, L.; Pradier, C. M. *Sensor Actuat. B-Chem.* **2006**, *114*, 223.

[43] Jiang, C. Y.; Markutsya, S.; Tsukruk, V. V. *Langmuir* **2004**, *20*, 882.

[44] Félidj, N.; Truong, S. L.; Aubard, J.; Lévi, G.; Krenn, J.; Hohenau, A.; Leitner, A.; Aussenegg, F. *J. Chem. Phys.* **2004**, *120*, 7141.

[45] Ouasri, A.; Rhandour, A.; Dhamelincourt, M. C.; Dhamelincourt, P.; Mazzah, A. *Spectrochim. Acta A* **2002**, *58*, 2779.

[46] Spencer, K. M.; Sylvia, J. M.; Janni, J. A.; Klein, J. D. *SPIE* **1999**, *3710*, 373.

[47] McFarland, A. D. ; Young, M. A. ; Dieringer, J. A. ; Van Duyne, R. P. *J. Phys. Chem. B* **2005**, *109*, 11279.

[48] Jackson, J. B.; Halas, N. J. *Proc. Natl. Acad. Sci. USA* **2004**, *101*, 17930.

[49] García-Vidal, F. J.; Pendry, J. B. *Phys. Rev. Lett.* **1996**, *77*, 1163.

[50] Wang, H. H.; Liu, C. Y.; Wu, S. B.; Liu, N. W.; Peng, C. Y.; Chan, T. H.; Hsu, C. F.; Wang, J. K.; Wang, Y. L. *Adv. Mater.* **2006**, *18*, 491.

[51] Jain, P. K.; Huang, W. Y.; El-Sayed, M. A. *Nano Lett.* **2007**, *7*, 2080.

[52] Gaponenko, S. V. *Phys. Rev. B* **2002**, *65*, 140303.

[53] Kim, W.; Safonov, V. P.; Shalaev, V. M.; Armstrong, R. L. *Phys. Rev. Lett.* **1999**, *82*, 4811.

[54] White, I. M.; Oveys, H.; Fan, X. *Spectroscopy* **2006**, *21*, 36.

[55] Sirbuly, D. J.; Tao, A.; Law, M.; Fan, R.; Yang, P. D. *Adv. Mater.* **2007**, *19*, 61.

Chapter 9. Gold Nanoparticle clusters inside the nanocanal arrays for trace level detection of DNT

9.1. Introduction

The surface-enhanced Raman scattering (SERS) has been one of prospective sensing tools for trace-level detection of explosives and hazardous chemicals since the demonstration of single molecule detection via SERS-based sensors.[1,2] However, these trace-level detections have been observed only on some random silver nanoparticle aggregates, which cannot be implemented on current sensing systems. The current challenge for practical sensing devices is the fabrication of highly sensitive and large area SERS substrates. We previously demonstrated in chapter 8 that the incorporation of gold nanoparticles into the 3D nanocanal arrays can provide SERS enhancement of four to five orders magnitude higher than observed for conventional 2D random nanoparticle films. We suggested that the Raman scattering by gold nanoparticles distributed along nanocanals efficiently combines with the optical wave guiding, to give dramatic enhancement of Raman scattering. Here, we report a simple and robust fabrication method of large area (5 centimeter), three-dimensional (3D) SERS substrates capable of detecting 100 zeptogram (~330 molecules) of 2,4-dinitrotoluene (DNT). Key to this performance was the combined effects of Raman-active spots of nanoparticle aggregates and the optical waveguide properties by depositing gold nanoparticle aggregates within 3D nanochannel arrays of porous alumina membranes.

The surface plasmons in the metallic nanostructures, which are collective excitations of free electrons in a metal resonating with incident light, have been known to enhance molecular spectroscopies such as IR absorption, fluorescence, and Raman scattering. Especially, the enhancement of Raman scattering have been demonstrated to be close to 10^{14} for analyte attached on the interparticle gaps (e.g. "hot spots") of metal nanoparticle aggregates, enabling single molecule detection by using surface-enhanced Raman scattering (SERS).[3,4] However, the typical surface-averaged SERS enhancement factor from 2D random metal nanostructures are about 10^4-10^6 far from trace level detection of analytes. While the enhancement factor of 10^8-10^9 have been demonstrated theoretically and experimentally for close-packed 2D metal nanosphere arrays formed by self-assembly, the processes are not often easy to reproduce SERS-active substrates over large areas for practical purposes.

The main mechanism of SERS effect is the signal enhancement by the strong local electromagnetic fields arising when the incident laser light is in resonance with the surface plasmons of metal nanostructures. While isolated metal nanospheres have been shown to provide enhancement factors about 10^3–10^4 for gold and 10^6–10^7 for silver, aggregated nanoparticle clusters have been demonstrated to provide SERS enhancement factors of up to 12 orders of magnitude, enabling even a single molecule detection.[3,6,5] These huge SERS effects are now known to appear due to very strong optical fields localized on the very small gaps (hot spots) between nanoparticles. However, when the SERS enhancements averaged on the interrogated area with the size of laser beam, the typical values of enhancement factors drop to the value of 10^4-10^6. Therefore, large

SERS enhancements from surface-averaged signal will be meaningful for practical applications of SERS sensors. The rational approaches will be the increase of surface density of hot spots or interparticle gaps within the interrogated area in addition to the optimization of interparticle gaps for maximized surface-averaged SERS enhancements. However, the number of hot spots on the 2D planar substrates is limited by the maximum packing density of nanoparticles. In this regard, 3D assembly of nanoparticle clusters present a novel way to fabricate SERS substrates overcoming the limitation of 2D assembly of nanoparticle clusters.

We describe the design of extremely high SERS-active substrates by using three-dimensional nano-canal arrays decorated with gold nanoparticle clusters. The nanocanal surface coated with positively charged polyelectrolytes provide the controlled aggregation of positively charged nanoparticles inside the nanocanals without any pore blocking. Here, the combined effects of the SERS-active hot spots on the aggregated metal nanoparticle clusters, the selective polyelectrolyte coating for target analytes, and the efficient light interactions with the hot spots through the 3D geometry of nano-canal arrays, give rise to extremely high SERS effects. We demonstrate the ability of this SERS substrate for trace level detection of nitroaromatic explosives by detecting down to 100 zeptogram (~330 molecules) of DNT.

9.2. Sample Preparations

Porous alumina membranes (Anodisc 47, Whatman) were decorated with Au nanoparticles by filtration of Au nanoparticle solution on surface-modified porous

alumina membranes, as described in detail in previous chapter. Here, we used PEI for surface modification and carefully tuned the concentration of CTAB to fabricate aggregated gold nanoparticles inside the pores instead of individual gold nanoparticles. Typically, inner surface of porous membranes were modified with polyethylenimine (PEI, M_w=55,000, Aldrich) by spin-coating (3000 rpm, 30 sec) of 0.2% PEI aqueous solution followed by rinsing with Nanopure water (18 MΩ cm). The concentration of CTAB was tuned by removing excess amounts of CTAB surfactant in the Au colloid solution via repeated centrifugation and multi-step dilution.

9.3. Results and Discussion

The methods for the aggregation of individual metal nanoparticles into clusters, induced by the addition of inorganic salts or organic binding agents, are well established.[6,7] However, the assembly of nanoparticle clusters on the inner-walls of nanopores is a challenge because the relatively large and metastable nanoparticle clusters cannot easily go into the nanopores and attach on the inner surfaces. In this study, we utilized electrostatic interactions between the charged gold nanoparticles and the chemically-modified surfaces of alumina membranes to put individual gold nanoparticles into the nanopores and simultaneously induce nanoparticle aggregations on the modified inner-surfaces. Figure 9.1a shows the fabrication procedure for controlled assembly of AuNP aggregates inside the nano-canal arrays. The surface of porous alumina membranes was modified with PEI, where the columbic repulsion between positively-charged PEI and gold nanoparticles prevents the attachment of gold nanoparticles on the

outer-surface of alumina membranes, which may cause the pore-blocking. The amine groups in the PEI,

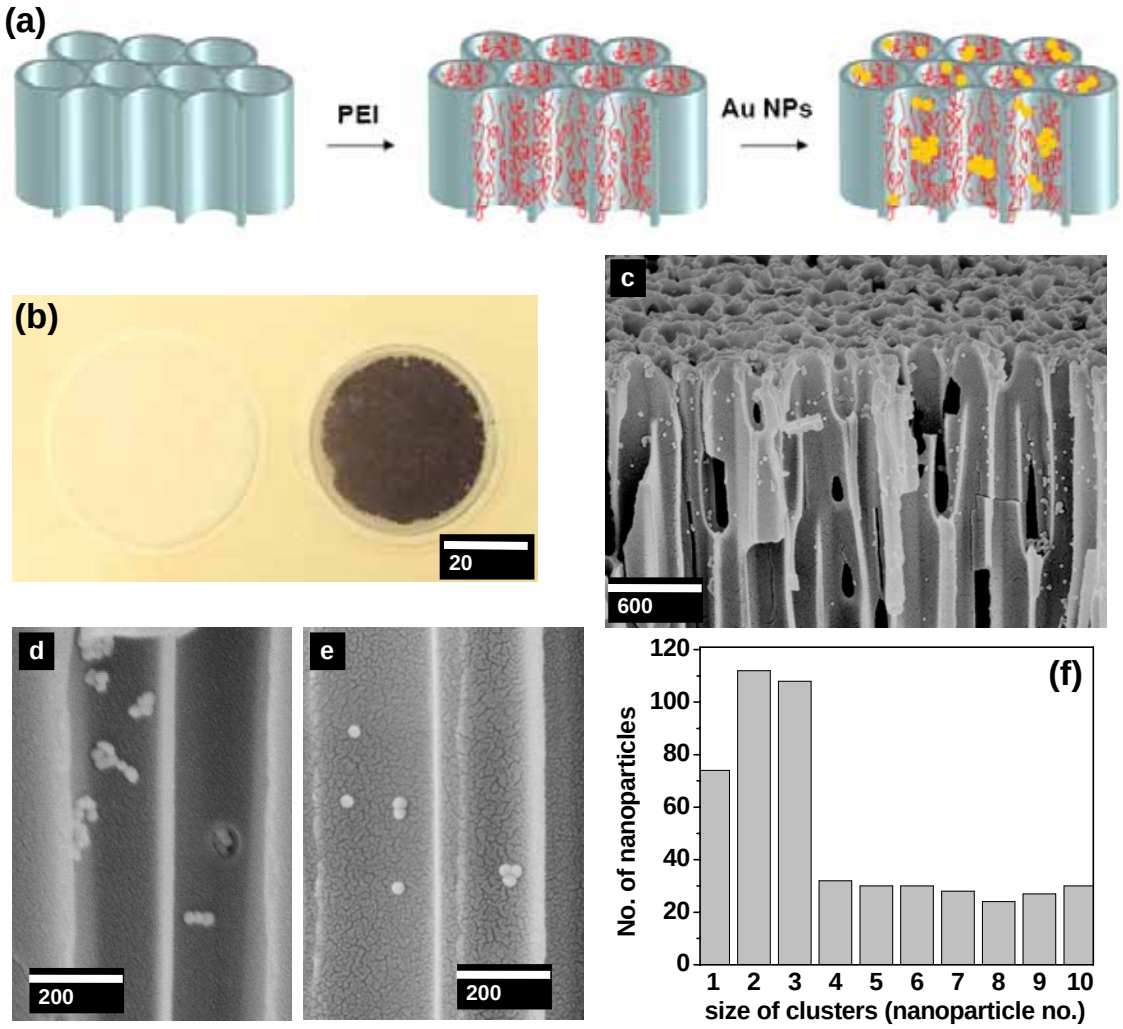

Figure 9.1. (a) Schematic of fabrication procedures for nano-canal arrays decorated with aggregated gold nanoparticle clusters. The surface of porous alumina membranes are functionalized with positively charged amine-groups by modification with PEI and CTAB-capped gold colloids are then passed through the PEI-modified porous alumina membranes resulting in the formation of aggregated Au nanoparticle clusters inside the pores. (b) Photograph of porous alumina membranes before (left) and after (right) the decoration of gold nanoparticles. (c) Cross-sectional SEM image of nano-canal arrays decorated with AuNP clusters. (d) and (e) high-resolution SEM images of aggregated AuNP clusters inside the pores. (f) Histogram of the number of gold nanoparticles in nanoparticle clusters.

on the other hand, are used to attach gold nanoparticles on the inner-walls of porous

alumina membranes by partial replacement with the CTAB ligands on the gold nanoparticle surface during the filtration of AuNP solution. Figure 9.1b shows the photograph image of porous alumina membranes before and after the incorporation of gold nanoparticles. The advantage of our method is the fabrication of large area SERS substrates. As can be seen in Figure 9.1b (right side image), the porous alumina membranes with 47 mm diameter can be easily decorated with gold nanoparticles, resulting in membrane color change from white to purple-blue.

We found that the CTAB plays a major role in the aggregation of nanoparticles inside the nanocanals. The cationic surfactant CTAB is known to form self-assembled bilayers on the AuNP surfaces and provide positively charges on the AuNPs, stabilizing nanoparticles by repulsive forces between nanoparticles.[8] However, when the concentration of CTAB is low, the CTAB molecules are known to link together the {100} facets of neighboring metal nanoparticles, assembling nanoparticles into linear chains or networked structures depending on the concentration of CTAB.[9,10] We found in this study that the gold nanoparticles can be assembled into aggregated clusters on the inner-walls of nanocanals when we controlled the balance between the repulsive and attractive forces by optimizing the concentration of CTAB within 1-10 μM. The CTAB concentration over or below the optimum values only results in no-attachment of nanoparticles or attachment only on the outer surface of nanocanal arrays. The cross-sectional SEM image (Figure 9.1c) shows that most of AuNPs are assembled into aggregated clusters inside the pore walls without attachment on the outer-surface or pore blocking. The high-resolution SEM images (Figure 9.1d,e) indicates that aggregated

AuNPs are dimers, trimers, and larger clusters, which are considered to provide hot spots for strong SERS effects. Figure 9.1f indicates that about 60-70% of nanoparticles aggregated into clusters and most of clusters are dimers and trimers.

The hot spots of aggregated nanoparticles distributed all over the 3D nanocanal arrays can be efficiently combined with the optical waveguide effects of nanoporous alumina membranes providing highly-efficient SERS substrates. The performance of nanocanal arrays decorated with nanoparticle aggregates as SERS-active substrates was demonstrated by measuring the SERS spectra of 2,4-dinitrotoluene adsorbed on them. Fig 9.2a shows the Raman spectra of 2,4-DNT on nano-canal arrays decorated with AuNP clusters and on 2D nanoparticle films. The SERS spectra of 2,4-DNT on our SERS chips is characterized by two strong bands due to vibration modes of -NO_2 groups at 834 cm^{-1} for NO_2 out-of-plane bending modes (ρ_{NO2}) and 1342 cm^{-1} for NO_2 stretching modes (ν_{NO2}). On the other hand, the SERS spectra of DNT on 2D nanoparticle arrays can not be clearly dissolved. The capability of this SERS substrate for trace-level detection of explosives is shown in Figure 9.2b. The peak from NO_2 stretching modes of DNT at 1342 cm^{-1} can be clearly resolved with 100 ppt 2,4-DNT. With further decrease in the concentration of DNT, the peaks at 1342 cm^{-1} decrease and can not be clearly resolved below 100 ppq DNT. From the signal-to-noise (S/N) ratio, we estimate the detection limit is 1 ppt DNT (S/N ratio is 3). This 1 ppt detection limit corresponds to 100 zeptogram within the interrogated area, which is about 328 DNT molecules. This value is well beyond the detection limit of DNT on conventional SERS substrates such as roughened metal electrodes or oriented silver nanowires arrays. In

addition, the nanoparticle-decorated nanocanal arrays have advantages of simple and inexpensive fabrication over large-area and uniform SERS substrates for the detection of truly trace-level detection of analytes.

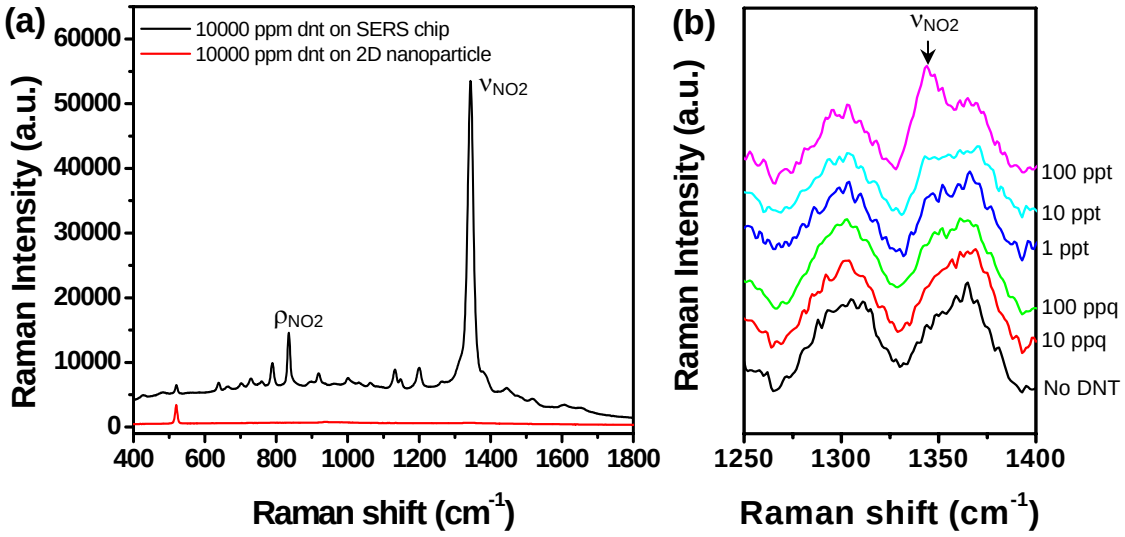

Figure 9.2. Raman spectra of 2,4-DNT on nano-canal arrays decorated with AuNP clusters. (a) A representative Raman spectra with 10000 ppm 2,4-DNT on our SERS chip and 2D nanoparticle films. (b) Raman spectra of trace level 2,4-DNT indicating down to 1 ppt detection capability.

We suggest here that the extraordinary high SERS-active properties of nanoparticle-decorated nanocanal arrays is associated with the combined effects of hot spots from nanoparticle aggregates and optical waveguide effects of anodic alumina membranes. Previously, we have demonstrated that the optical waveguide effects of anodic alumina membranes can provide additional enhancement of Raman scattering of about five orders magnitude higher than that of conventional planar nanoparticles arrays.[11] While previous study has focused on individually separated nanoparticle arrays without major contribution from hot spots, we show here that the optical waveguide

effects can be combined with hot spots of aggregated nanoparticle clusters, resulting in highly-active SERS substrates capable of detecting down to several molecules of DNT.

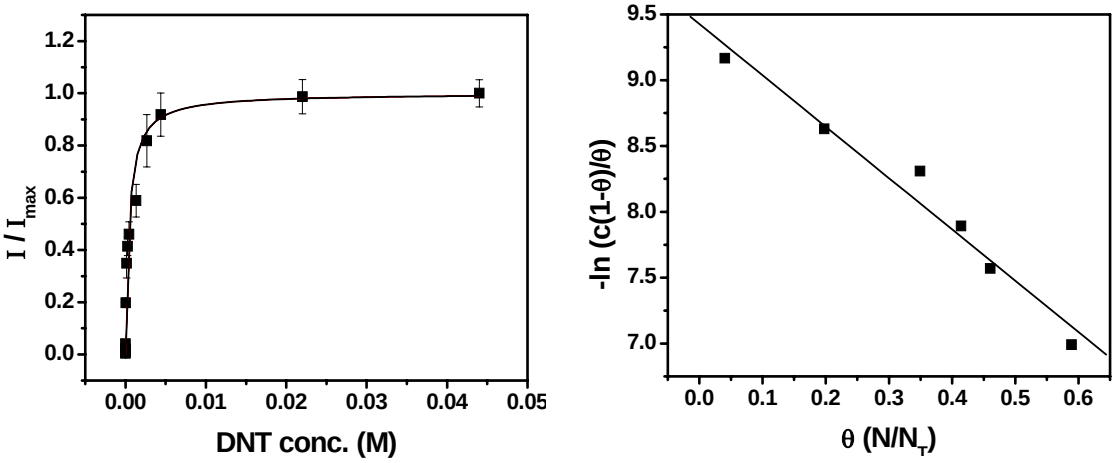

Figure 9.3. (a) The adsorption isotherm of DNT on nanocanal arrays decorated with gold nanoparticles. The Frumkin isotherm model (equation 1) was used to fit the experimental data. (b) Frumkin isotherm fitting of linear region of experimental data.

The variation of Raman intensity with the concentration of 2,4-DNT is shown in Fig 9.3. At low DNT concentrations, the Raman intensity at 1342 cm^{-1} increases linearly with DNT concentration. At higher DNT concentration, the increase in Raman intensity saturates at ~ 0.004 M of DNT due to full occupation of adsorption sites by the DNT molecules. This saturation concentration of analyte is much higher than typical 2D SERS substrates, providing much large dynamic range of analyte concentration.

To determine the adsorption process of DNT on the 3D SERS chips, Frumkin isotherm was used to fit the experimental data:

$$\theta = \frac{I_{1343}}{I_{1343,\max}} = \frac{CKe^{2g\theta}}{1+CKe^{2g\theta}} \qquad (1)$$

$$\ln\left[\frac{\theta}{C(1-\theta)}\right] = 2g\theta + \ln K \qquad (2)$$

where θ is the fractional coverage of DNT on the SERS chip; $I_{1343,max}$ is the maximum SERS intensity at 1343 cm^{-1} when all the adsorption sites are occupied by the DNT molecules; c is the DNT solution concentration in M; K is the adsorption constant of DNT on SERS chip; g is the Frumkin constant. The g and K values can be extracted from the linear fitting by using equation 2 (Figure 9.3b). The obtained g value is −1.95 and K value is 1.21×10^4 M^{-1}. The sign of g value indicates the repulsive or attractive force between adsorbed molecules. The negative g value in our system indicates repulsive force between adsorbed DNT. The large value of K indicates the strong interactions between the adsorbed DNT and the PEI modified gold nanoparticles. This strong interaction can be associated with the interactions between the electron-rich amine groups in PEI and electron-deficient NO_2 group in DNT.

Because the light interactions with hot spots dispersed in 3D structure of nanoparticle-decorated nanocanal arrays are critical factor determining the sensitivity of SERS-acitve nanocanal arrays, it is worth to investigate the optical interactions of 3D nanocanal arrays with varying amount of gold nanoparticles loading inside the nanocanals. Figure 9.4a shows the SERS intensity at 1342 cm^{-1} for different SERS substrates with varying AuNP loadings on the nano-canal arrays. As the AuNP loading increases from 8 to 32 μmol/cm^3, the SERS intensity also increases due to increase in the number of hot spots inside the nano-canal arrays. However, further increase in AuNP loadings results in the decrease in SERS intensity, which can be related to the decreased

light transmission through the nanopores due to the presence of gold nanoparticles, resulting in decreased interactions of light with those hot spots existing deep into the nanopore walls.

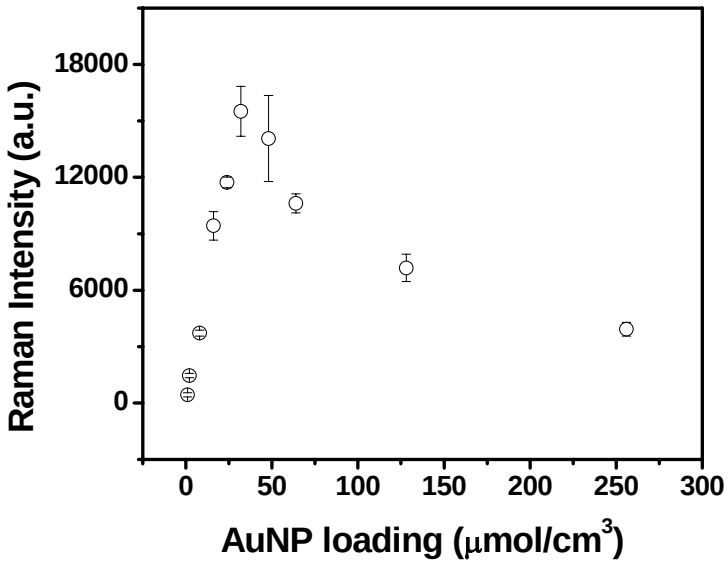

Figure 9.4. Comparison of Raman intensities at 1342 cm^{-1} with different loadings of nanoparticles inside the nanocanal arrays.

The change in light interaction with the 3D nanocanal arrays with the loading of gold nanoparticles can be clearly seen in the absorption and transmission of light in Figure 9.5. The bare porous alumina membranes show no obvious absorption peak except a very weak and broad band at 600-800 nm. When the gold nanoparticles are infiltrated into the membranes, a strong band at 530 nm and weak band at 600-800 nm appear. The band at shorter-wavelength is ascribed to the surface plasmon resonance of single gold nanoparticles. As the amount of gold nanoparticles inside the membranes increases, an increase in longer-wavelength band are evident. This increase in longer-wavelength indicates increased coupling between nanoparticles with increasing the

amount of

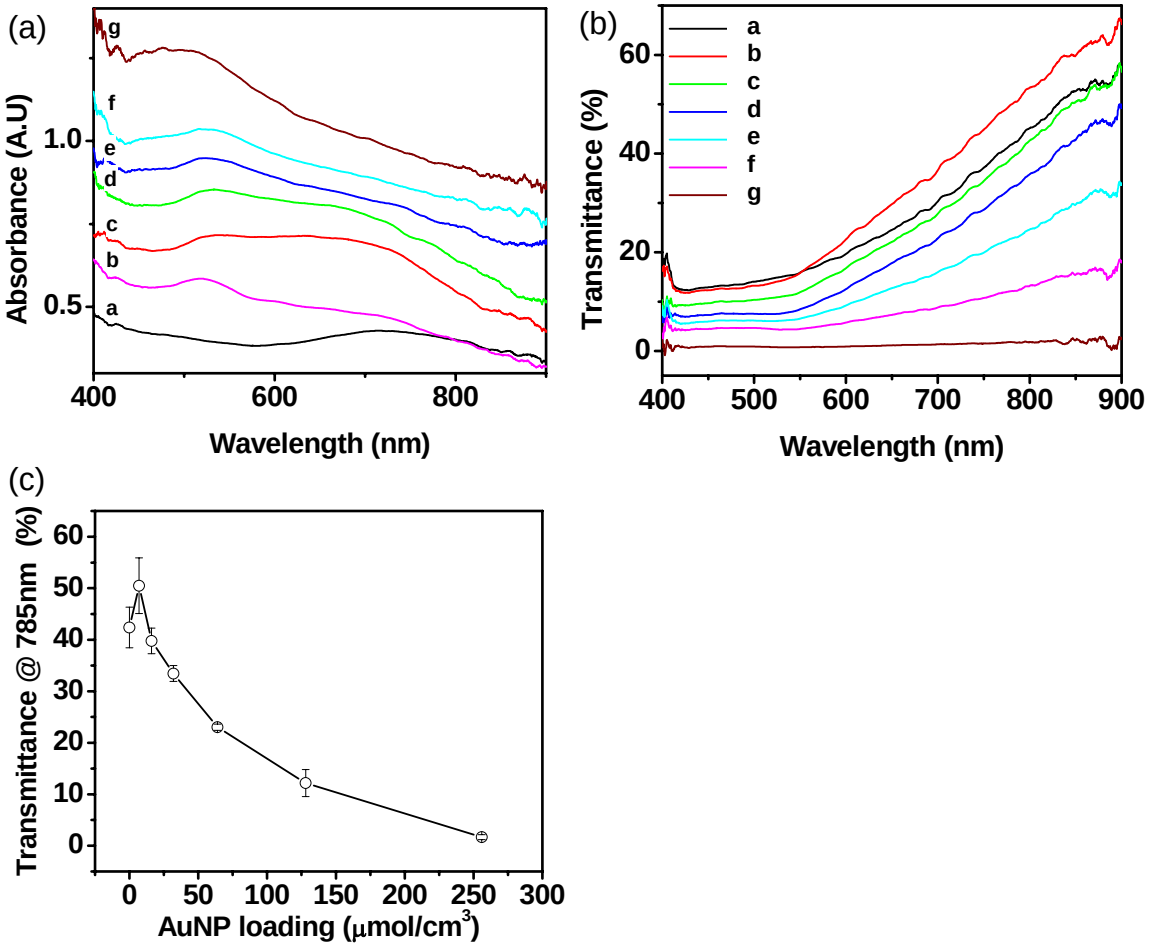

Figure 9.5. (a) Absorbance and (b) transmittance of nano-canal arrays decorated with AuNP clusters with different AuNP loadings (a:0, b:8, c:16, d:32, e:64, f:128, g:256 μmol/cm^3). (c) Transmittance at 785 nm wavelength in Figure 4c with different AuNP. loadings.

nanoparticles. However, the adsorption at shorter-wavelength becomes stronger than that of longer-wavelength when the AuNP loading is over 32 μmol/cm^3 and disappear at higher AuNP loadings (over 128 μmol/cm^3). This change in absorption in combination with the transmission can be associated with the decrease in SERS intensity after the AuNP loading of 32 μmol/cm^3. Similar behavior has been observed for 2D nanoparticle

aggregates with SERS intensity decreased after a critical point with increasing the surface coverage of nanoparticles.[12,13,14] This decrease in SERS intensity for 2D nanoparticle films has been explained by comparing the extinction maximum and the excitation wavelength.nd the excitation wavelength. At initial stage, the SERS intensity increases with the increase of surface coverage of nanoparticles as long as the wavelength of plasmon resonance is shorter than excitation wavelength. Then, the SERS intensity decreases with further deposition of nanoparticles when the extinction maximum is longer than the excitation wavelength.

In addition to the change in adsorption peak, the change in transmission is also related to the change in SERS intensity. The addition of gold nanoparticles into the alumina membranes causes the decrease in light transmission. Figure 9.5b shows the transmission spectra of the porous alumina membranes with and without infiltration of gold nanoparticles. The transmission of bare porous alumina membranes is relatively high (40-50%) in the near-IR range and decrease in the visible range due to the high scattering in the visible range. Upon the incorporation of gold nanoparticles, the transmission of the Au-PAMs decreases mainly due to high adsorption of photons by the gold nanoparticles. In Figure 9.5c, we compared the transmission of SERS chips at 785 nm, the wavelength of excitation laser. The transmission decreased exponentially with increasing the amount of gold nanoparticles inside the membranes. Therefore, for 3D au-PAM system, we suggest that the decreased transmission of excitation light with increasing the loading of nanoparticles is the main cause of the decrease in SERS intensity.

9.6. References

[1] Nie, S. M.; Emery, S. R. *Science* **1997**, *275*, 1102.

[2] Kneipp, K.; Wang, Y.; Kneipp, H.; Perelman, L. T.; Itzkan, I.; Dasari, R.; Feld, M. S. *Phys. Rev. Lett.* **1997**, *78*, 1667.

[3] Nie, S. M.; Emery, S. R. *Science* **1997,** 275, 1102.

[4] Kneipp, K.; Wang, Y.; Kneipp, H.; Perelman, L. T.; Itzkan, I.; Dasari, R.; Feld, M. S. *Phys. Rev. Lett.* **1997,** *78*, 1667.

[5] Xu, H. X.; Bjerneld, E. J.; Kall, M.; Borjesson, L. *Phys, Rev. Lett.* **1999,** *83*, 4357.

[6] Kneipp, K.; Kneipp, H.; Manoharan, R.; Hanlon, E. B.; Itzkan, I.; Dasari, R. R.; Feld, M. S., *Appl. Spectrosc.* **1998**, *52*, 1493.

[7] Michaels, A. M.; Nirmal, M.; Brus, L. E. *J. Am. Chem. Soc.* **1999**, *121*, 9932.

[8] Nikoobakht, B.; Wang, Z. L.; El-Sayed, M. A. *J. Phys. Chem. B* **2000**, *104*, 8635.

[9] Yang, Y.; Matsubara, S.; Nogami, M.; Shi, J.; Huang, W. *Nanotechnology* **2006**, *17*, 2821.

[10] Yang, Y.; Shi, J.; Tanaka, T.; Nogami, M. *Langmuir* **2007**, *23*, 12042.

[11] Ko, H.; Tsukruk, V. V. *Phys. Rev. Lett.* submitted

[12] Maxwell, D. J.; Emory, S. R.; Nie, S. *Chem. Mater.* **2001**, *13*, 1082.

[13] Adison, C. J.; Brolo, A. G. *Langmuir* **2006,** *22*, 8696.

[14] Olson, L. G.; Lo, Y.-S.; Beebe Jr., T. P.; Harris, J. M. *Anal. Chem.* **2001**, *73*, 4268.

Chapter 10. General Conclusions and Future Directions

The work presented in this dissertation has suggested novel fabrication methods for the assembly of zero- and one-dimensional nanoscale building blocks and discovered novel properties and phenomena from the assembled nanostructures. In this work, we developed several assembly strategies to organize carbon nanotubes and gold nanoparticles into hierarchical nanostructured arrays via controlled bottom-up assembly onto various substrates containing chemical or physical templates. In addition, we have found some novel electrical, mechanical, and optical properties from the assembled nanostructued arrays of carbon nanotubes and gold nanoparticles. We successfully demonstrated the prospective use of assembled nanostructure arrays for device applications by designing flexible carbon nanotube nanomembranes as mechanical sensors, highly-oriented carbon nanotubes arrays for thin-film transistors, and gold nanoparticle arrays for SERS chemical sensors.

In Chapter 3, we demonstrated the fabrication of patterned assembly of carbon nanotube arrays on the silicon surface by using solution-based techniques as the way for assembling carbon nanotube arrays. In the course of this work, we found that the patterned hydrophobic and hydrophilic SAMs can be used to control the selective assembly and patterned organization of CNT arrays. For dip-coating process, we suggested that nanotubes are initially adsorbed during immersion, and then aligned during the drying process by combined hydrodynamic and capillary forces. However, for the casting process, nanotubes adsorption and alignment arise at the same time, resulting

in highly packed nanotube arrays. During the casting process on the tilted surface, the liquid film spontaneously sweeps down at the patterned substrate, concentrating the solution concentration along the hydrophilic stripes. Successive drying of this liquid film causes nanotubes deposition by the nucleation along the contact line. In this case, the nanotubes align parallel to the contact line. We also showed that the tangential G-mode shift downward upon nanotube bending, and we attribute the shift to tensile strain of bending nanotube, which result in the extension of C–C bond.

As an extension of this work, in Chapter 4, we have developed simple and easy solution-based assembly strategy for the fabrication of densely-packed, uniaxially aligned SWNTs as a semiconducting layer in CNT-TFTs. We suggested using liquid crystalline behavior of CNT solution in the vicinity of the receding contact line induced by localized solvent vaporization. We have successfully controlled the nematic-like ordering of carbon nanotubes during tilted-drop casting process by using confined micropatterned geometry. Because of the liquid crystalline behavior near the contact line, this process does not require highly concentrated CNT solution and still provides densely-packed and uniformly oriented CNTs with predominantly monolayer surface films. We further demonstrated that the electrical performance of thin-film transistors based on these densely-packed uniformly oriented CNT array is dramatically improved as compared to the TFTs with random CNTs because the uniaxially oriented SWNTs significantly reduce the number of inter-tube contacts that the carriers should pass through.

In addition to the silicon substrate, we have also developed a method to fabricate polymer membranes containing CNT arrays as a central layer. We have developed a novel method to investigate the deformational behavior in freely suspended polymer nanomembranes with embedded carbon nanotubes subjected to elastic deflections by conducting *in-situ* monitoring of resonance Raman scattering directly in the course of full deformational cycle (Chapter 5). In this study, we have found a deformational process for these deforming nanomembranes as indicated by very different Raman peak changes at low and high deflections. We have suggested that the deformational behavior at low deflections (strain below 0.05 %) included mainly buckling of the bent carbon nanotubes. However, for large nanomembranes deflections when tensile strain dominates, along-axis stretching leads to the intensive shift of the Raman peaks to lower frequencies.

We demonstrated that the patterned array of carbon nanotubes can be successfully incorporated into the freely suspended, flexible LbL membranes by using the micropatterned LbL surface as a template for subsequent nanotube assembly (Chapter 6). The patterned array of monolayered carbon nanotubes with a thickness of 5 nm was sandwiched between two ultrathin polymer multilayers with the thickness of about 19 nm each. A key element of the microfabrication routine introduced here is the exploitation of a polymer sacrificial micropattern as a template for assembly of carbon nanotubes followed by its removal and further derivatization of the exposed surface areas with a topmost polyelectrolyte multilayer to complete encapsulation. By using confocal Raman imaging, we demonstrated that the carbon nanotube array embedded into the polymer

film generates highly contrasted resonance Raman grating which might be considered for sensing applications.

To establish robust patterning techniques for carbon nanotube and gold nanoparticle arrays inside the polymer membranes, we developed so-called "capillary transfer lithography" as a simple and efficient method of creating 3D micropatterned templates on the surface of LbL multilayers by transferring polymer patterns from PDMS mold onto the target substrate (Chapter 7). The key elements of this method are the creation of polymer microstructure and the transfer onto the polyelectrolyte surface. The polymer microstructure introduced here is easily transferred from the recessing regions of the PDMS mold to target substrate in a controllable manner, resulting in 3D open microstructure with no residual polymer layer on the compressed region. We suggested that these polymer microstructures can be used as sacrificial templates for subsequent assembly of both carbon nanotubes and gold nanoparticles onto LbL films in the patterned manner. The advantages of this approach include highly selective patterning, greater control over the 3D structure, and the possibility of further modification of protected surface areas. We demonstrated that further modification of intact surface areas can be used to fabricate heterogeneous orthogonal arrays or encapsulate nanoparticular arrays into LbL multilayers.

In Chapter 8, we demonstrated the assembly of gold nanoparticles into three-dimensional arrays and showed prospective device applications in SERS-based sensors. First, we observed gigantic Raman scattering from 3D porous substrate nanocanals decorated with

low concentration gold nanoparticles without nominal "hot spots". The nanoparticle-decorated nanocanal arrays showed about five orders higher enhancement of Raman scattering than that of conventional planar nanoparticles arrays, which cannot be attributed solely to the increase in specific surface area. We suggested that the Raman scattering by gold nanoparticles distributed along nanocanals efficiently combines with the optical wave guiding, to give dramatic enhancement of Raman scattering. As an extension of this work, in chapter 9, we developed ultra-high active SERS substrates for the detection of trace level DNT, a model compounds of nitroaromatic explosives. We suggested that the high performance is associated with the combined effects of Raman-active spots of nanoparticle aggregates and the optical waveguide properties by depositing gold nanoparticle aggregates within 3D nanochannel arrays of porous alumina membranes.

Overall, this research has suggested some novel solution-based assembly strategies for the fabrication of functional nanostructured arrays from zero- and one-dimensional nanoscale building blocks. The developed assembly strategies have great potential in low-cost, large-scale processing of high-performance electronic devices based on functional nanoscale building blocks. Although we demonstrated the assembly of nanoscale materials with simple geometry of patterns, further research need to be done toward the development of efficient bottom-up strategies for the assembly of nanoscale materials into complicated and hierarchical architectures enabling the use of nanoscale materials for practical device applications.

Appendix A: List of Publications

The results of this dissertation have been published in:

1. **Hyunhyub Ko,** Srikanth Singamaneni, and Vladimir V. Tsukruk, Nanostructured surfaces and nanoparticles for SERS applications, Invited Review, *Small*, submitted.
2. **Hyunhyub Ko** and Vladimir V. Tsukruk, Three-dimensional surface-enhanced Raman spectroscopy substrates, manuscript in preparation.
3. **Hyunhyub Ko** and Vladimir V. Tsukruk, Nanoparticle-decorated nanocanals as efficient SERS media, *Small*, submitted.
4. **Hyunhyub Ko** and Vladimir V. Tsukruk, Liquid-Crystalline Processing of Highly Oriented Carbon Nanotube Arrays for Thin-Film Transistors, *Nano Lett.* **2006**, 6, 1443. (*Featured in SPIE newsroom, Solution Processing Simplifies the Manufacturing of Carbon Nanotube Transistors, 2006, x8606*)
5. **Hyunhyub Ko**, Chaoyang Jiang and Vladimir V. Tsukruk, Encapsulating nanoparticle arrays into layer-by-layer multilayers by capillary transfer lithography. *Chem. Mater.* **2005,** 17, 5489.
6. Chaoyang Jiang, **Hyunhyub Ko**, and Vladimir V. Tsukruk, Strain sensitive Raman modes of carbon nanotubes in deflecting freely suspended nanomembranes. *Adv. Mater.* **2005**, 17, 2127.
7. **Hyunhyub Ko**, Chaoyang Jiang, Hennady Shulha, Vladimir V. Tsukruk, Carbon nanotube arrays encapsulated into freely suspended flexible films. *Chem. Mater.* **2005**, 17, 2490. (*Featured in MRS Bulletin, CNT Arrays encapsulated into freely suspended flexible films, 2005, 30 (7), 501*)
8. **Hyunhyub Ko**, Yuri Pikus, Chaoyang Jiang, Andrea Jauss, Olaf Hollricher, and Vladimir V. Tsukruk, Raman spectroscopy of curled carbon nanotubes, *Appl. Phys. Lett.* **2004**, 85, 2598.
9. **Hyunhyub Ko**, Sergiy Peleshanko, and Vladimir V. Tsukruk, Combing and Bending of Carbon Nanotube Arrays with Confined Microfluidic Flow on Patterned Surfaces, *J. Phys. Chem. B* **2004**, 108, 4385.
10. Vladimir V. Tsukruk, **Hyunhyub Ko**, and Sergiy Peleshanko, Nanotube Surface Arrays: Weaving, Bending, and Assembling on Patterned Silicon, *Phys. Rev. Lett.* **2004**, 92, 065502. *(Featured in Physical Review Focus, Nanotubes Go with the Flow, 12 February 2004 and in Materials Today, Bending over backwards for nanotubes, 2004, 5, 9)*

The other related results have been published in:

1. Suck Won Hong, Wonje Jeong, **Hyunhyub Ko**, Michael R. Kessler, Vladimir V. Tsukruk, and Zhiqun Lin, Directed self-assembly of gradient concentric carbon nanotube rings, *Adv. Funct. Mater*, accepted.

2. Ray Gunawidjaja, Sergiy Peleshanko, **Hyunhyub Ko**, and Vladimir V. Tsukruk, Bimetallic nanocobs: decorating silver nanowires with gold nanoparticles, *Adv. Mater.*, accepted.

3. Eugenia Kharlampieva, Taisia Tsukruk, Joseph M. Slocik, **Hyunhyub Ko**, Nicole Poulsen, Rajesh R. Naik, Nils Kröger, and Vladimir V. Tsukruk, Bio-enabled Surface-mediated Growth of Uniform Titania Nanoparticles, *Adv. Mater.,* accepted.

4. Ray Gunawidjaja, **Hyunhyub Ko**, Chaoyang Jiang, and V. V. Tsukruk, Buckling behavior of highly oriented silver nanowires encapsulated within multilayered LbL films, *Chem. Mater.* **2007**, 19, 2007.

5. Ray Gunawidjaja, Chaoyang Jiang, **Hyunhyub Ko** and V. V. Tsukruk, Freestanding 2D Arrays of Silver Nanorods, *Adv. Mater.* **2006**, 18, 2895.

Conference Presentations:

1. **Hyunhyub Ko**, Chaoyang Jiang and Vladimir V. Tsukruk, Freely Suspended Hybrid Nanotube Forests for Surface-Enhanced Raman Spectroscopy, MRS Meeting, San Francisco, March **2007**.

2. **Hyunhyub Ko** and Vladimir V. Tsukruk, Highly-oriented carbon nanotube arrays by Liquid-crystalline processing and the Application as Thin Film Transistors, MRS Meeting, Boston, November **2006**.

3. **Hyunhyub Ko**, Chaoyang Jiang, and Vladimir V. Tsukruk, Carbon Nanotube Arrays Encapsulated into Polyelectrolyte Multilayer Films, MRS Meeting, Boston, November **2006**.

4. Ray Gunawidjaja, Chaoyang Jiang, **Hyunhyub Ko**, Sergiy Peleshanko, Maryna Ornatska, Srikanth Singamaneni, and V. V. Tsukruk, Freely Suspended Silver Nanowires, MRS Meeting, Boston, November **2006**.

5. **Hyunhyub Ko**, Chaoyang Jiang, and Vladimir V. Tsukruk, Assembly of carbon nanotube arrays, *229th* ACS National Meeting, San Diego, March **2005.**

6. Chaoyang Jiang, **Hyunhyub Ko**, and Vladimir V. Tsukruk, Confocal Raman spectroscopy of bent carbon nanotubes, *229th* ACS National Meeting, San Diego, March **2005.**